UNIVERSITY OF CALIFORNIA, SAN DIEGO

A Study on the Phase Stability and Diffusion Behavior of Alkaline-Earth Hexaborides

A Dissertation Submitted in Partial Fulfilment

of the Requirements for the Degree of Doctor of Philosophy

in

Materials Science and Engineering

by

James T. Cahill

Committee in Charge:

Professor Olivia A. Graeve, Chair
Professor Renkun Chen
Professor Robert E. Continetti
Professor Joanna M. McKittrick
Professor Marc A. Meyers

2016

The Dissertation of James T. Cahill is approved, and it acceptable in quality and form for publication on microfilm and electronically:

_____

_____

_____

_____

_____

Chair

University of California, San Diego

2016

Dedication

To my parents, who found the perfect balance between drive and support. You taught me to think, to listen and to learn. I owe you everything.

To my better half, you are my best friend in the entire world and the most perfect life partner. You truly make me a better person, and I cannot wait to spend the rest of my life by your side.

Table of Contents

List of Tables

List of Figures

Acknowledgements

This project was funded by National Science Foundation grant #1360561.

Research experiments were performed at the CaliBaja Center for Resilient Materials and Systems at the University of California, San Diego and at Alfred University in Alfred, New York.

Spark plasma sintering was carried out in the McMahon laboratory at Alfred University in Alfred, New York.

High-resolution transmission electron microscopy was conducted by Raúl Borja-Urby at the Centro de Nanociencias y Micro y Nanotecnologías at the Instituto Politécnico Nacional in Mexico City, México.

Scanning electron microscopy was conducted at the Nano3 User Facility at the University of California, San Diego.

A sincere thank you to Dr. Olivia Graeve, Dr. Doreen Edwards, Dr. Scott Misture, Dr. Victor Vasquez, Dr. Ekaterina Novitskaya, Dr. James Kelly, Michael Alberga, Seth Fuller, Joel Bahena, Chris Pisano and the rest of my coworkers for overall assistance, and going above and beyond the job description to help make this research possible.

Chapter 1, in part, is being prepared for publication authored by J.T. Cahill and O.A. Graeve. The dissertation author was the primary investigator and author of this paper.

Chapter 4, in part, is being prepared for publication authored by J.T. Cahill, M. Alberga, J. Bahena, C. Pisano, R. Borja-Urby, V.R. Vasquez, S.T. Misture, D. Edwards, and O.A. Graeve. The dissertation author was the primary author of this paper.

Chapter 5, in part, is being prepared for publication authored by J.T. Cahill, V.R. Vasquez, S.T. Misture, D. Edwards, and O.A. Graeve. The dissertation author was the primary investigator and author of this paper.

Vita

2012	Bachelor of Science, Alfred University
2012 – 2015	Research Assistant, University of California, San Diego
2014	Master of Science, University of California, San Diego
2015 – 2016	Teaching Assistant, University of California, San Diego
2016	Doctor of Philosophy, University of California, San Diego

Publications

"Development of Mesoporosity in Scandia-Stabilized Zirconia: Particle Size, Solvent, and Calcination Effects" Langmuir, 30:19 5585-5591 (2014)

"Tool Steel as an Alternative Binder for Cemented Tungsten Carbide" In preparation

"Phase Formation and Stability in Mixed-Metal Hexaborides" In preparation

"Effect of current flow on cation diffusion in hexaborides" In preparation

"Hexaborides: a Review" In preparation

ABSTRACT OF THE DISSERTATION

A Study on the Phase Stability and Diffusion Behavior of Alkaline-Earth Hexaborides

by

James T. Cahill

Doctor of Philosophy in Materials Science and Engineering

University of California, San Diego

Professor Olivia A. Graeve, Chair

The following work provides new insight into the behavior of the alkaline-earth hexaborides CaB_6, SrB_6 and BaB_6. Both binary and ternary compounds were produced for the first time by solution combustion synthesis, resulting in cubic particles averaging 500 nm in size. Detailed X-ray diffraction analysis revealed phase separation and formation of nano-domains in ternary (Ba-Ca)B_6 and (Ba-Sr)B_6 compounds. High-resolution transmission electron microscopy confirms the presence of these phases in the

form of homogenous nano-regimes in individual equilibrium within the hexaboride particles. Thermal treatments up to 2000 K enhance the overall homogeneity of the samples and merge the phases into one, indicating that the as-synthesized state is unstable as the collection of nano-regimes results in increased microstrain and lattice imperfections. Analysis of the chemical reactions that occur during synthesis suggests that the decomposition of the metal precursors to metal oxides introduces variance into the formation process of mixed-cation hexaboride compounds, producing nano-regimes within the crystal lattice. Spark plasma sintering was shown to effectively produce high-density hexaboride samples from powders in as little as 45 minutes. The effect of pulsed direct current on metal atom diffusion in CaB_6-SrB_6 couples was investigated. It was shown that the diffusivity of Ca and Sr atoms across the interface was towards the positive electrode when subjected to a current flow of 2.2 kA at a temperature of 2007 K. No new phases were formed at the interface between CaB_6 and SrB_6 as hexaboride compounds readily form solid solutions. Energy-dispersive spectroscopy was used to map the concentration of Ca and Sr surrounding the interface, and diffusion profiles were fitted with error functions. The concentration curves display concentration-dependent diffusivity. Total dopant values (Q) were used to numerically compare the differences between Ca diffusion in SrB_6 and Sr diffusion in CaB_6 under the influence of current. The results provide evidence for the role of pulsed direct current on the diffusion of metal ions in hexaboride compounds.

1. Introduction

1.1. Hexaboride Compounds

Borides are represented by a multitude of compounds found in many modern engineering applications, mostly as refractory materials and ultra-hard ceramics. Many of the unique properties of metal borides stem from their crystal structures and bonding, where the covalent component between the boron atoms forms an incredibly strong bond, providing the materials with high hardness and melting temperatures [1]. Hexaborides are a specific class of metal boride with the chemical formula MB_6 that can be engineered for a wide variety of uses from electron emitters [2, 3] and single-photon detectors [4] to thermoelectrics [5] and superconductors [6-8]. Although a seemingly simple material, hexaborides are in reality a complex group of compounds with curious properties and behaviors, the study of which has piqued the interest of researches in the last few decades. This paper is a collection of these studies formatted to summarize the current state of research (to the best knowledge of the authors) and is broken down into sections detailing the structure, synthesis and properties of metal hexaborides.

1.1.1. Structure and Bonding

The most recognizable feature of hexaborides is their cubic crystal structure, one shared by all compounds with the MB_6 formula. Commonly referred to as the CaB_6 crystal structure, the lattice is composed of a single metal atom surrounded by 8 octahedra of boron atoms, each centered on a corner of the cube (Figure 1). This structure has CsCl-type Pm-3m symmetry with the Cl site representing the boron octahedra.

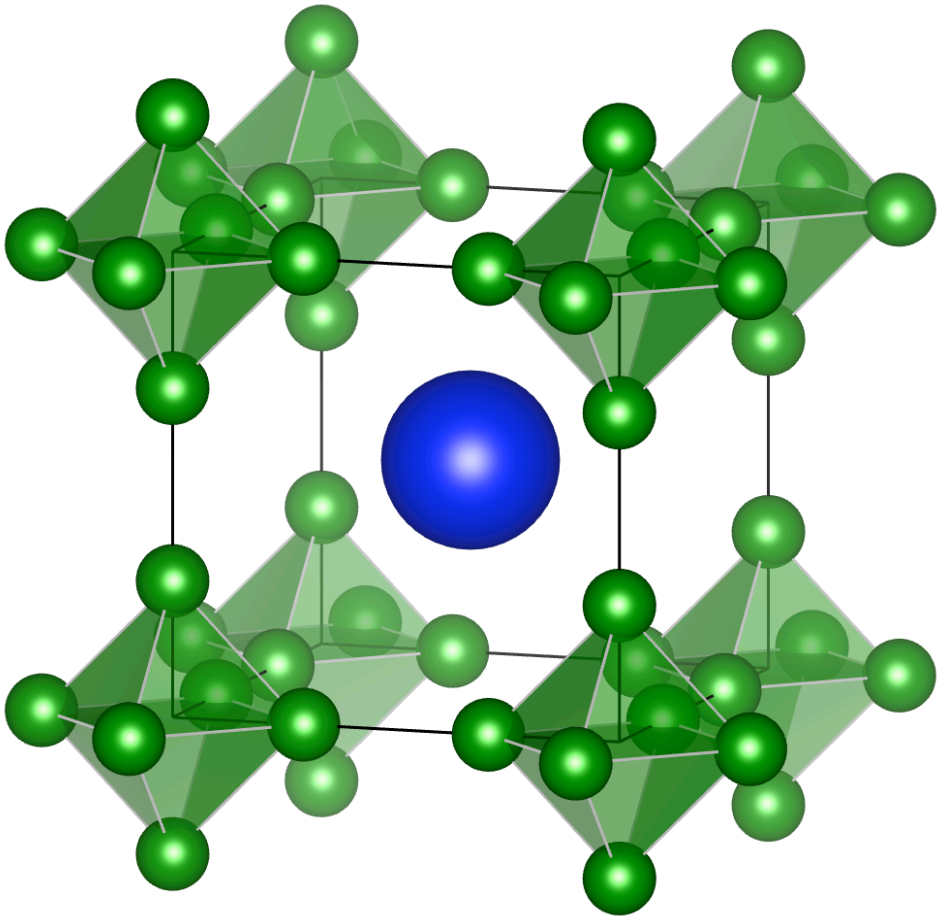

Figure 1 Crystal structure of the CaB_6–type hexaborides

Each boron atom has a coordination of 5, with 4 adjacent in the octahedra and another along one of the cube axes [2]. The metal atoms at the center are coordinated by 24 boron atoms, between which no valence bonds appear to exist [1, 2]. On the other hand, the boron atoms are highly covalently bonded to each other and subsequently responsible for many of the material's physical and chemical properties. Because each boron atom must distribute its 3 valence electrons over 5 bonds, the cubic boron sublattice itself is inherently electron deficient and cannot exist without donated electrons from the metal atoms.

Table 1 Summary of experimental structural parameters for metal hexaborides (adapted from Mackinnon et al [9]).

MB_6	KB_6	CaB_6	SrB_6	YB_6	BaB_6	LaB_6	CeB_6	NdB_6	SmB_6	EuB_6	YbB_6	ThB_6
a (Å)	4.2246	4.1514	4.1953	4.1000	4.2618	4.1569	4.1407	4.1269	4.1346	4.1849	4.1479	4.0931
M site occu-pancy	0.947	1.0	1.0	1.0	1.0	1.0	1.0	1.0	1.0	1.0	1.0	0.997
B site occu-pancy	1.0	1.0	1.0	1.0	1.0	1.0	1.0	0.979	1.0	0.980	0.977	1.15
R_W (%)	2.2	5.0	2.1	4.4	2.9	2.9	0.8	1.9	1.1	1.3	1.6	2.2
M-B (A)	3.1023	3.0528	3.0865	3.0115	3.1373	3.0542	3.0439	3.0314	3.0381	3.0783	3.0495	3.0045
$B\text{-}B_{out}$ (Å)	1.6744	1.6760	1.7040	1.6300	1.7440	1.6590	1.6644	1.6415	1.6688	1.6964	1.6695	1.6100
$B\text{-}B_{in}$ (Å)	1.8033	1.7520	1.7620	1.7460	1.7800	1.7660	1.7511	1.7574	1.7438	1.7596	1.7525	1.7570
z	0.1982	0.2019	0.2031	0.1988	0.2047	0.1996	0.2011	0.1982	0.2018	0.2027	0.2012	0.1970

This concept, coupled with the fact that the boron sublattice forms a semi-rigid "cage", limits the metal atom candidates based on size and valency to alkaline-earth metals, rare-earth metals and thorium. As seen in Table 1, the lattice parameters do not significantly fluctuate between the various metal hexaborides, suggesting that the boron framework is the primary contributor. Although hexaborides must have a metal cation with a charge of at least 2^+ to be electronically stable [10, 11], metal-deficient KB_6 has been produced in controlled environments [12].

The general thermal stability of metal hexaborides is based on two main factors: the saturation vapor pressure of the metal cation and the stability of the bonds in the boron sublattice [1].

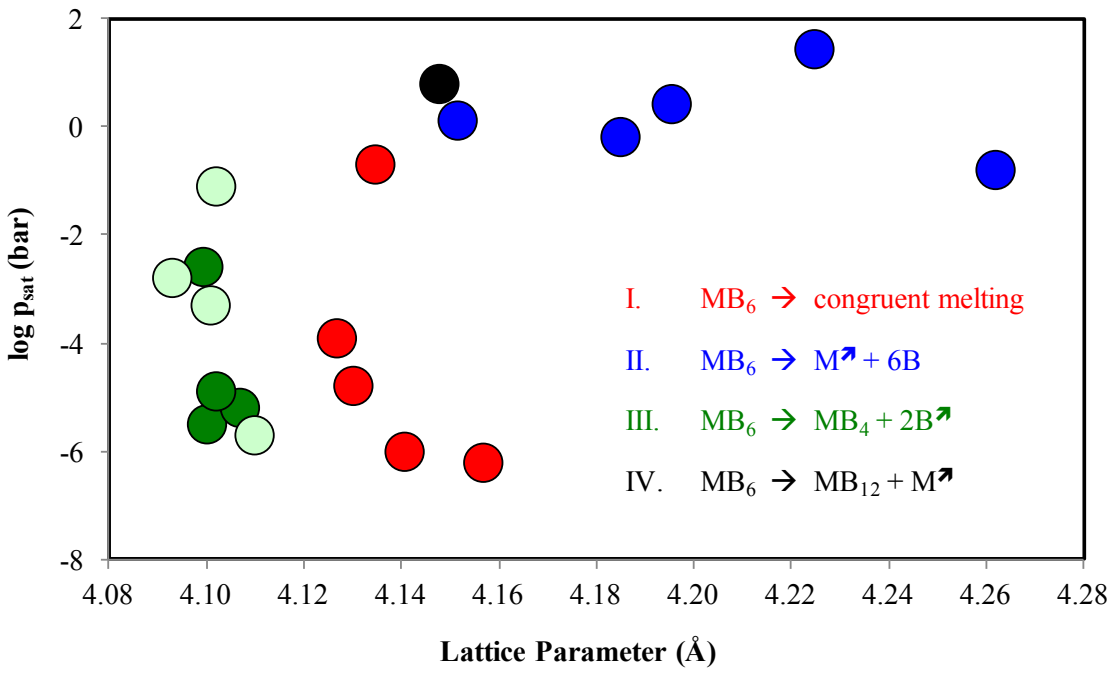

Figure 2 Thermal stability of metal hexaborides plotted as saturation vapor pressure vs. lattice parameter. The colors represent the four types of thermal dissociation.

The greater the saturation vapor pressure of the metal, the greater the volatility and ability of the atom to dissociate from the structure. For two MB_6 compounds with the same lattice parameter, such as CaB_6 and LaB_6, the more thermally stable is that with the least volatile metal (in this case LaB_6). At temperatures right below the melting point the crystalline hexaborides fall into one of four classes of thermal degradation as described by Etorneau and illustrated in Figure 2 [1]. As the saturation vapor pressure of the metal atom increases or the radius decreases, the hexaboride's stability is reduced. The high stability of Group I hexaborides is due in part to a progressive shrinking of the lattice as the volatility of the metal element increases [1]. On the opposite end, the structure's stability also decreases as the lattice parameter increases, due to a reduction in strength of the stretched boron-boron bonds. As seen in Figure 2 the four classes remain fairly grouped together, allowing one to approximate the thermal degradation behavior based on these two parameters. This is useful in the case of several rare-earth hexaboride compounds that have only recently been synthesized and studied, much later than the original work done by Etourneau in the 1970's [1].

While there are many examples of compounds changing structure under the influence of high pressures, it wasn't until 2012 that a high-pressure phase of CaB6 was discovered by Kolmolgorov et al. [13]. The structure transformation was first predicted by density functional theory (DFT) [13] that showed thermodynamic and dynamic instabilities in the CsCl structure and a subsequent reduction in Gibb's free energy by transformation to a stable polymorph.

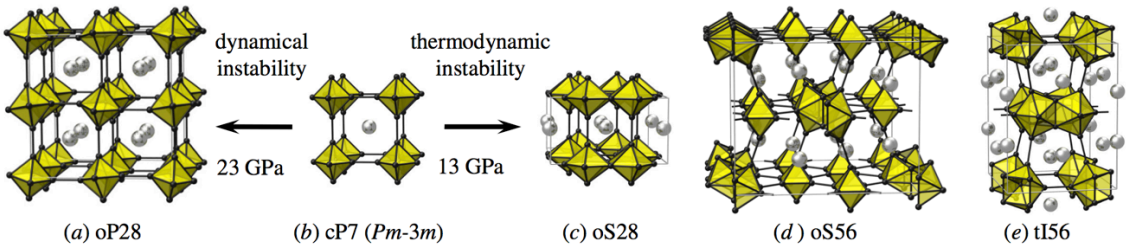

Figure 3 Competing high-pressure structures of calcium hexaboride where b) cP7 (Pm-3m) is at STP, a) oP28 (Pnma) is one of the possible distortions of cP7, c) oS28 (Cmmm) is a metastable structure, d) oS56 (Cmcm) is our lowest enthalpy structure for 13–32 GPa and e) is tI56 (I-4mmm) a new ground state candidate above 32 GPa supported by X-ray data (reprinted with permission) [13].

This was confirmed experimentally by Kolmolgorov et al. who laser-heated CaB_6 up to 42 GPa while performing in-situ X-ray diffraction (XRD) to observe changes in the crystal structure. Figure 3 from Kolmolgorov et al. depicts the stable CsCl structure (cP7) of CaB_6 along with the competing high-pressure structures and the final tetragonal (tI56) structure. Han et al. took the DFT analysis a step further to analyze properties of the high-pressure phase and predicted that the bulk, shear and Young's moduli are larger than that of the low-pressure phase, as well as a reduction in ductility with the transformation to tI56 [14]. This research on phase transformations is important if hexaboride compounds find their way into high-pressure applications, or if the tetragonal polymorph could be quenched and stabilized at room temperature.

1.1.2. Synthesis and Processing

Like many other non-oxide ceramics such as carbides, nitrides and phosphides, the covalently bonded borides are refractory materials with high melting temperatures. This means that high synthesis temperatures are often required to obtain crystalline structures. Synthesis of the first boride compounds in the early 19th century was followed closely by the first hexaborides, produced by Moissan and Williams in 1897

who reduced metal borates with aluminum in an arc furnace to produce CaB_6 and SrB_6 [15]. This process was later refined by Andrieux in 1926, who electrolyzed molten mixtures of metal borates and fluorides [16]. While molten salt electrolysis and solid state reductions were among the first techniques used to produce hexaborides, they have not become obsolete and are still commonly employed methods today. Although there are many different hexaboride synthesis methods to date with varying complexities and nuances, they can all be roughly summarized by four basic classifications: solid state, electrolysis and flux, vapor deposition or metal-gas reactions, and combustion or self-propagation. Specific examples for each group are described in this section, however it should be noted that the synthesis of metal hexaborides is not at all limited to these methods.

1.1.2.1. Solid State Reactions

Solid state reactions are defined here as the mixing of solid precursors and subsequent processing to produce the desired MB_6 compound. These techniques require high purity precursors and elevated temperatures, often above 1000°C, where the compound formation occurs as the precursors decompose into their elemental constituents. Any unwanted or excess lighter elements such as H, C, O, N, or B are usually removed as gases. Two of the most popular solid-state methods for synthesizing hexaborides are the borothermal (Equation 1) [5, 17-33] and carbothermal reductions (Equation 2) [30, 34-42]. Borothermal reductions involve a combination of the desired metal oxide and excess boron, while carbothermal reductions utilize carbon or carbon-metal compounds. Boron-carbon reductions (Equation 3) use B_4C as both the reducing agent (carbon) and boride-former (boron).

$M_mO_n + (6m+n)B \rightarrow mMB_6 + nBO$ (borothermal) Equation 1

$M_mO_n + (3m)B_2O_3 + (10n)C \rightarrow mMB_6 + nCO$ (carbothermal) Equation 2

$M_2 + 3B_4C \rightarrow 2MB_6 + 3CO$ (boron carbide reduction) Equation 3

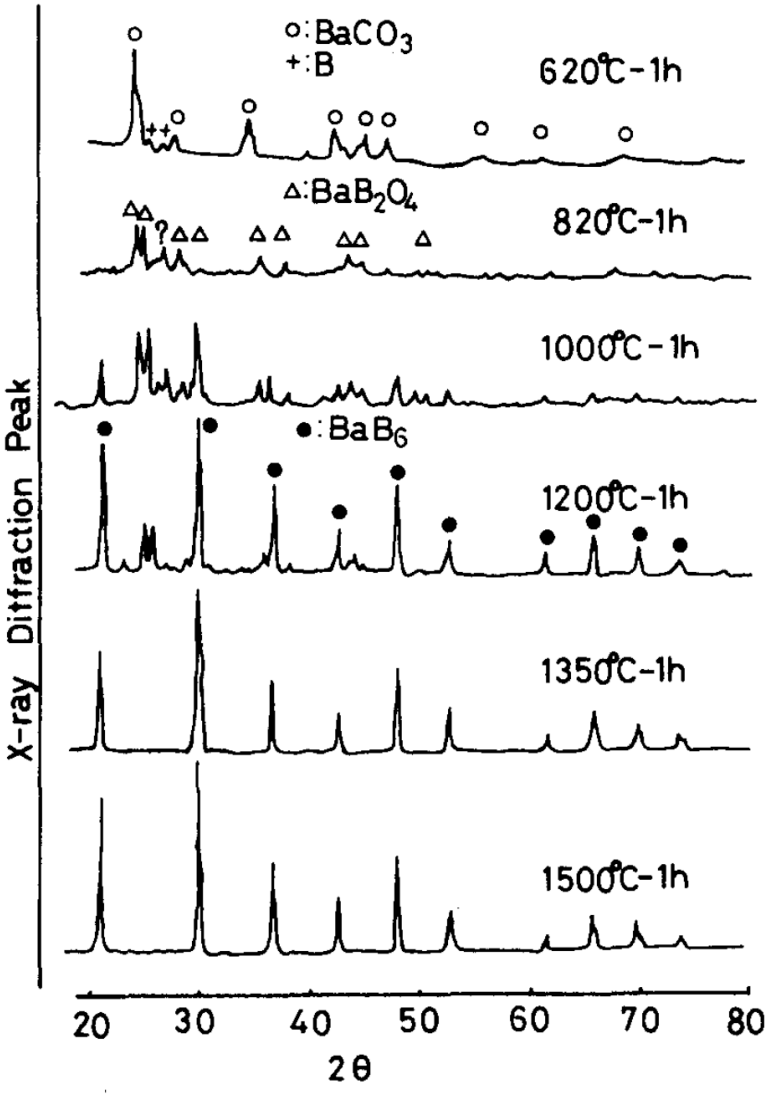

Figure 4 Patterns from the powder X-ray diffraction peaks of the reaction products treated at various temperatures from the starting materials $BaCO_3$ and 7B powders (reprinted with permission) [17].

The combination of metals or metal oxides with boron can be a highly exothermic process, and the reaction may begin to self-sustain at temperatures as low as 200°C [43]. Figure 4 adapted from Aida et al. depicts XRD patterns of the precursors $BaCO_3$ and B gradually turning into BaB_6 with increasing temperature and time [17]. Other examples of solid state reactions include:

1.1.2.2. Direct Reaction of Elements

Ultra-high purity metal and boron are mixed together and heated in a crucible (all under an inert atmosphere) to the boiling temperature of the metal for several hours to ensure homogeneous mixing [2, 12, 44, 45]. This produces hexaboride compounds of purity corresponding to that of the elemental precursors, however, it is not often used due to the reactivity of the metal precursors with oxygen.

1.1.2.3. Reaction of Metal Chlorides and MgB_2

Hydrated rare-earth chlorides and magnesium diboride powders can be heated under an argon atmosphere in a tube furnace. Aprea et al. synthesized ReB_6 compounds at the relatively low temperature of 923 K (albeit containing a level of contamination in the crude materials, later washed away with HCl) [46].

1.1.2.4. Mechanochemical Reactions

Mechanochemical reactions are the only method in this group not to rely on external heating, but rather on the energy produced by collisions between the precursor particles and milling media. Balcı et al. synthesized CaB_6 through high-energy ball milling using calcium metal and B_2O_3 powders in an argon-filled steel vial with steel media for 6 hours at 1200 rpm [47].

1.1.2.5. Reactive Sintering

Reactive SPS is a one-step synthesis and consolidation process used by Bao et al. to produce $La_xGd_{1-x}B_6$. By combining lanthanum and gadolinium hydrides with boron and then heating the mixture to 1773 K at 50 MPa in the SPS, fully-dense (>97%) hexaborides formed as the hydrogen diffused out in the form of H_2 gas [48].

1.1.2.6. Floating Zone Melting

Floating zone melting utilizes pure metal or metal oxide precursors mixed with excess boron and melted together under argon to form precursor rods which are then heated under vacuum in a specific molten zone that is then cooled to crystallize the material. A similar method called zone leveling uses a zone with a temperature and composition on an adjacent liquidus line that is then moved to precipitate crystals out of the molten solution. Floating zone methods are capable of producing large single crystals without any crucible interaction, but can be challenging with some hexaboride compounds that display incongruent melting. Figure 5 from Otani et al. depicts the La-B phase diagram along with a schematic of a typical floating zone setup [11, 49-59].

1.1.2.7. Melt Electrolysis and Flux

Melt electrolysis and flux are techniques used to grow crystals of material within a molten bath, with the main difference between the two being the application of a current (electrolysis). Electrolysis, or electrochemical synthesis, most often utilizes a bath of molten salts [60-66] to dissolve the metal and boron precursors, although other options such as molten borates [67] can be used. The electrolytically dissolved metal and boron ions within the melt deposit on the cathode and crystallize into MB_6 compounds.

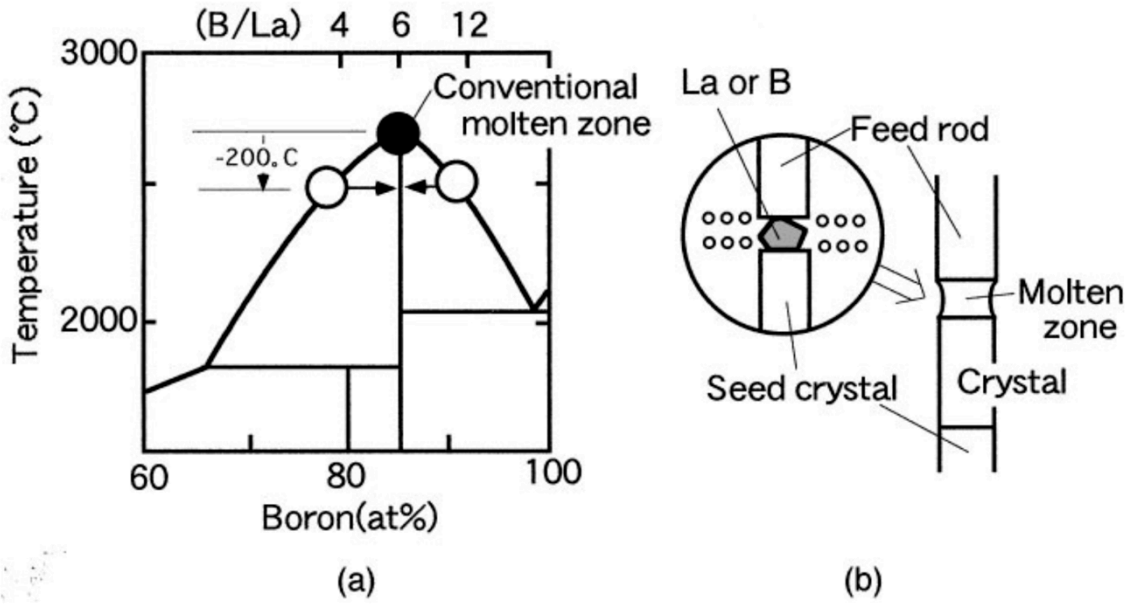

Figure 5 a) Phase diagram of the La-B system and b) the traveling solvent floating zone method by which the high-quality crystals, free of boundaries, can be prepared (reprinted with permission) [59].

The materials used for the cathode (rod) and anode (crucible) vary based on the salts and targeted metal cation, but popular choices include tungsten or molybdenum cathodes and graphite or glassy carbon crucibles. Current densities range from 0.2 to 2 A/cm^2 and synthesis temperatures hovering around 1273 K [60-66]. Melt electrolysis produces polycrystalline growths on the cathode surface and some results indicate increasing grain size with increasing current density [60]. The aluminum flux [55, 68-81], a specific form of the solution-melt method, has the distinct advantage of producing high purity MB_6 single crystals, often several millimeters in length. Due to the metallic character of the bonds in refractory borides, suitable high-temperature solvents are practically limited to metals [78]. Although no metal has been found to perfectly meet all the requirements, molten aluminum and germanium offer the best compromise and the reducing power of aluminum has proven itself over time and it remains the most popular

solvent choice. While this technique was often used in the past to produce crystals of near-perfect stoichiometry, recent studies have shown that the stoichiometry actually varies along the length of the crystal, but only by small amounts ($^{dB}/_{M}$ ~0.3) [72]. Figure 6 shows SEM images of (La-Ce)B_6 crystals grown by Gurin et al. with corresponding plots containing the B/Ce and B/(La+Ce) ratio along length of a crystals. A typical experimental set-up involves the heating of high-purity aluminum ingots with the desired precursors in an alumina or aluminum nitride crucible under flowing argon atmosphere to around 1673 K, followed by a slow cool to room temperature. The MB_6 crystals are then removed by dissolving the aluminum matrix in either HCl or NaOH.

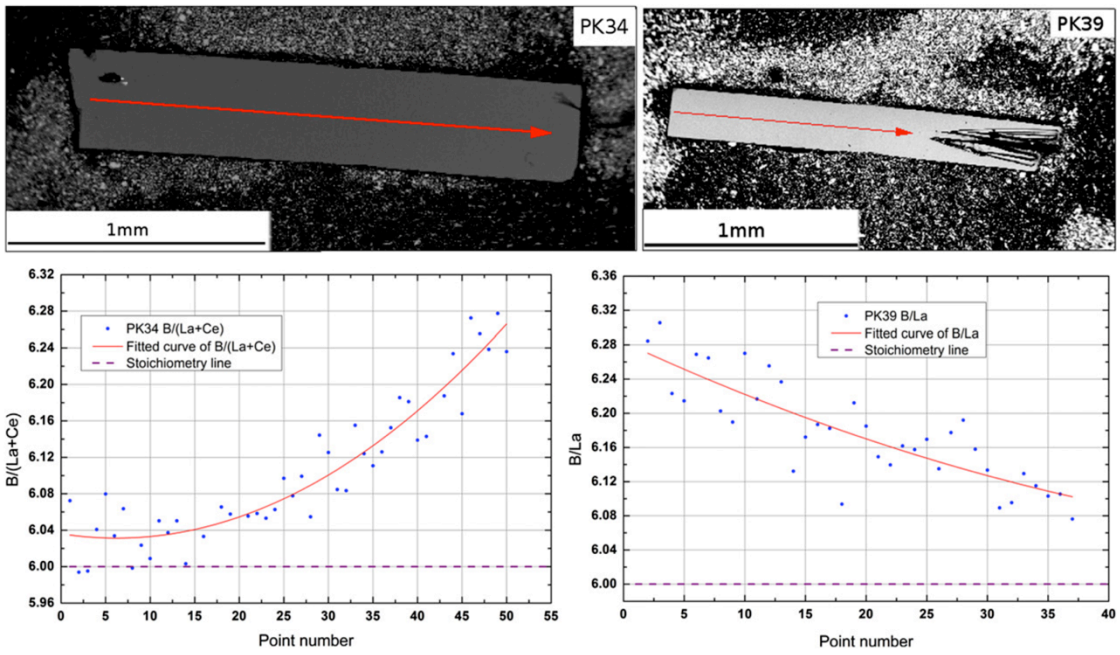

Figure 6 BSE images of elongated plate crystals of LaB6 and its Ce solid solutions obtained in a solution-melt of Al (Samples PK34, PK39, *sm*). Red line shows direction of scanning. The plots show B/Ce and B/(La+Ce) ratio along length of a crystals (reprinted with permission) [72].

Although the crystals are often very high purity, impurities may take the form of aluminum inclusions [72] (as low as 0.02 wt.%) or iron [59, 74, 82, 83] (~0.03 wt.% as a result of matrix removal), with the former being easy to locate and avoid.

While the various reactions listed above are capable of producing hexaboride compounds of high purity and stoichiometry, it often comes at the price of high synthesis temperatures and ultra-pure precursors, adding to the overall cost of the experiment. However, these methods remain the most commonly used for producing bulk amounts of material (thermal reductions) and large single crystals (flux). If nanostructured hexaborides are desired, the following synthesis methods can be used to produce hexaborides:

1.1.2.8. Vapor Deposition and Metal-Gas Reactions

Vapor deposition and metal-gas reactions are commonly used to produce nano-structured materials and their application in hexaborides includes the synthesis of nanowires [84-93], nanobars [94] and nanoobelisks [95]. These types of reactions include, but are not limited to the various types of vapor deposition described below:

I. Chemical vapor deposition (CVD) synthesis for hexaboride materials often involves a metal precursor (M_nCl_m, M_nO_m,) heated under the flow of boranes ($B_{10}H_{14}$, B_2H_6, B_5H_9) that grows crystals on an upstream wafer. This process is sometimes accompanied by a catalyst such as Ni [84, 86, 87, 93], especially when metal oxide precursors are used. CVD reactions for hexaborides typically occur at temperatures between 1073-1273 K. Figure 7 contains SEM images of LaB_6 nanoobelisks grown by Brewer et al. using lanthanum chloride and decaborane. In similar fashion to the 1D hexaboride structures produced by CVD using metal

oxides or metal chlorides with borane gas, a reaction of pure metal and boron trichloride gas can produce hexaboride nanowires with and without the use of a catalyst. Flowing boron trichloride and hydrogen gas over metal precursors results in the formation of hexaborides and hydrochloric acid. Reaction temperatures for the synthesis of hexaborides typically range between 1273-1423 K [3, 88-92, 96-98].

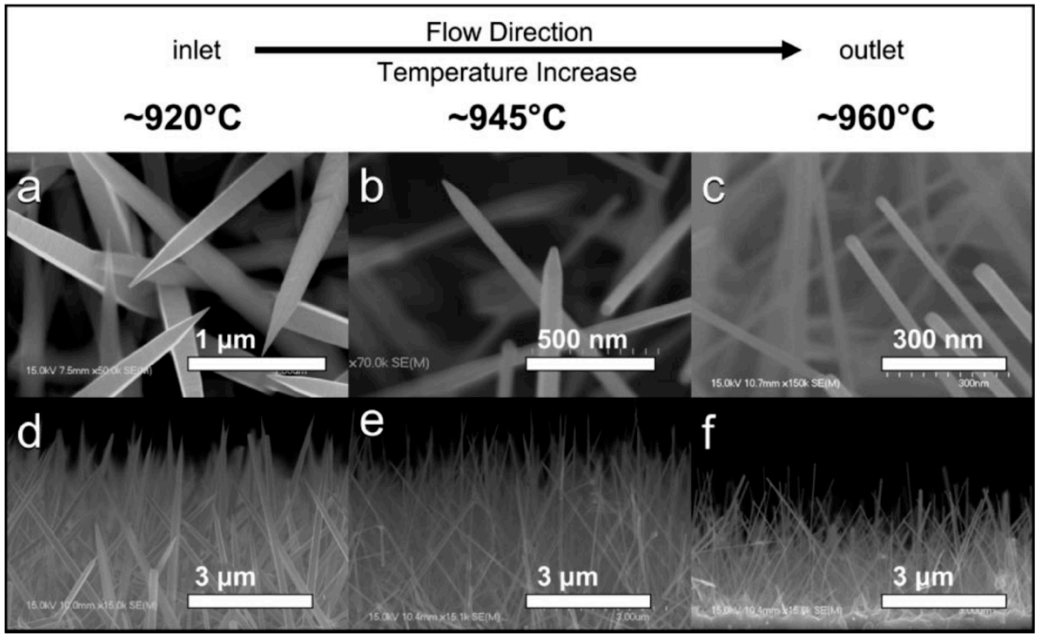

Figure 7 Typical SEM images of LaB_6 nanoobelisks and nanowires synthesized with substrates placed (a) 3, (b) 4, and (c) 5 cm downstream from the $LaCl_3$ precursors. (d-f) Zoom-out SEM images of the nanostructures in a-c, respectively (reprinted with permission) [95].

II. Unlike CVD, physical vapor deposition (PVD) of hexaboride compounds is based on non-reactive techniques [99-104]. This can be accomplished by triode sputtering (Figure 8) [103], magnetron sputtering [99] electron beam evaporation [102] and arc evaporation [104] for the deposition of hexaboride coatings. As these types of non-reactive processes involve the vaporization of a hexaboride

target instead of metal and boron precursors, they may be considered as more material rearrangement than material synthesis. Nevertheless, PVD is capable of producing thin film and coatings of hexaboride compounds.

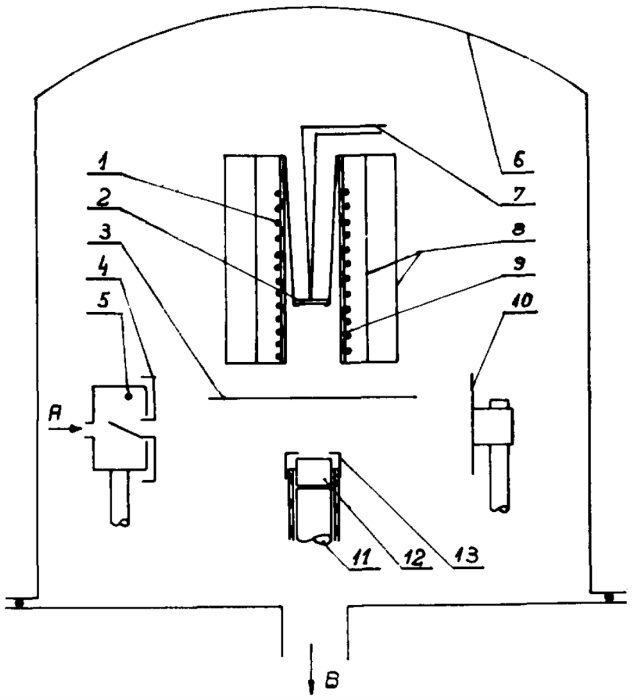

1 - heater
2 - substrate
3 - shutter
4 - accelerating electrode
5 - filament
6 - stainless steel bell jar
7 - thermocouple
8 - radiation shield
9 - quartz tube
10 - anode
11 - target holder
12 - target (LaB_6 rod)
13 - shield

A - argon inlet
B - to the vacuum system

Figure 8 The apparatus used for lanthanum hexaboride film deposition by the cathode sputtering method (reprinted with permission) [103].

Thermal plasma reactors can also be used to evaporate solid precursors and cause the nucleation of desired compounds from supersaturation of the vapor phase. Szepvolgyi et al. injected lanthanum oxide and amorphous boron through an RF inductively coupled plasma flame, resulting in precursor vaporization and nucleation followed by water cooling to produce agglomerates of spherical LaB_6 particles 10-50 nm in size [105].

1.1.2.9. Combustion Synthesis

Combustion and self-propagation represent a broad range of reactions all involving the ignition of materials to drive the formation of hexaboride compounds. These methods utilize various precursors, temperatures and pressures, including but not limited to:

I. Combustion of metal nitrates, lithium tetraborate and citric acid under argon at 873 K to produce hexaboride powders with a crystallite size of ~200 nm [106].

II. Combustion of metal oxides and boron oxide with magnesium powder mixed in as an ignition source to produce hexaboride powders with a particle size of ~1 μm [107, 108].

III. Combustion of metal borates with magnesium at 973 K using the magnesium as an ignition source and reducing agent to produce hexaboride powder. [109]

IV. Solution combustion of metal nitrates, amorphous boron and carbohydrazide at 593 K to produce hexaboride powders with a particle size of ~500 nm [110, 111].

V. Reaction under autogenic pressure at elevated temperature (RAPET) of metal acetates and sodium borohydride ($NaBH_4$) in a nitrogen environment within a closed stainless steel cell heated to 1173 K to produce hexaboride powders with a particle size of 200 nm – 10 μm [112].

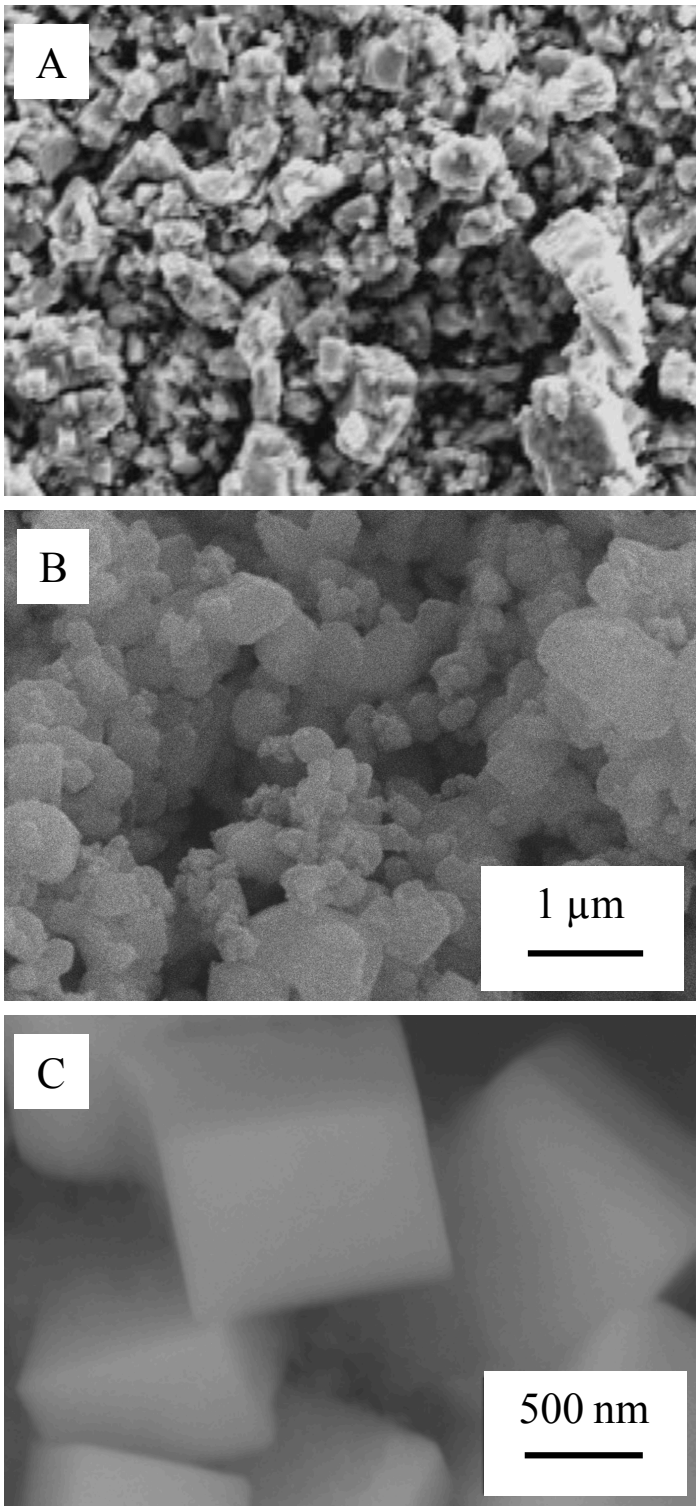

Figure 9 SEM images of a) CeB_6 produced by Amalajyothia et al. using metal nitrates, lithium tetraborate and citric acid [106], b) CeB_6 powders produced by Dou et al. using metal oxides, boron oxide and magnesium powder [108] and c) LaB_6 produced by Kanakala et al. using solution combustion of metal nitrates and boron [111] (reprinted with permissions).

1.1.3. Properties

Borides are represented by vast number of compounds with unique properties, including refractory melting temperatures [113], high hardness [114, 115], wear resistance [116], chemical inertness (especially towards liquid metals [117]) and superconductivity [118].

Table 2 Typical properties of some borides (adapted from T. Lundstrom) [119].

Compound	Melting Temperature (K)	Microhardness (GPa)	ΔH_f (kJ/mol)	Resistivity ($\Omega m 10^8$)	T_c (K)
MgB_2	1100[a]	11	-92	16	39
TiB_2	3500	33	-280	7-15	
ZrB_2	3450	29.4	-305	7-10	5.5
CrB	2400	12-13		45	
CrB_2	2500	21	-130	21-56	
Fe_2B	1660[a]	13.5		38	
FeB	1925	19	-38	80	
CaB_6	2770	27	-120	>200	
LaB_6	3000	27.7	-400	7-15	0.12
CeB_6	2825	30	>-350	29	
α-AlB_{12}	1725[a]	37		10^5	
YB_{66}	~2300	38		$360x10^6$	
h-BN		2.3	-255	insulator	
c-BN	~2700	60-70		insulator	
B_4C	2725	45	-242	10^5 - 10^7	

[a] Decomposes

Hexaborides are no exception, and even excel in certain categories when compared to other types of ceramics. Table 2 compares several properties of various boride compounds, including that of CaB_6, LaB_6 and CeB_6 [119]. As the physical properties of hexaborides are derived mostly from the covalently-bonded boron framework, they vary only slightly from compound to compound [2]. On the other hand, the electronic and magnetic properties of these compounds are highly influenced by the corresponding metal cation and its valency. As with any new and emerging field there are sometimes conflicting theories on the origin of hexaboride's unique properties, and the following sections are aimed at presenting these various arguments for the thermal, electrical, superconductivity, magnetic and mechanical properties.

1.1.3.1. Thermal Behavior

Thermal properties of hexaborides have been represented in literature by both theoretical [120, 121] and experimental studies [122, 123], with the latter being a bit less common. Although the thermal stability has been previously covered in *Structure and Bonding*, it is of course worth noting again the high melting temperatures of the hexaboride family due to the strong covalent bonds within the boron sublattice. The boron-boron bond length is represented by both the inter-octahedral (between) and slightly longer intra-octahedral (octahedra edge) bonds. Chen et al. found that for hexaborides of Ca, Sr, Ba, Y and La the thermal expansion coefficients (α) seen in Figure 10 correspond to the difference between the $B–B_{intra}$ and $B–B_{inter}$ distance and that that the product of α(T) and T_m are constants, 0.019 (rare-earth) and 0.016 (alkaline-earth) [69].

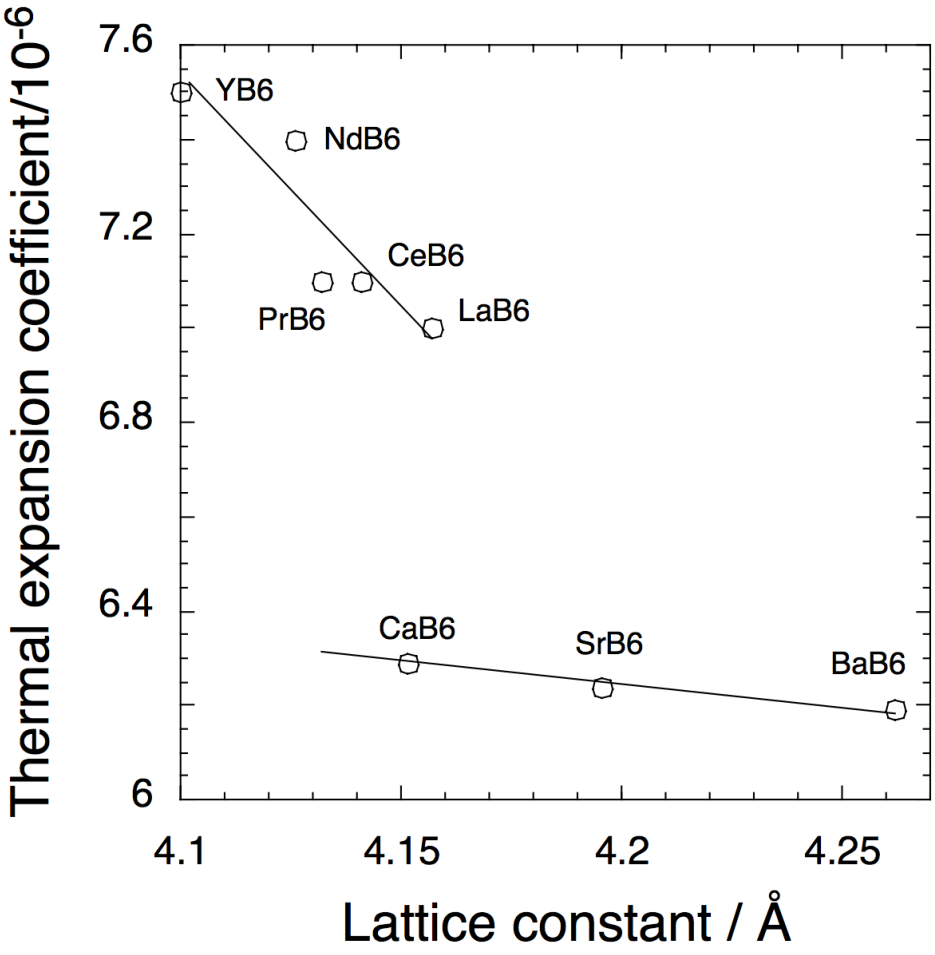

Figure 10 Thermal expansion coefficients for some hexaborides vs. the lattice constant (reprinted with permission) [69].

Sirota et al. carried out an extensive study of the thermal expansion coefficients for various rare-earth hexaborides over the low-temperature range of 5 - 320K and separated out the lattice contribution for both α(T) and heat capacity (C_p) [122]. Figure 11 depicts the linear coefficients of thermal expansion for these compounds, and it was noted that the low-temperature local maximums for CeB_6, PrB_6, GdB_6, TbB_6, and DyB_6 correlate with anomalies in the heat capacity and most likely result from the Jahn–Teller effect [122].

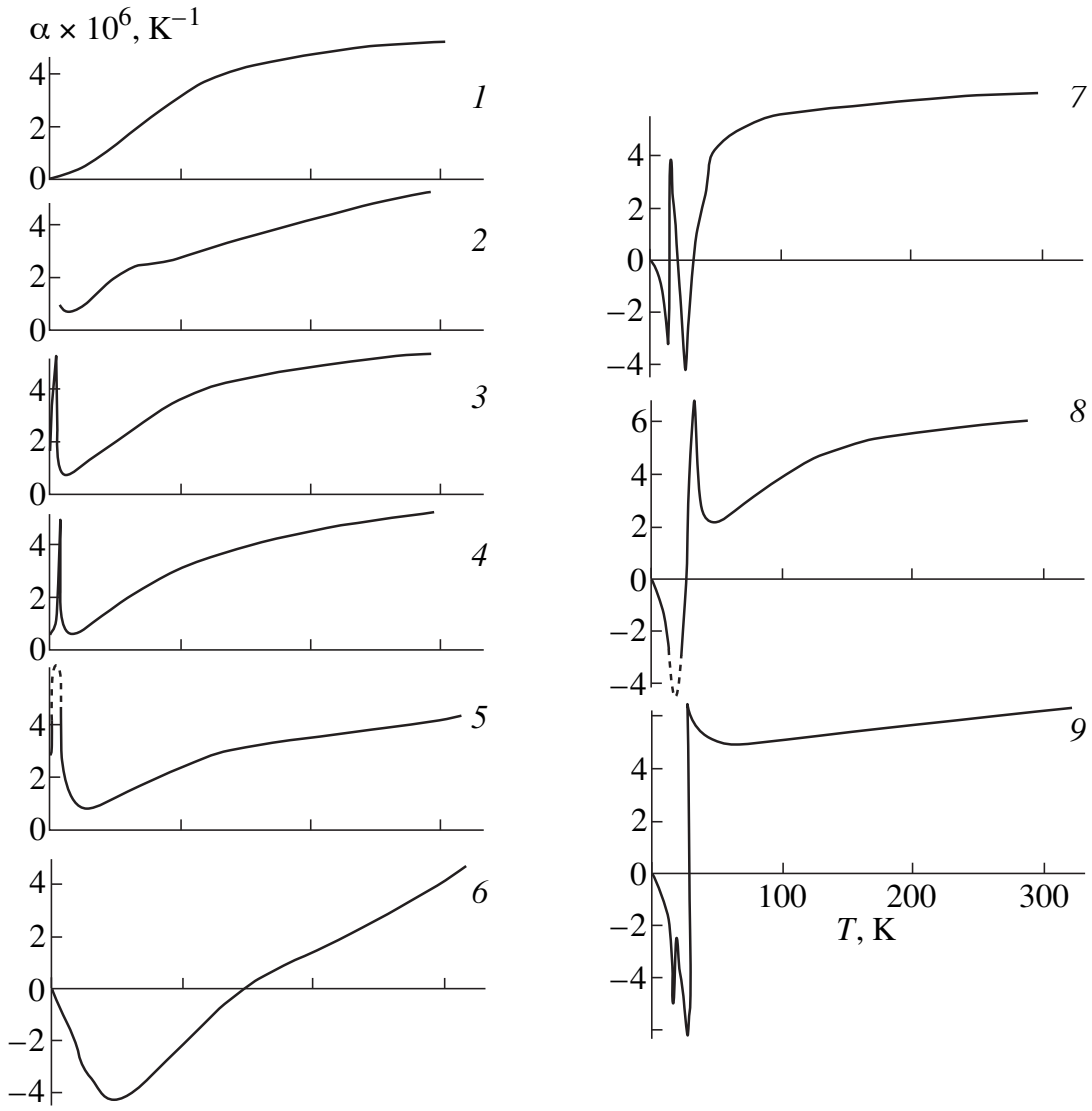

Figure 11 Temperature dependences of the linear thermal expansion coefficient *α(T)* for 1) LaB_6, 2) CeB_6, 3) PrB_6, 4) NbB_6, 5) SmB_6, 6) EuB_6, 7) GdB_6, 8) TbB_6 and 9) DyB_6 (reprinted with permission) [122].

On the higher end of the temperature spectrum, Guo-Liang et al. performed first-principal calculations using density functional theory to obtain the thermal expansion coefficient and heat capacity for LaB_6 at various pressures (Figure 12). In agreement with the results from Sirota et al. they observed a leveling of α(T) at elevated temperatures [120].

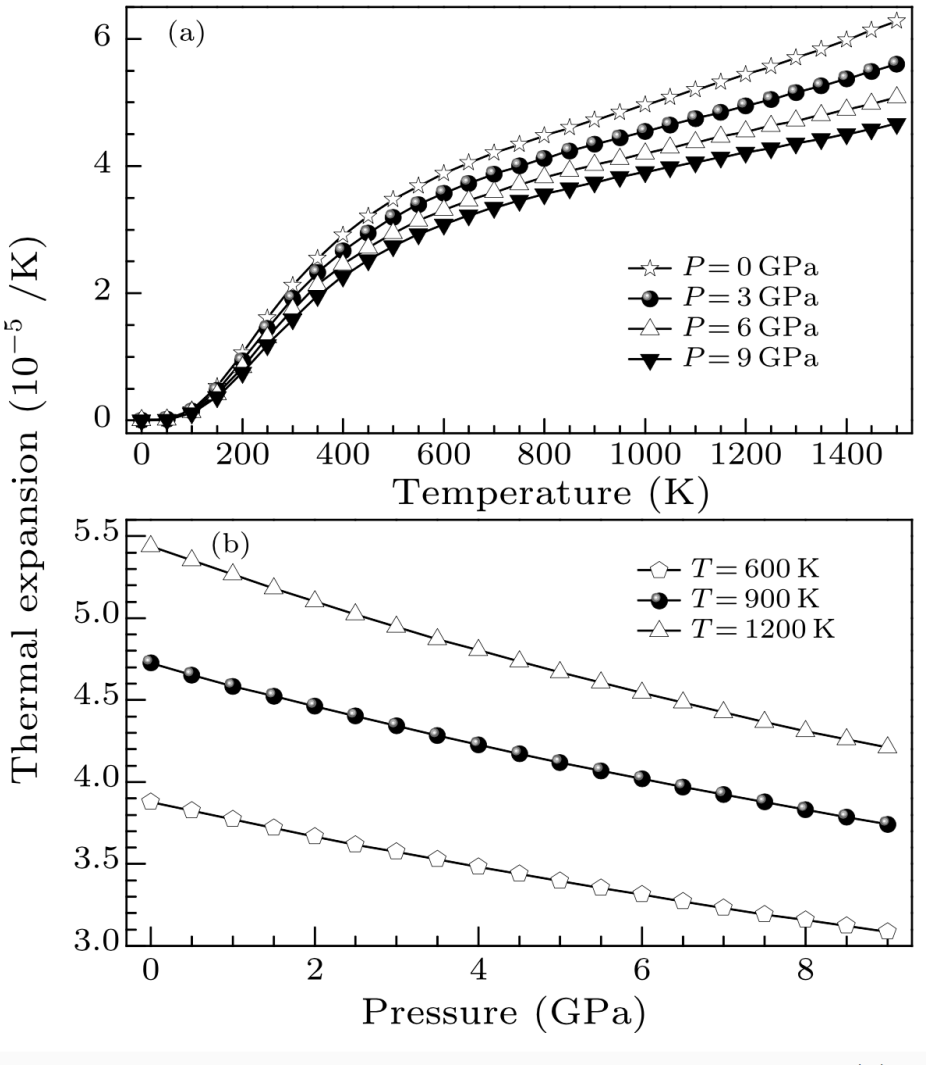

Figure 12 Variation of the thermal expansion coefficient (α) with temperature (T) at P = 0, 3, 6 and 9 GPa, and (b) with P at T = 600, 900 and1200 K (reprinted with permission) [120].

In a series of studies on the thermoelectric potential of hexaboride compounds, Gursoy et al. reported the specific heat, thermal diffusivity and thermal conductivity for CaB_6, SrB_6, BaB_6 and the ternary solid solutions $Ca_xSr_{1-x}B_6$, $Ca_xBa_{1-x}B_6$ $Sr_xBa_{1-x}B_6$ between 300 and 1100 K [45]. As seen in Figure 13, these properties agree with standard trends for insulating ceramics such as decreasing thermal conductivity with increasing temperature.

It was noted by the authors that the noticeably low thermal conductivity of $Ca_{0.75}Sr_{0.25}B_6$ and corresponding low electrical conductivity suggests a very low carrier concentration, and that the reduction of the thermal conductivity was a result of introducing a larger cation (Sr^{2+}) and subsequent change in the electronic situation resulting in different scattering mechanisms [45]. Similar results were observed for solid solutions of $Ca_xBa_{1-x}B_6$, although it is interesting that the conductivities were not as low considering the larger size difference between Ca^{2+} and Ba^{2+} ions.

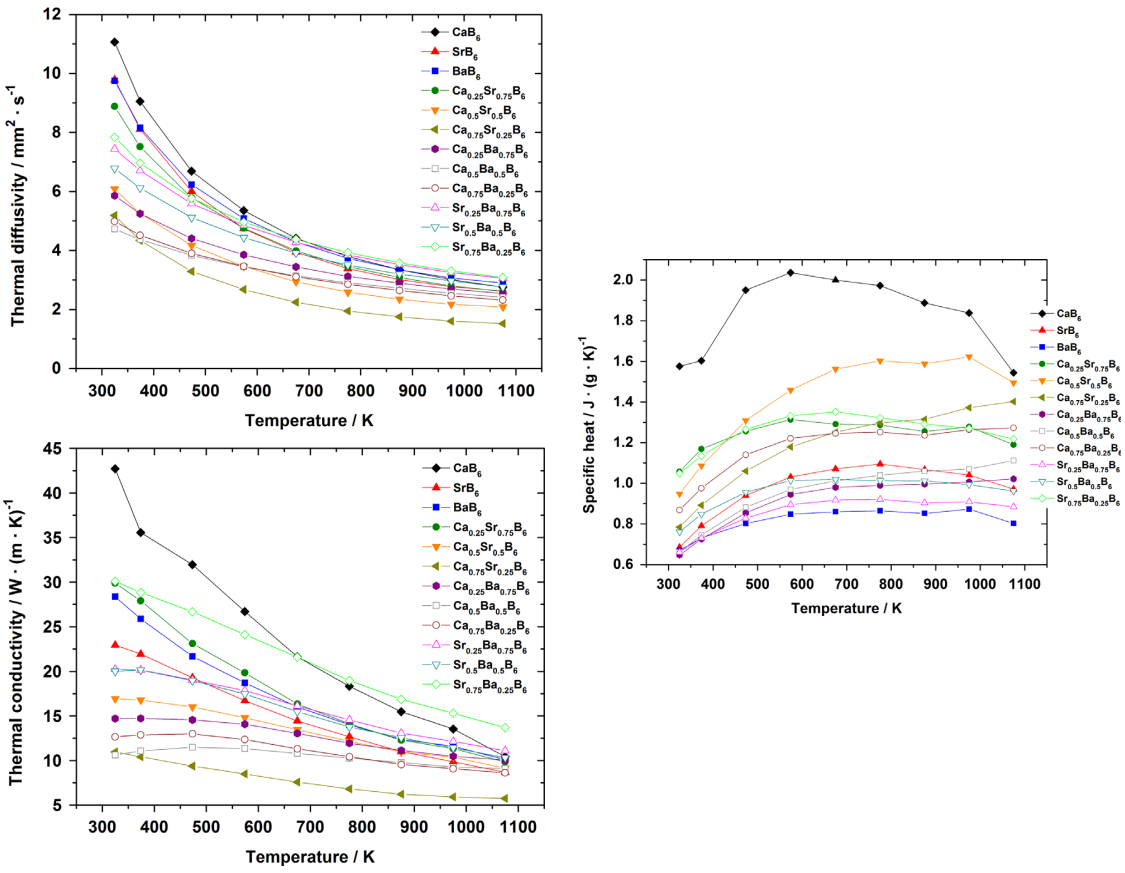

Figure 13 Values for a) specific heat, b) thermal diffusivity and c) thermal conductivity for CaB_6, SrB_6, BaB_6 and the ternary solid solutions $Ca_xSr_{1-x}B_6$, $Ca_xBa_{1-x}B_6$ $Sr_xBa_{1-x}B_6$ between 300 and 1100 K (reprinted with permission) [45].

1.1.3.2. Electrical Behavior

Electronic conductivity is where hexaboride compounds really begin to display their unique range of properties. This stems almost directly from the bonding of the MB_6 structure, in which the covalently-bonded boron atoms "trap" the metal atom, the main purpose of which is to donate electrons to the charge deficient boron sublattice. The number of donated electrons has been experimentally and theoretically determined to be 2 [10, 11], making divalent hexaborides semiconductors and trivalent compounds metallic [1, 2, 54]. However, very low levels of doping or impurities (0.5%) can cause divalent compounds to exhibit metallic behavior [77, 124, 125]. Mandrus et al. fit experimental resistivity data for LaB_6 using a modified Einstein Bloch-Grüneisen model that treats the La ions as independent Einstein oscillators embedded in a boron framework treated as a Debye solid (Figure 14) [126].

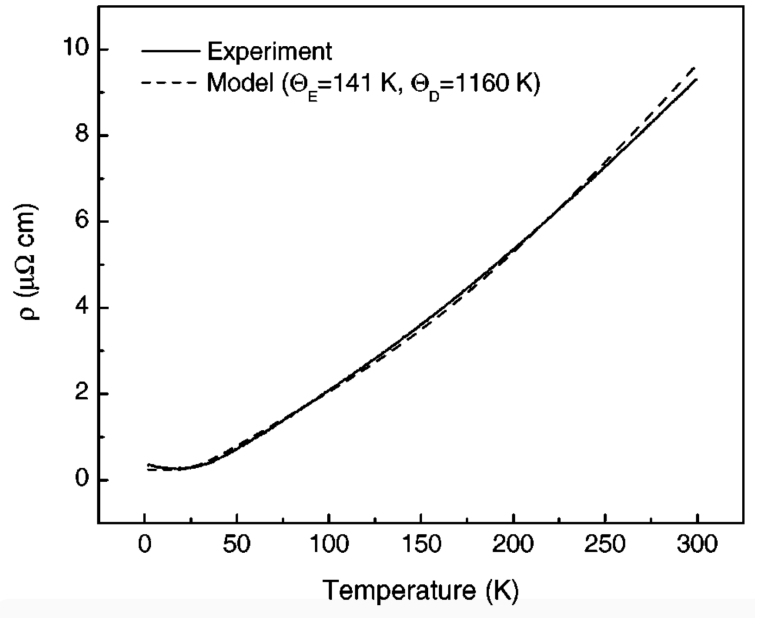

Figure 14 Resistivity of LaB_6 and a model that incorporates scattering form localized vibrations of the La ions ($\boldsymbol{\Theta}_E$ = 141 K) and a Bloch-Grüneisen contribution from the boron framework ($\boldsymbol{\Theta}_D$ = 1160 K) (reprinted with permission) [126].

As seen in Figure 14, the resistivity of LaB_6 decreases with decreasing temperature below 300 K, a typical characteristic of metallic materials. While the resistivity of trivalent hexaborides may be metallic in nature around room temperature, extreme low temperatures can produce alternate behaviors as seen in CeB_6 [55]. Petrosyan et al. grew CeB_6 single crystals by floating-zone and aluminum flux and found that the resistivity begins to increase below 150 K, noting that the resistivity of the crystals obtained by the flux method was higher than that of the floating-zone crystal over the whole investigated temperature range, most likely due to aluminum and oxygen impurities in the flux crystal [55].

While the donation of two electrons to the boron framework would suggest semiconductor behavior from the divalent hexaboride compounds, that is not always the case. Even for SrB_6, a model divalent hexaboride, metallic characteristics are observed at high temperature [5, 31], around room temperature, and again below 0.5 K [77]. To further understand the physical properties at low temperature, Ott et al. performed a detailed study on the crystal structure, electrical conductivity, specific heat, heat capacity and electronic excitation spectrum of SrB_6 and their finding indicate that the electrical resistivity of the material changes from metallic to semiconducting between at approximately 250 K, as shown in Figure 15 [77]. The authors concluded that the mean free path for the conduction electrons is sizable, that the Fermi wave vector (k_F) related to the ranges of metallic character must be rather small, and that the sharp drop in resistivity below 0.5 K is accompanied by similar behavior in $C_{p,ex}$ vs T [77].

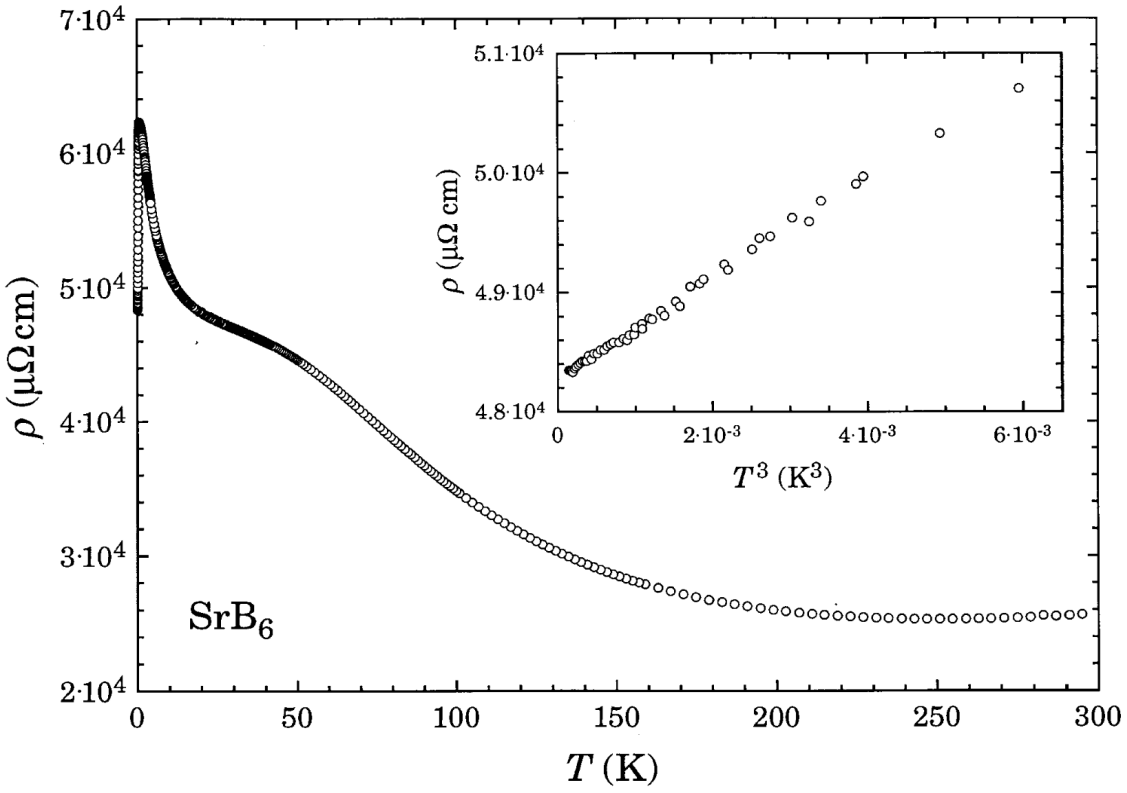

Figure 15 Temperature dependence of the electrical resistivity of SrB_6 between 0.05 and 300 K (reprinted with permission) [77].

At higher temperatures the results vary, with some divalent hexaborides exhibiting conductivity of metallic character and some of semiconductor, as shown by Takeda et al. in their study of the thermoelectric potential of hexaboride compounds [5, 31, 127]. Figure 16 contains the electrical conductivities from one such study for several hexaboride compounds up to 1073 K, clearly showing the metallic character for all compounds except YbB_6 [5]. The unusually high conductivity of alkaline-earth hexaborides has been described in terms of both overlapping band gaps and carrier concentration, with the influence of impurities and metal vacancies being quite apparent in experimental results [125]. This phenomenon has also been explained by more recent

band gap calculations showing that the changes in $B–B_{intra}$ and $B–B_{inter}$ distances can easily effect the electronic properties, resulting in slight band overlapping and a shift from semiconducting to semi-metallic [9, 21, 128].

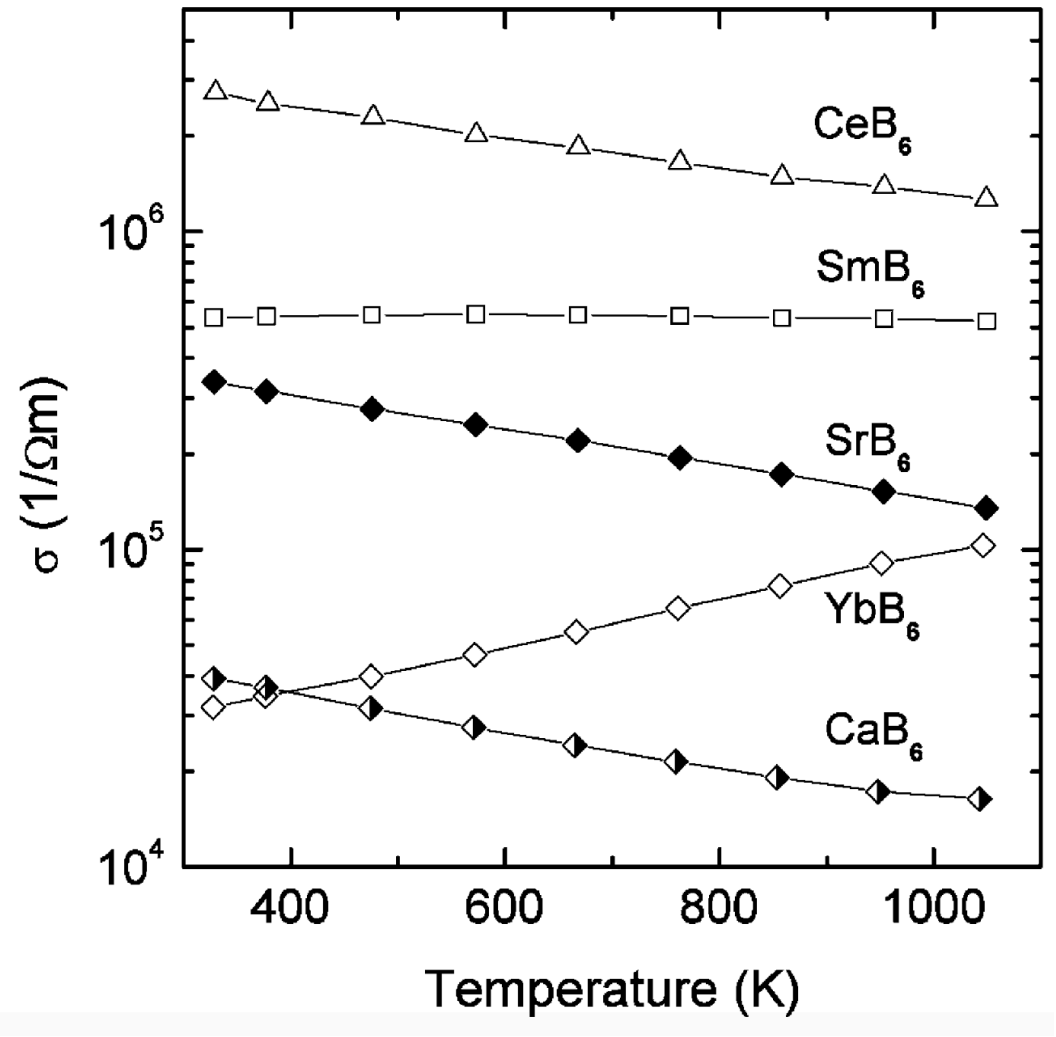

Figure 16 Temperature dependence of electrical conductivities of some hexaborides (reprinted with permission) [5].

It is important to note that unlike most rare-earth hexaborides, the large lattice parameters for the compounds EuB_6 and YbB_6 coupled with magnetic and Mössbauer measurements indicate that europium and ytterbium are in the 2+ oxidation state, thus explaining the small-gap semiconducting nature of YbB_6 [5]. While Mercurio and Etourneau observed semiconducting behavior for pure EuB_6 in their study of $LaEuB_6$ solid solutions, their early works failed to capture the low-temperature behavior of EuB_6 with regards to electrical conductivity. More recent electronic structure calculations [79, 129] indicate that small dilations of the boron octahedra result in an overlap of the conduction and valence bands in EuB_6, imparting semi-metallic character.

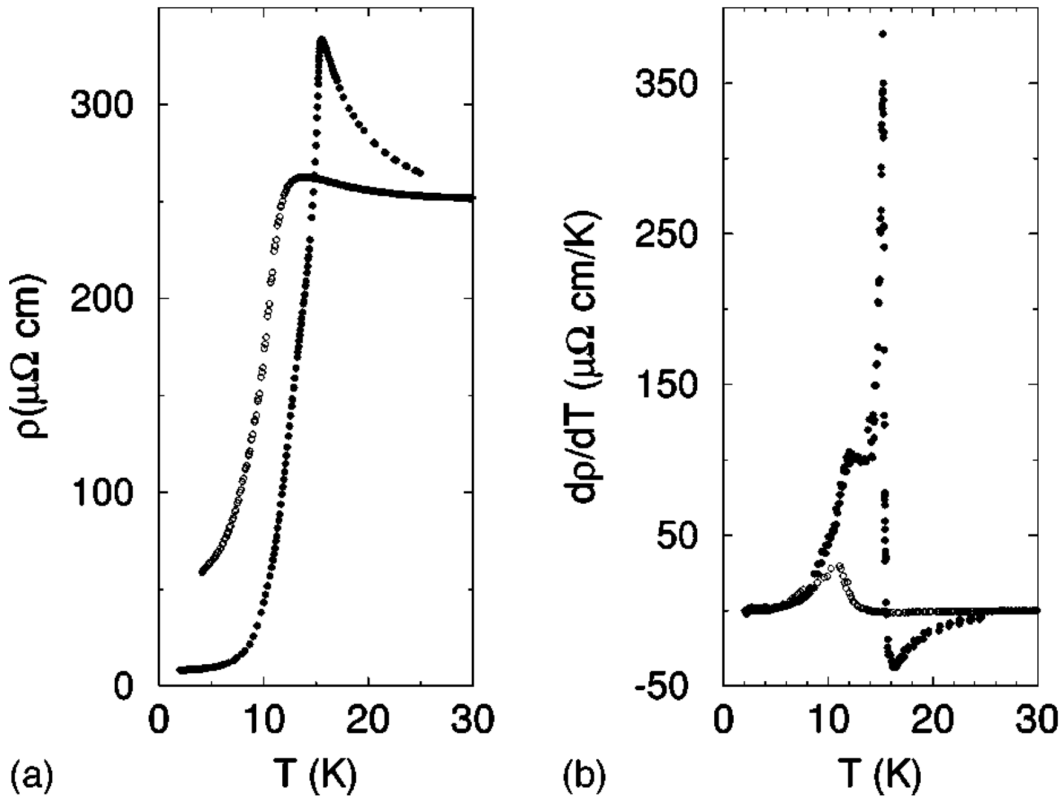

Figure 17 A comparison of the temperature dependences of the electrical resistivity (a) and the temperature derivative of the resistivity (b) for two single crystals of EuB_6 (reprinted with permission) [79].

This behavior, as illustrated in Figure 18, can be seen as the resistivity increases with decreasing temperature followed by a sharp drop around 12 K as the material transitions into the ferromagnetic-metal ground state [27, 79, 130, 131]. $La_{1-x}Eu_xB_6$ compounds are often studied due to the controlled nature in which the dramatic shift from semimetal to metal caused by the substitution of La^{3+} ions for Eu^{2+} ions can be observed [1, 27, 54, 79, 130, 131]. Figure 18 from the work by Snow et al. demonstrates the obvious difference between samples of $x \leq 0.01$ and $x \geq 0.03$ at low temperatures [130].

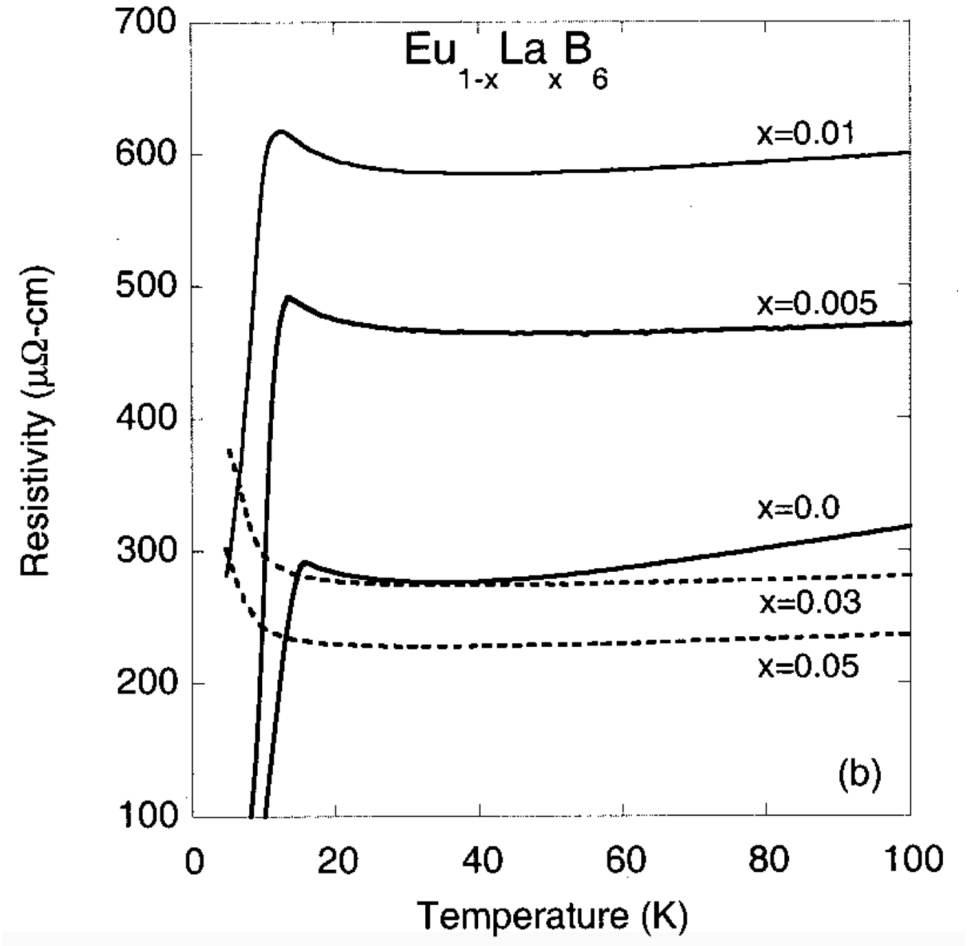

Figure 18 Resistivity vs. temperature. The paramagnetic semimetal to ferromagnetic metal transition temperatures are 15.4, 13.7 and 12.45 K for the $Eu_{1-x}La_xB_6$ for x=0.005 and x=0.01 samples, respectively, as determined by the position of the peak in dp/dT^4 (reprinted with permission) [130].

An increased lattice parameter has a similar effect on the valency of samarium in SmB_6, although not quite as much as in EuB_6 and YbB_6, resulting in a "mixed valency" hexaboride. This curious compound has sparked detailed research for nearly half a century; due mostly in part to the transition from metallic to semiconducting behavior with decreasing temperature [54, 132]. Figure 19 depicts the low temperature conductivity from a study by Flachbart et al. on single crystals of SmB_6 [133]. At low temperatures, SmB_6 displays narrow energy and spin gaps that stem from the hybridization between the narrow states formed by electrons of the samarium 4*f* shell and the wide conduction band formed by both boron *p* states and Sm 6*s* states [133, 134].

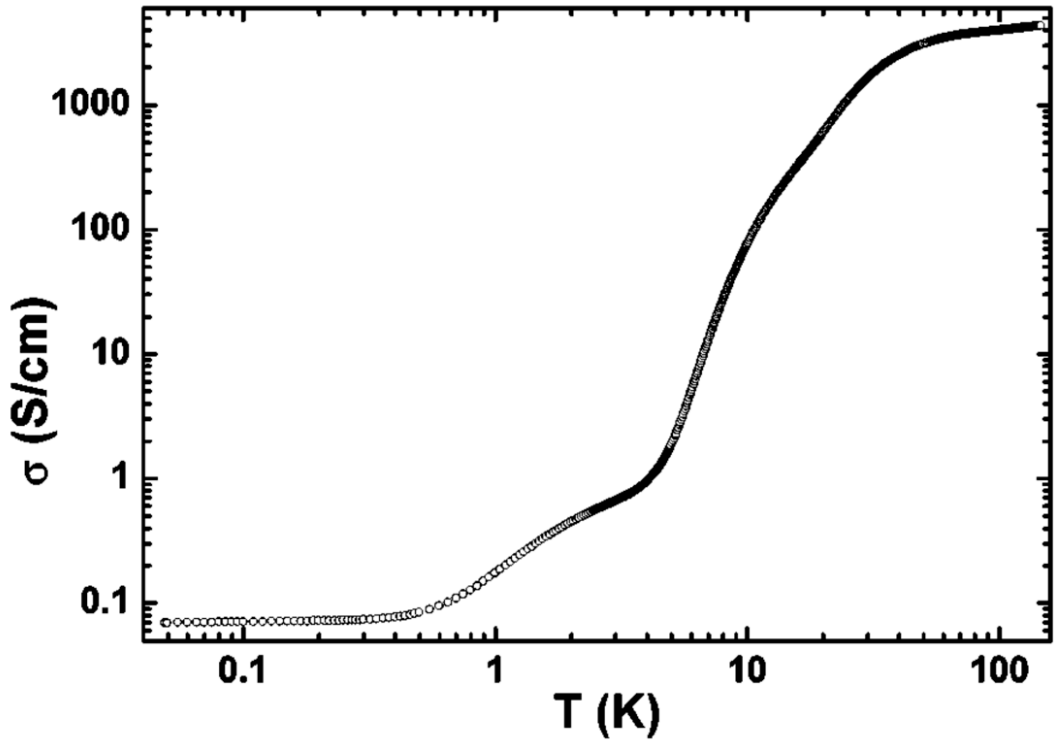

Figure 19 Electrical conductivity vs. temperature T of the bulk SmB_6 sample (reprinted with permission) [133].

This electrical conductivity behavior is also effected by pressure induced transition of Sm towards the trivalent state; from 2.6+ to 2.75+ between 1 bar and 60 kbar that occurs smoothly without any structural changes [135-137]. High pressure studies of the resistivity of SmB_6 have been carried out to 220 kbar by Beille et al., 60 kbar by Berman et al. and 66 kbar by Cooley et al. [135, 136, 138, 139]. Figure 20 depicts the effect of pressure on resistivity at low temperature.

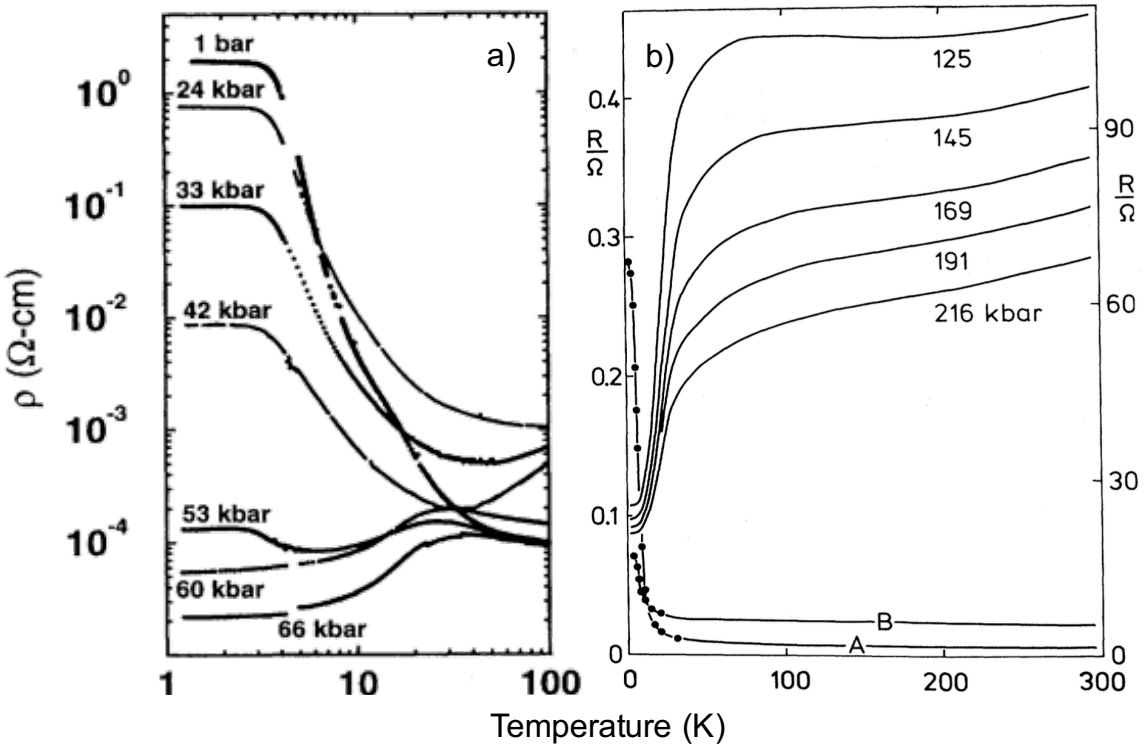

Figure 20 a) electrical resistivity of SmB_6 as a function of temperature [136] and b) electrical resistivity of SmB_6 as a function of temperature for various pressures between 125 and 216 kbar (left scale) and 21 kbar (right scale, curves A&B) (reprinted with permission) [135].

The MB_6 structure also offers a number of superconducting characteristics such as a high density of scattering centers and nine branches of low-frequency phonon modes [8], and while four compounds have been shown to exhibit superconductivity (Table 3), only YB_6 and LaB_6 have been repeatedly demonstrated.

The superconducting transformation of LaB_6 eluded researchers [140, 141] for years as the extremely low temperature was difficult to achieve in experiments. Superconducting transformations have been reported for NdB_6 (3 K) and ThB_6 (0.74 K) [118, 142], but may only be sharp drops in resistivity below the Néel point [143].

Table 3 Superconducting hexaborides listed with lattice parameter and superconducting temperature, T_C – i [142], ii [144].

MB_6	A_0 (Å)	T_C (K)	Ref.
YB_6	4.1000	7.1	i
LaB_6	4.1569	0.44	ii

Although the thermoelectric (TE) potential of a given material depends on both electrical and thermal properties, the bulk of TE-based hexaboride studies have focused primarily on the electrical aspect as it remains the unruliest and most challenging component of the system. Boron-rich compounds have long been investigated as candidates for thermoelectric applications, and alkaline-earth hexaborides have shown promise as possible n-type equivalents with good Seebeck coefficients (Figure 21) [5, 31, 127]. Unfortunately, as described above, the electrical properties of some of these compounds are inconsistent, as even the divalent compounds are sometimes too electrically conductive.

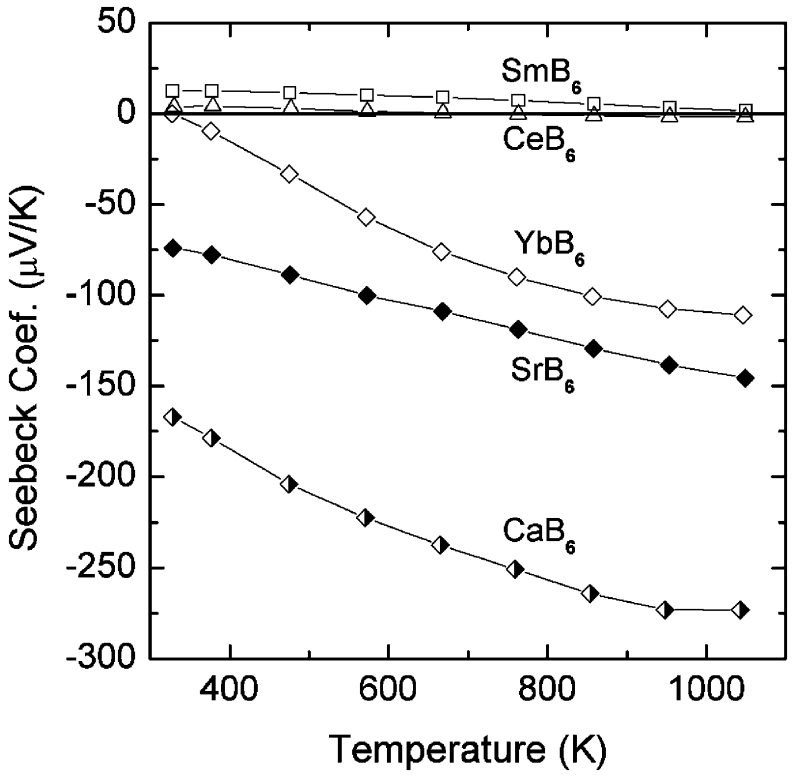

Figure 21 Seebeck coefficient as a function of temperature for some hexaborides (reprinted with permission) [5].

However, this has not slowed the investigation of hexaboride thermoelectric applications, especially for Takeda and coworkers who have performed extensive studies on the subject focusing primarily on the divalent candidates SrB_6, CaB_6 and BaB_6 and their alloys [5, 31, 45, 127].

1.1.3.3. Magnetic Behavior

Magnetism in hexaborides is an intriguing phenomenon with ever increasing complexity, and recent research has been aimed at determining the cause of these properties in hexaboride compounds. The first case is of EuB_6; a compound in which the magnetic ordering has been attributed to the ferromagnetic alignment of localized Eu 4f electron moments [145, 146]. According to recent neutron-scattering experiments [147],

the zero-temperature moment is 7 Bohr magnetons per Eu ion, as expected for the divalent configuration of Eu previously shown by photoemission and Mössbauer measurements [79, 131]. Specific heat and magnetization measurements reveal that this state is reached via two distinct transitions, with the first representing the Curie Temperature at T_C = 12.6 K and the second representing a charge delocalization transition caused by the overlap of magnetic polarons and resulting in colossal magnetoresistance (CMR) at T_M = 15.5 K [79]. Additionally, a magnetic phase separation is observed between 30 and 40 K and is likely accompanied by the self-localization of free charge carriers and the formation of magnetic polarons of two types [148].

The second magnetic phenomenon is that of La-doped CaB_6. In 1999, Young et al. reported that electron-doped CaB_6 was ferromagnetically polarized with a saturation moment of 0.07 μ_B per electron [149]. By studying the temperature dependence of the magnetic moment in a field of 0.1 T, they found that CaB_6 doped with as little as 5% La ($Ca_{0.995}La_{0.005}B_6$) had a Curie temperature (T_C) of 600 K [149]. Research over the next few years attributed this strange behavior to the overlapping band gaps in divalent hexaborides that cause a shift from semiconductor to semi-metallic [124, 125, 129, 149]. In 2002, both Matsubayashi et al. and Mori and Otani published results claiming that the source of ferromagnetism in these divalent hexaborides was due to iron impurities [82, 83] Figure 22 from Matsubayashi et al. depicts a correlation between reduction in magnetization and decreasing iron mass.

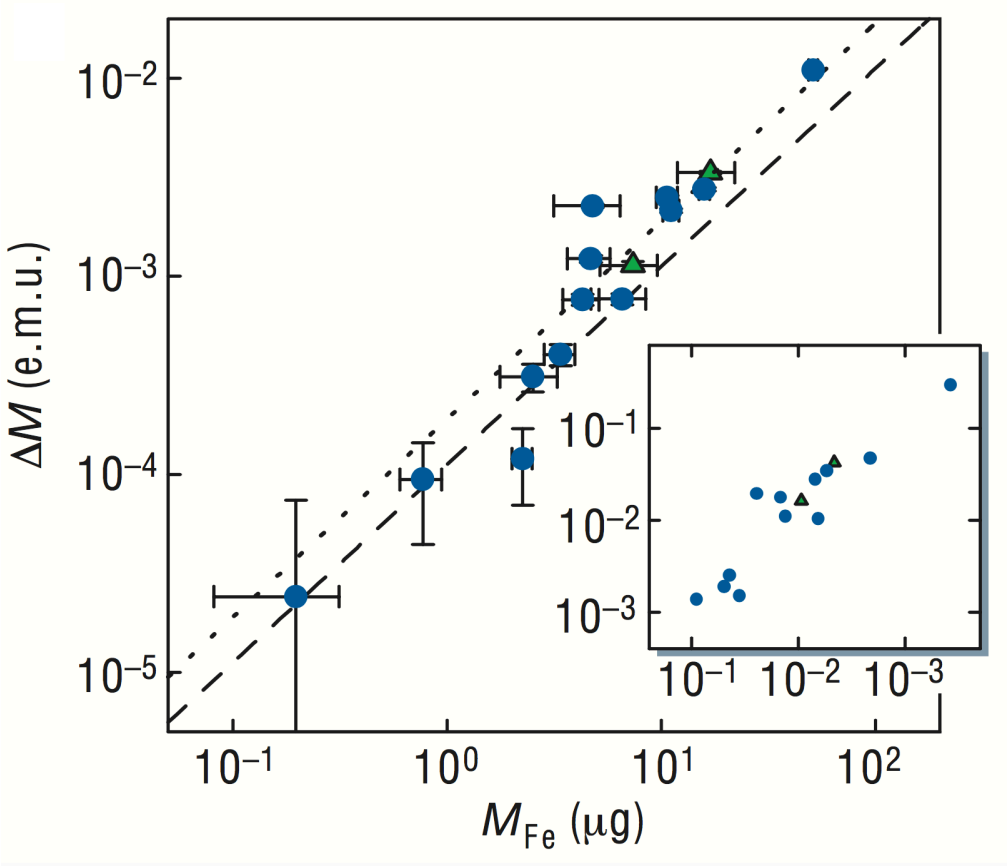

Figure 22 Correlation between magnetization reduction, ΔM, and iron mass, m_{Fe}. The data is consistent with the curves indicating the saturation magnetization of FeB (dashed line) and Fe_2B (dotted line). Inset, plot of $\Delta M/m_s$ in e.m.u. per gram (m_s, = sample mass) against m_{Fe}/m_s in $\mu g g^{-1}$ (reprinted with permission) [82].

Figure 23 from Mori and Otani shows the complete transition from ferromagnetic to diamagnetic after washing La-doped CaB_6 in HCl to remove iron impurities. The source of iron impurities in these samples comes from the synthesis via aluminum flux, where the increased electrical conductivity of La-doped CaB_6 can result in electrochemically plated iron onto the surface during HCl removal of the flux [83].

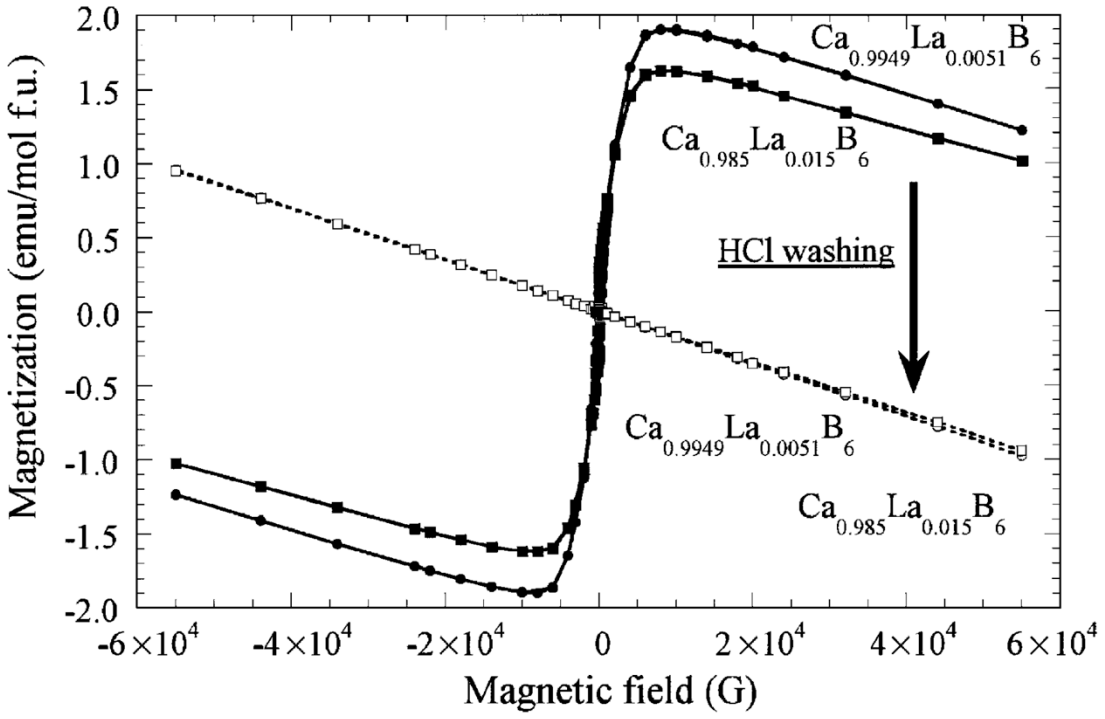

Figure 23 Magnetic field dependence of the magnetization of $Ca_{0.9949}La_{0.0051}B6$ (closed circles) and $Ca_{0.985}La_{0.015}B_6$ (closed squares) at 300 K, and the magnetization of HCl washed $Ca_{0.9949}La_{0.0051}B_6$ (open circles) and $Ca_{0.985}La_{0.015}B_6$ (open squares). Reprinted with permission [83].

1.1.3.4. Mechanical Properties

Although there are various borides that display ultra-hardness [114, 115], hexaborides have never truly been sought after for their mechanical properties. Nevertheless, there are reports documenting the elastic modulus *(E)* [87, 150], flexural strength *(σ)* [151], and hardness *(H)* [59, 70, 71, 150, 151] of various hexaboride compounds. Otani et al. grew single crystals of LaB_6, CeB_6, PrB_6, NdB_6, and SmB_6 by the floating-zone method and used microhardness measurements to gauge the quality of the crystal [59]. Results from their measurements can been seen in Table 4.

Table 4 Growth temperature and Vicker's hardness values for hexaborides grown by the floating zone method (adapted from Otani et al.) [59].

	Growth Temp		Hardness (kg/mm^2)			
	K	ΔT	ΔH^a (%)	at 1173 K	ΔH^b (%)	Increase in hardness at growth temperature (%)
LaB_6	2988	0		1160		
LaB_6 (boundary-free)	2788	-200	+ 28	1160	0	+ 28
CeB_6	2848	-140	+ 19	1090	-6	+ 13
PrB_6	2778	-210	+ 30	1080	-7	+ 23
NdB_6	2738	-250	+ 37	1010	-13	+ 24
SmB_6	2618	-370	+ 60	940	-19	+ 41

Dub et al. used nanoindentation to study the elasto-plastic transition in LaB_6 single crystals. They observed an abrupt elasto-plastic transition at shear stresses close to the theoretical values for LaB_6 due to homogeneous nucleation of dislocations in the contact region [150]. Figure 24 depicts load displacement curves detailing the difference between 1) spalling along the cleavage plane and 2) a sample with high dislocation density induced by mechanical polishing.

In addition to experimental work, some researchers have taken a theoretical approach for studying the mechanical properties of hexaborides [14, 21, 152-155]. Sandeep et al. used density functional theory (DFT) to compare the bulk modulus of LaB_6, CeB_6, PrB_6, and SmB_6 to results from both other theoretical work (generalized gradient approximation, GGA and local spin density approximation, LSDA) and experimental work [152-155]. Their results and corresponding comparisons can be seen in Table 5.

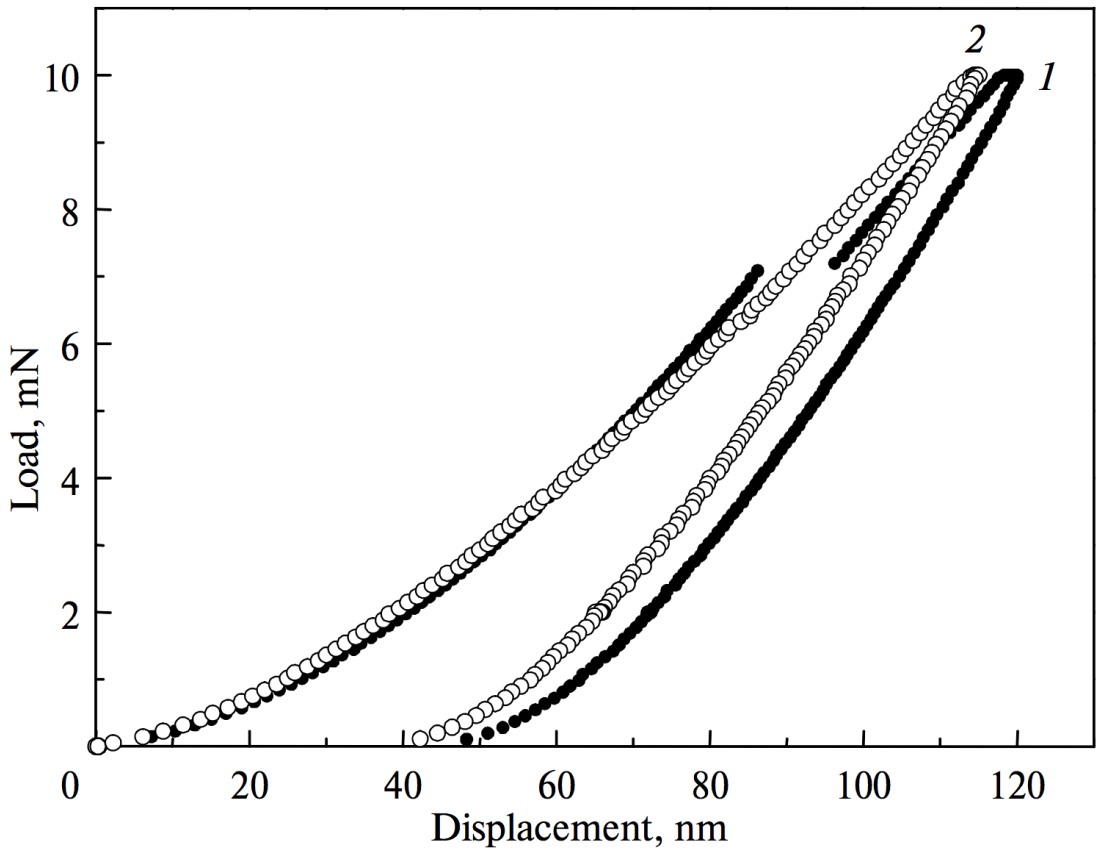

Figure 24 Effect of the mechanical polishing of the LaB_6 single crystal with a diamond powder on the load–displacement curve where 1: spalling along the cleavage plane and 2: mechanical polishing (reprinted with permission) [150].

Table 5 Bulk modulus values for LaB_6, CeB_6, PrB_6, and SmB_6 from DFT, LDA and GGA experiments (adapted from Sandeep et al.) [155].

	Bulk Modulus (DFT)	**Bulk Modulus (LDA)**	**Bulk Modulus (GGA)**	**Bulk Modulus (experimental)**
	GPa	GPa	GPa	GPa
LaB_6	189.5	178.8	166.2	164
LaB_6				173
CeB_6	162.2	173		166
PrB_6	165.8			
SmB_6	146.7	179.6	167.2	

1.2. Combustion Synthesis

Traditional production of high-temperature refractory materials often involves elevated synthesis temperatures and long processing times. One major way to save time and energy (and therefore cost) is through the use of quick and low-temperature synthesis methods. Combustion synthesis (CS), also referred to as self-propagating high-temperature synthesis (SHS), can be described as the formation of condensed substances by combustion of condensed precursors [156]. The ignition of condensed precursors produces an exothermic chemical reaction with sufficient energy that it becomes self-sustaining [156, 157]. Combustion synthesis has been used to produce a variety of materials, including oxides, carbides, borides, nitrides and intermetallics [158]. Table 6 contains a list of some non-oxide compounds produced by SHS and their combustion temperatures [159]. In addition to the cost saving aspects of combustion synthesis its ability to produce unique or sub-micron structures makes it attractive for nanomaterials processing.

Combustion processes can be divided into two general forms [159-161]: i) *propagation* or *wave* reactions, where a local ignition is followed by a reaction that moves through the compact as a synthesis wave and ii) *bulk* reactions, where the precursors are heated together (often in a furnace) until the energy is sufficient enough to ignite the synthesis reaction simultaneously throughout the material. A classic example of wave propagation SHS can be seen in the synthesis of TiB from solid Ti and B precursors (Figure 25) by A.G. Merzhanov, who developed solid-flame combustion in 1967 [156, 162].

Table 6 Some non-oxide materials produced by SHS and their combustion temperatures in Kelvin (adapted from McCauley) [159].

Borides	TiB_2 (3190), ZrB_2 (3310), NbB_2 (2400), TaB_2 (3370), MoB_2 (1800), LaB_6 (2800), HfB_2, CrB, VB
Carbides	TiC (3210), HfC (3900), B_4C (1000), Al_4C_3 (1200), TaC (2700), SiC (1800), WC (1000), ZrC (3400), NbC (2800), Cr_3C_2
Carbonitrides	TiC-TN, NbC-NbN, TaC-TaN
Nitrides	TiN (4900), ZrN (4900), BN (3700), AlN (2900), Si_3N_4 (4300), TaN (3360), HfN (5100), NbN
Silicides	$MoSi_2$ (1900), Ti_5Si_3 (2900), Zr_5Si_3 (2800), Nb_5Si_3 (3340), $NbSi_2$ (1900), $TaSi_2$ (1800), $ZrSi_2$, WSi_2 (1500), V_5Si_3 (2260)
Hyrdrides	TiH_2, ZrH_2, NbH_2
Intermetallics	NiAl, FeAl, N_6Ge, TiNi, CoTi, CuAl
Chalcogendies	MoS_2, $TaSe_2$, NbS_2, WSe_2

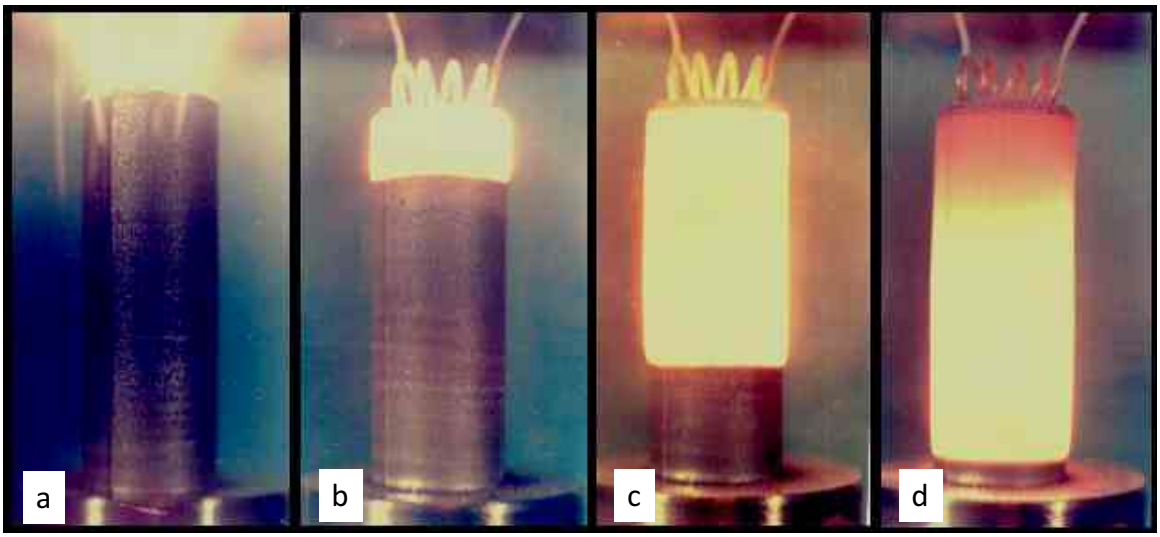

Figure 25 TiB produced by SHS from solid precursors by A.G. Merzhanov. Frames of an SHS process where a) is initiation (t = 0), b) and c) are propagation of the combustion front (t = 0.1 s and 2.7 s, respectively) and d) is cooling (t = 4 s).

The theory of SHS was advanced with the concept of non-equilibrium reactions in which the reaction zone is broader than that of the fore-flame zone due to combustion self-inhibition [156, 163, 164]. The wave velocity of the reaction (U) is then described by:

$$U^2 = A\frac{T_*^2}{\eta_*}exp\left(-\frac{E_a}{RT_*}\right)$$

Equation 4

where T_* is the temperature determining the reaction rate, A is a value determined by reaction rate and heat transfer constants, η_* is the degree of conversion ($\eta_* <1$) and E_a is the activation energy.

Unlike wave reactions, which involve ignition by an external source (heated coil, laser, microwave), bulk reactions are ignited by increasing the ambient temperature of the precursors. These precursors can be in either solid form (usually as powders) or dissolved into a solution. The most common form of solution combustion synthesis

(SCS) is the dissolution of metal nitrates and organic fuels in water [161]. Although it could be argued that because the water must evaporate before combustion can occur this process is no different than traditional CS, the important distinction lies in the mixing of the precursors. Dry combustion synthesis precursors are often milled or mixed by hand before being pressed into pellets. The homogeneity of mixing is dependent on the mixing mechanism, time, and the particle size of the precursors. In SCS, the ability to form a precursor solution allows for a higher degree of homogeneity as long as all of the precursors are soluble in the solute. Once the liquid has evaporated the precursors can be heated past the boiling point until combustion occurs, much like a dry combustion synthesis. The intensity of the reaction depends on several factors but is highly affected by fuel-to-oxidizer ratio (f/o).

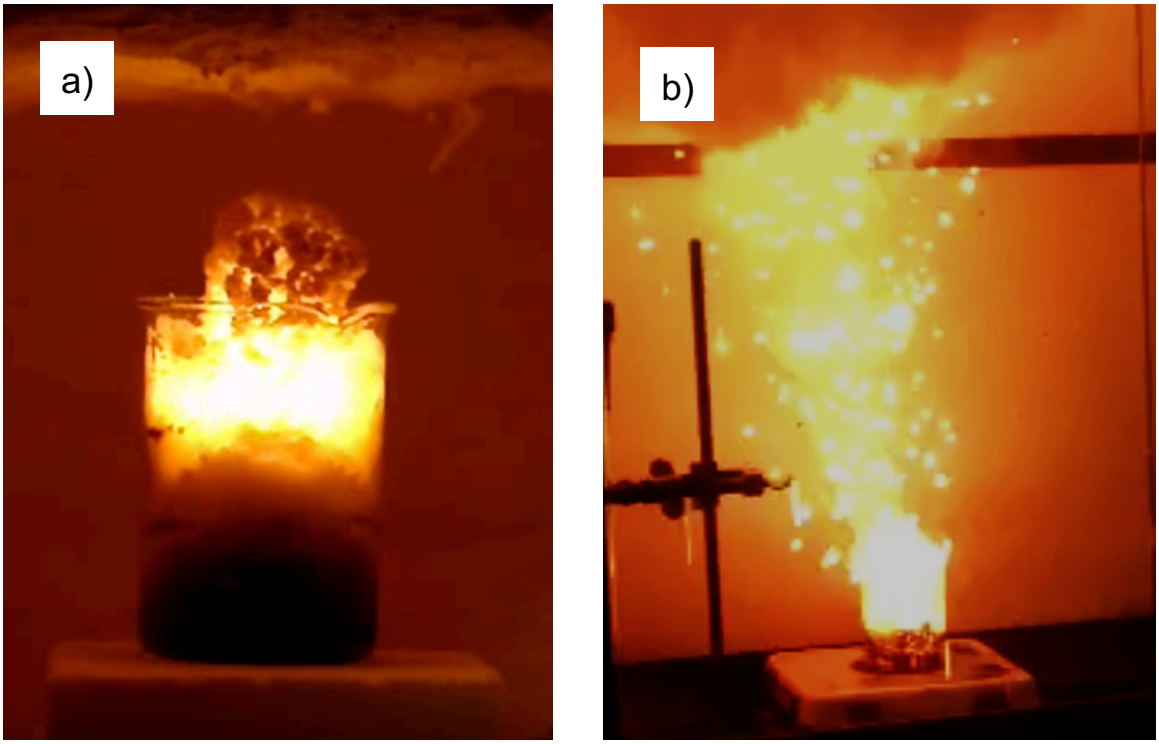

Figure 26 Combustion synthesis of a) a slow, smoldering oxide reaction [165] and b) an aggressive, explosive boride reaction.

Figure 26 depicts two different types of reactions where a) is slow and smoldering and b) is quick and violent. Increasing the f/o could easily turn a smoldering reaction into an intense reaction. While there are countless examples in published literature of the various combustion processes, the following are a few examples of solution combustion (SCS) as it is the method of choice for the work in this dissertation.

I. The synthesis of γ-ferrite by Ravindranathan and Patil (1986) using a one-step SCS process involving thermal decomposition of either $N_2H_5Fe(N_2H_3COO)_3 \cdot H_2O$ or $Fe(N_2H_3COO)_2(N_2H_4)_2$ resulting in powders with specific surface areas of 75 and 28 m^2/g, respectively [166].

II. The research by Chick et al. (1990) is among the earliest involving SCS using nitrates and glycine. Chromite and manganite were produced in this fashion at an ignition temperature of 453 K resulting in powders with specific surface areas of 32 and 23 m^2/g for chromite and manganite, respectively [167].

III. Shea et al. (1996) produced Cr-doped yttrium aluminum garnet (YAG) and Eu-doped yttira using metal nitrates and a combination of urea, glycine and carbohydrazide at 773 K. They found that the particle size, luminescence and crystallinity of the powders were effected by fuel type, f/o and ignition temperature [168].

IV. McKittrick et al. (1999) produced luminescent rare-earth activated oxide powders via SCS and studied the effect of various fuels on particle size. They reported a relationship between increasing gas production (from fuel) corresponded to decreasing particle size of the resultant powder product [169].

V. Mimani and Patil (2001) produced alumina, ceria, yttria zirconia and their composites via SCS using metal nitrates, ammonium nitrate and glycine. The reactions were smoldering and resulted in voluminous powders with large specific surface areas (10-30 m^2/g) and small particle sizes (10-50 nm) [170].

VI. Pathak et al. (2002) studied the effect of pH on SCS of alumina and reported flaky particles at a pH of 2 and fine, desegregated particles at a pH of 10. They concluded that the slow decomposition rate at low pH was responsible for the flaky morphology, opposite that of the faster decomposition at higher pH values [171].

VII. Aruna and Rajam (2004) produced alumina-zirconia nanocomposites via SCS using metal nitrates and urea and obtained particle sizes of ~37 nm. By changing the to a mixture of fuels including urea, glycine and ammonium acetate they were able to reduce the particle size to <10 nm [172].

VIII. Dinka and Mukasyan produced iron oxide via SCS using ferric nitrate and glycine on a multitude of porous supports including alumina and zirconia. Use of the highly-porous supports led to oxides with specific surface areas >200 m^2/g [173].

IX. Bansal and Zhong (2006) produced $Sm_{0.5}Sr_{0.5}CoO_{3-x}$ and $La_{0.6}Sr_{0.4}CoO_{3-x}$ nanopowders via SCS using metal nitrates and glycine between 573 and 673 K. Average particle size for the powders was ~12 nm [174].

X. Mukasyan, Epstein and Dinka (2007) used iron oxide as a model to study various types of SCS: volume combustion, self-propagating combustion and impregnation combustion. They found that controlling the combustion parameters influences

the microstructural characteristics and hypothesized that these trends would work for other complex oxide systems [175].

XI. Prakash et al. (2010) produced nanocrystalline $Li_4Ti_5O_{12}$ (LTO) by SCS using metal nitrates and glycine resulting in highly porous flaky particles with a specific surface area of 12 m^2/g. The reaction was smoldering an voluminous and resulted in particles 20 to 50 nm in size [176].

XII. Reddy et al. (2011) produced Cu-doped (0.1 mol%) ZrO nanopowders via SCS at 573 K using metal nitrates and oxalyl dihydrazide as a fuel. The particles were highly porous and approximately 40 nm in size, completely exhibiting the hexagonal wurtzite structure of ZnO [177].

XIII. The most pertinent research to this dissertation topic is the work done by Kanakala et al. (2010-2011) on the synthesis of metal hexaborides via combustion synthesis. Combustion of LaB_6, SmB_6 and EuB_6 with metal nitrates, boron and carbohydrazide was the first example of using SCS to produce a non-oxide material. Hexaboride particles were cubic and approximately 500 nm in size. Although the SCS method results in some degree of precursor oxidation (oxides and borates) the unwanted phases are easily washed away using concentrated HCl [110, 111].

1.3. Spark Plasma Sintering

Sintering is the process of thermally bonding particles in contact with one another without liquidation, and is a vitally important step in the creation of densified ceramics. The high melting temperatures of refractory ceramics can make the mass transport required to accomplish sintering difficult to achieve, and a great deal of current research is aimed at enhancing the sintering process of these materials. This enhancement can be thought of as a reduction in either time, cost and energy or the simple act of obtaining a sintered specimen. In the realm of sintered ceramics, the addition of current to assist in sintering is a relatively new technology, with the early work done by Lenel at Rochester Polytechnic Institute in the 1950's referred to as "spark sintering" [178]. Since then quite a few names have surfaced for advanced techniques such as "electric pulse assisted consolidation" (EPAC) [179], "plasma assisted sintering" (PAS) [180], "spark plasma sintering" (SPS) [181] and "pulsed electric current sintering" (PECS) [182]. Although the word "plasma" is often used to describe this sintering method, evidence for the existence of plasma in this process has yet to be presented [183]. Nevertheless, the term spark plasma sintering (SPS) has gained popularity and will be used throughout this dissertation to describe the current-assisted sintering method utilized by the author.

A modern SPS unit is comprised of two electrodes that also function as pressing rams which are capable of applying both a load and electric current to the sample. As the large current (kA's) passes through the sample and the die it increases in temperature due to Joule heating – making it important to note that the two parameters of current and temperature and not independent. A schematic of an SPS unit can be seen in Figure 27.

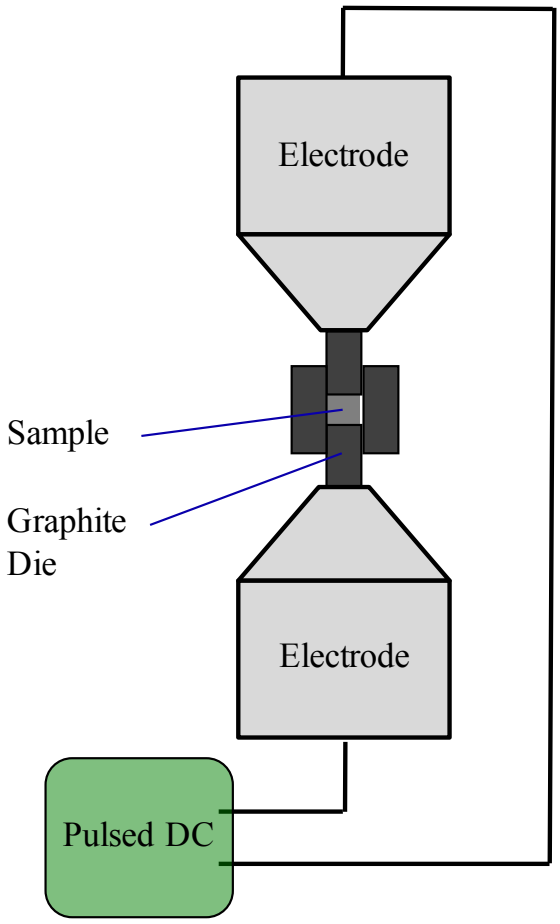

Figure 27 Schematic of an SPS unit containing two electrodes (positive and negative) between which a pulsed DC current passes through the die (often graphite) and sample.

Joule heating does, however, have the advantage of high heating rates that can drastically shorten the sintering time and therefore reduce the effects of surface diffusion and subsequent grain coarsening [184, 185]. Because electric current will flow through the path of least resistance, the electrical conductivity of the materials between the electrodes greatly influences the components participating in Joule heating. In a series of investigations on the SPS process, Anselmi-Tamburini et al. modeled the current and temperature distributions of under typical conditions using two materials with drastically different electrical conductivities; alumina and copper. They found significant

differences in the current and temperature distributions between the two cases, resulting in different Joule heating flux distributions [186]. Figure 28 depicts the difference in current distribution between graphite dies containing either alumina or copper.

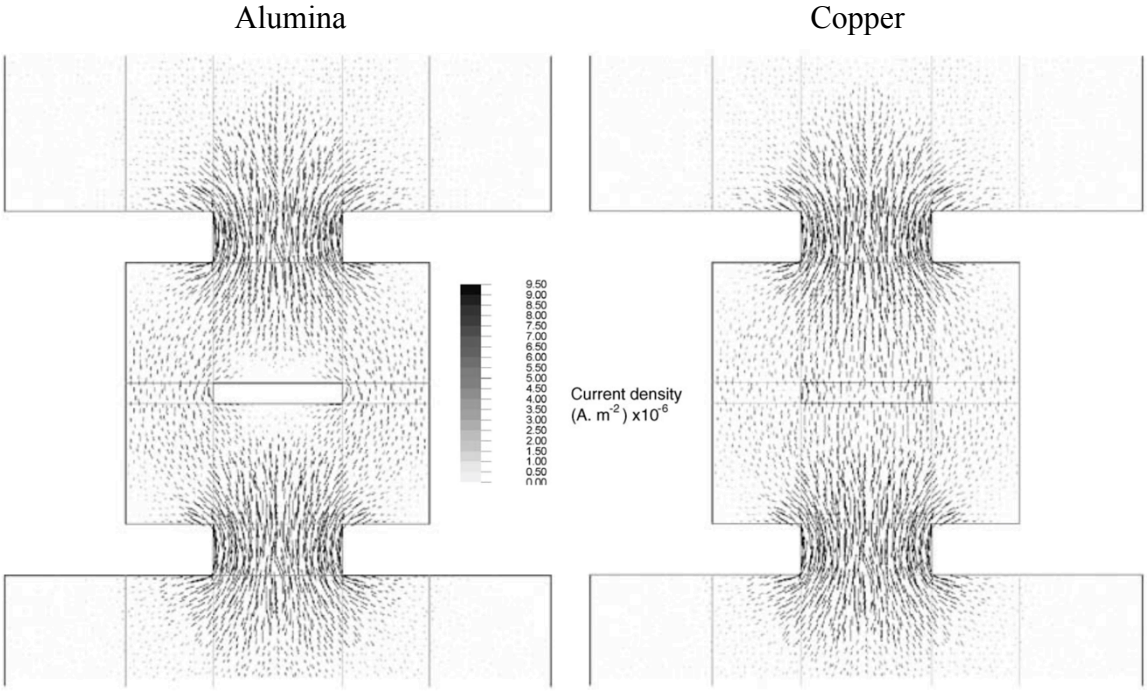

Figure 28 Current distributions in the SPS die for alumina and copper samples. Applied voltage = 5 V (reprinted with permission) [186].

The difference in current density is clear and it is quite apparent that the current flow through the copper sample (conductive) is greater than that through the alumina sample (insulating). This can also be represented graphically to better understand the current densities in the sample versus the current densities in the graphite die. Figure 29 shows the current distribution as a function of location within the sample and die components [186].

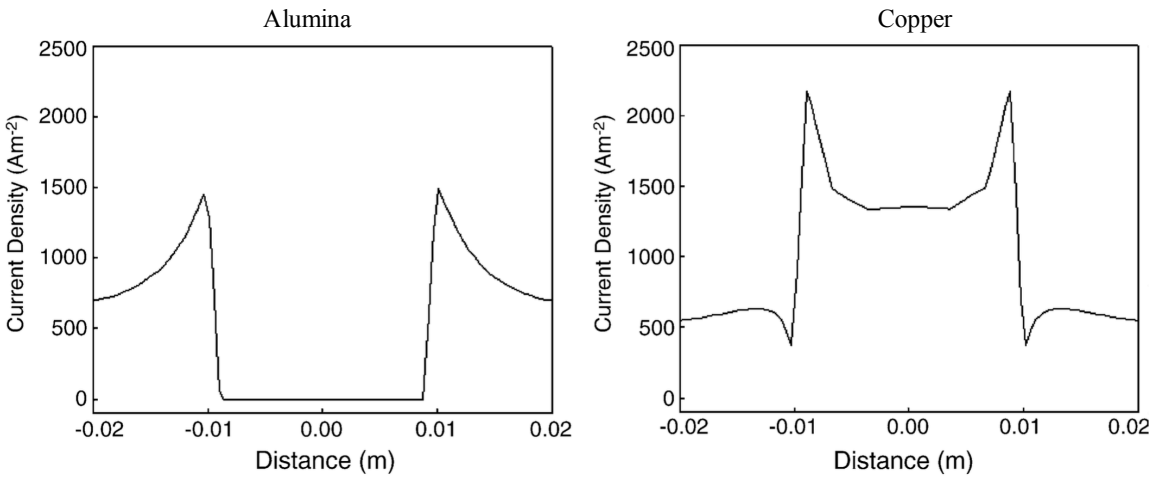

Figure 29 Radial current density distribution for a non-conducting (alumina) and conducting (copper) samples. The profile is calculated along the diameter passing through the center of the sample. Applied voltage = 5 V (reprinted with permission) [186].

Here it is interesting to note that the highest current density for the alumina sample is at the inside of the die wall closest to the specimen, while the highest current density for the copper sample is at the surface of the specimen and decreases rapidly into the graphite die. While almost no current is carried by the sample in the alumina setup, the majority passes through the samples in the copper setup. Also of note is that these calculations do not consider the powder nature of real-life SPS samples as their corresponding decreased conductivity, which could be orders of magnitude lower than the densified material [186]. While there are an ever-increasing number of publications detailing the use of current-assisted sintering for the production of densified materials, the following are a few examples highlighting the capabilities of SPS:

I. Nishimura et al. (1995) used SPS to sinter β-SiN at temperatures 100 – 150 K lower that with traditional hot-pressing, allowing them to achieve grain sizes of

200 – 300 nm. The use of sintering additives (5 wt% Y_2O_3 and 2 wt % MgO) allowed them to achieve > 98% relative density [187].

II. Shen et al. (2002) reported a systematic study on the effect of changing the parameters of temperature, holding time, heating rate, pressure, and pulse sequence on the spark plasma sintering of Alumina. They found that the SPS process enabled sintering of alumina at lower temperatures than conventional methods (1423 K) though enhanced densification and grain growth [188].

III. Cha and Hong (2003) sintered binderless WC to 98% relative density using SPS and a sintering temperature of 1923 K. As with many refractory carbides, WC is difficult to sinter without a binder such as Co or Ni. They found that shortened sintering times due to the fast heating rates possible with SPS helped suppress grain growth and decarburization [189].

IV. Angerer et al. (2005) sintered TiC_xN_{1-x} at temperatures between 1873 and 2073 K using SPS to achieve ~ 95% relative density and a grain size of ~ 200 nm. They found that SPS was capable of producing dense samples with grains three times smaller than samples produced by gas-pressure sintering (GPS) [190].

V. Li et al. (2005) sintered lead-free $Na_{0.5}K_{0.5}NaO_3$ using SPS at temperatures as low as 1193 K an managed to achieve 99% relative density. Niobates are traditionally tricky to sinter yet the used of SPS was able to produce high density and grains between 200 – 500 nm [191].

VI. Kim et al. (2007) sintered transparent alumina using SPS and a slow heating rate of 8 K/min to 1423 K. While SPS is often used to induce fast heating rates, it is also capable of slow and controlled temperature ramps. The transparent alumina

had a grain size of 270 nm, a residual porosity of 0.03% and an in-line transmission of 47% for a wavelength of 640 nm [192].

VII. Sciti et al. (2008) sintered ZrC using SPS and $MoSi_2$ as a sintering aid at temperatures between 2023 and 2373 K, noting that increasing the volume fraction of $MoSi_2$ (up to 9%) decreased the sintering temperature. The Joule heating effects present in SPS are capable of generating the very high temperatures necessary to sinter refractory carbides [193].

VIII. Guo et al. (2008) used SPS to sinter ZrB_2 at temperatures between 2073 and 2223 K using a heating rate of 200 – 300 K/min. The found that grain growth was significantly greater at temperatures above 2173 K and heating rates below 200 K/min. While they were able to obtain fine and homogeneous grains at heating rates >200 K/min, too high of a heating rate resulted in a decrease in final density of the specimens [194].

IX. Couret et al. (2008) spark plasma sintered pre-alloyed TiAl powders also containing parts Cr, Nb and B at temperatures between 1373 and 1523 K with the entire process taking less than 30 minutes. The authors were able to achieve two-phased ($\gamma + \alpha_2$), duplex and lamellar microstructures depending on the powder and the sintering temperature [195].

X. Kelly and Graeve (2015) completed a detailed study on the mechanisms of pore formation in spark plasma sintered TaC. They found there were three main pore-forming mechanisms: i) evolution of oxygen impurities, ii) evolution of excess carbon and iii) incongruent sublimation of TaC [196].

1.4. Research Motivation

With the continually growing global population and volume of mechanized transportation there is an ever increasing push to move forward from fossil fuels and seek out forms of renewable energy. Unfortunately, there is no single answer to the problem and we instead find ourselves addressing the tiny details before moving on to make global change. For example, it would be wonderful if we lived in a sustainable hydrogen economy where the only by-product from transportation was water vapor – but where does the hydrogen come from? Although it is the most abundant element in the universe, it is not the easiest to separate from oxygen here on earth. After the challenge of production is solved, where do you store hydrogen? The smallest and simplest element is a masterful escape artist and will gradually diffuse through the walls meant to contain it. While pressurized tanks are still the most common form of hydrogen storage, there are new technologies on the horizon that offer alternatives. One such alternative is solid-state storage, where the hydrogen atoms are kept neatly inside the atomic structure of a host material. Solid-state storage relieves the need for the high pressures (20 MPa) or low temperatures (20 K) used in tank storage, and because the gas has actually been integrated into the crystal structure of the host material it poses no fire risk. Despite all the potential advantages of solid-state hydrogen storage, there are still some challenges to be met.

Today's most common use for hydrogen in the realm of energy is the fuel cell, which converts hydrogen gas into electricity and water. Already there are hydrogen cars, busses and trucks on the street powered by fuel cells that draw hydrogen from pressurized tanks (2017 Toyota Mirai pictured in Figure 30).

Figure 30 The 2017 hydrogen-powered Toyota Mirai with an EPA-estimated 67 city / 67 highway MPG and a 312-mile driving range. Estimated refueling time is 5 minutes [197].

There are three main requirements for the hydrogen storage system: it must be able to deliver hydrogen quickly to the fuel cell (discharge), it must be able to refill in a reasonable amount of time (charge), and it must be safe. Although tanks already meet all three requirements, there is always the need for improvement and innovation. One of the main challenges with solid-state storage is rapid charging and discharging. On top of this, the material needs to be able to cycle through many charge/discharges (think filling your gas tank) without a decrease in performance.

The unique crystal structure and bonding of hexaboride compounds make them a research candidate for solid state hydrogen storage. The mobility of the metal atom within the rigid boron sublattice presents an opportunity to use these materials as hosts for the storage of atoms or ions if transport can be reversibly controlled with an electric

field. If the diffusion of the metal atoms can be directionally controlled to move forward and backward, it could create a space in the lattice for guest atoms to diffusion into and then push them back out by reversing the field. Figure 31 contains a schematic depicting this concept for the CaB_6–type crystal structure.

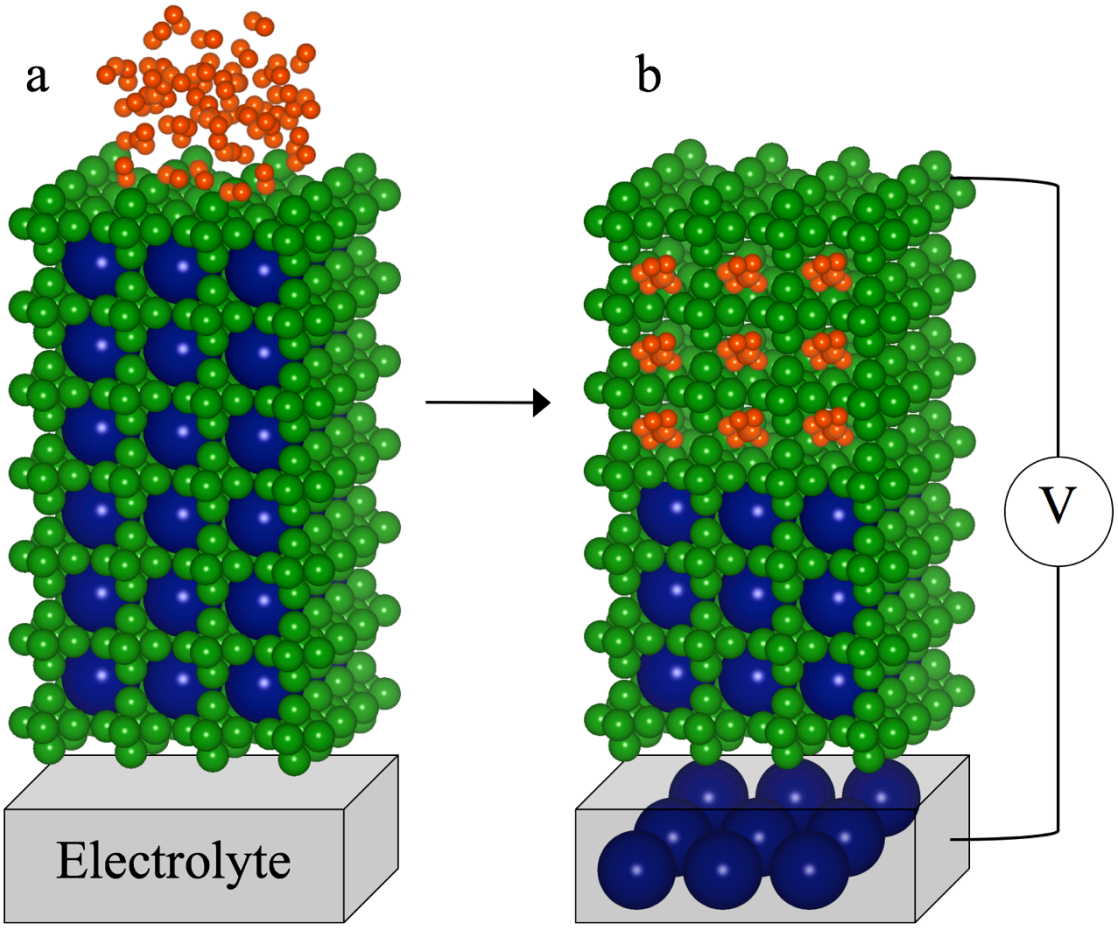

Figure 31 Schematic depicting the concept of storing guest atoms or ions in the lattice of an MB_6 structure, where a) represents the complete MB_6 structure with metal atoms (blue) filling all sites within boron (green) sublattice and b) represents an applied field moving metal atoms out of sites to make room for guest atoms or ions (red).

Chapter 1, in part, is being prepared for publication authored by J.T. Cahill and O.A. Graeve. The dissertation author was the primary investigator and author of this paper.

2. Experimental Procedure

2.1. Combustion Synthesis

The beginning stages of this research on the combustion of alkaline-earth hexaborides were based loosely on the work of Kanakala et al., who pioneered the synthesis of hexaborides via combustion of several trivalent MB_6 compounds [110, 111]. Early on it became clear that the decreased electronegativity of the alkaline-earth metals led to an increase in the potential for oxidation and therefore an increase in the intensity of the reactions. If one prepares a combustion based on the balanced chemical reaction between the precursors (Equation 5), the intensity of the ensuing reaction reaches unsafe levels and embodies the term *combustion*.

$$2M(NO_3)_2 + 12B + 3CH_6N_4O_2 \rightarrow 2MB_6 + 3O_2 + 8N_2 + 9H_2O \qquad \text{Equation 5}$$

Kanakala et al. arrived at this realization as well, and made the appropriate adjustment in the form of a reduced fuel-to-oxidizer ratio (f/o). Equation 5 shows that for every 2 mols of metal nitrate it takes 3 mols of carbohydrazide to balance the reaction, resulting in an f/o of 1.5 (in the case of boride combustions, elemental boron is not considered an oxidizer due to its higher electronegativity). For the combustions of LaB_6 and SmB_6, Kanakala et al. reduced the f/o to 15% of the stoichiometric value. Combustions of alkaline-earth hexaborides required the f/o to be reduced to as little as 5%, as detailed in Figure 32 below. F/o values for the alkaline-earth hexaborides were determined by trial and error, with the powder yield, purity and reproducibility determining the success of a combustion. These factors were highlighted at the extremes by powder purity – a low intensity combustion fails to react all of the elemental boron while a high intensity reaction produces a larger percentage of oxides. In combination

with a decreased f/o, the second major deviation from Kanakala et al. was mixing the precursors in water as opposed to dry.

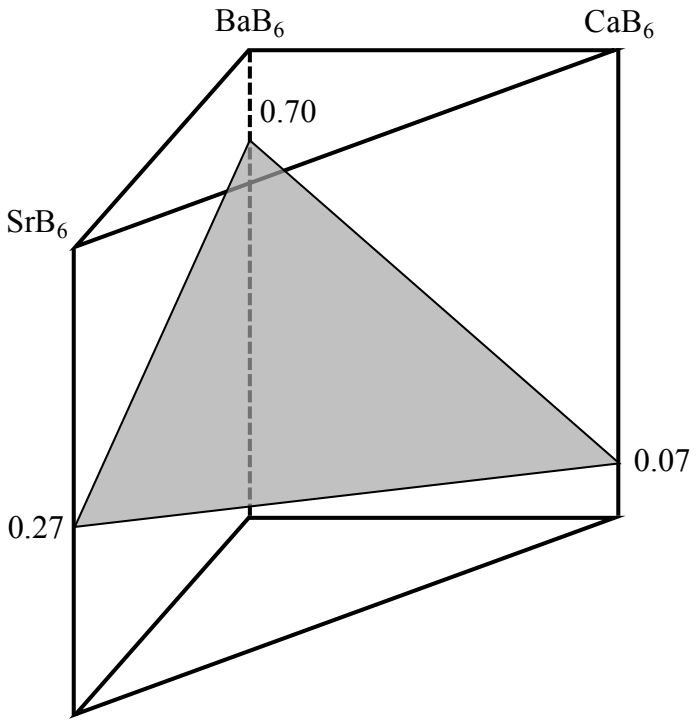

Figure 32 Fuel to oxidizer ratios (f/o) for SrB_6, BaB_6 and CaB_6. Grey triangle represents theoretical f/o's for all mixed-cation compositions.

Although metal nitrates and carbohydrazide are soluble in water, boron is not. Nevertheless, agitation by stirring leads to a dispersed suspension of the boride particles within the water-nitrate-fuel solution, and the turbulence caused by boiling continues that process once the stir bar is removed. This is done with the goal of obtaining the highest degree of homogeneity possible, at the cost of time. A complete procedure for a standard alkaline-earth combustion is depicted by the flowchart in Figure 33.

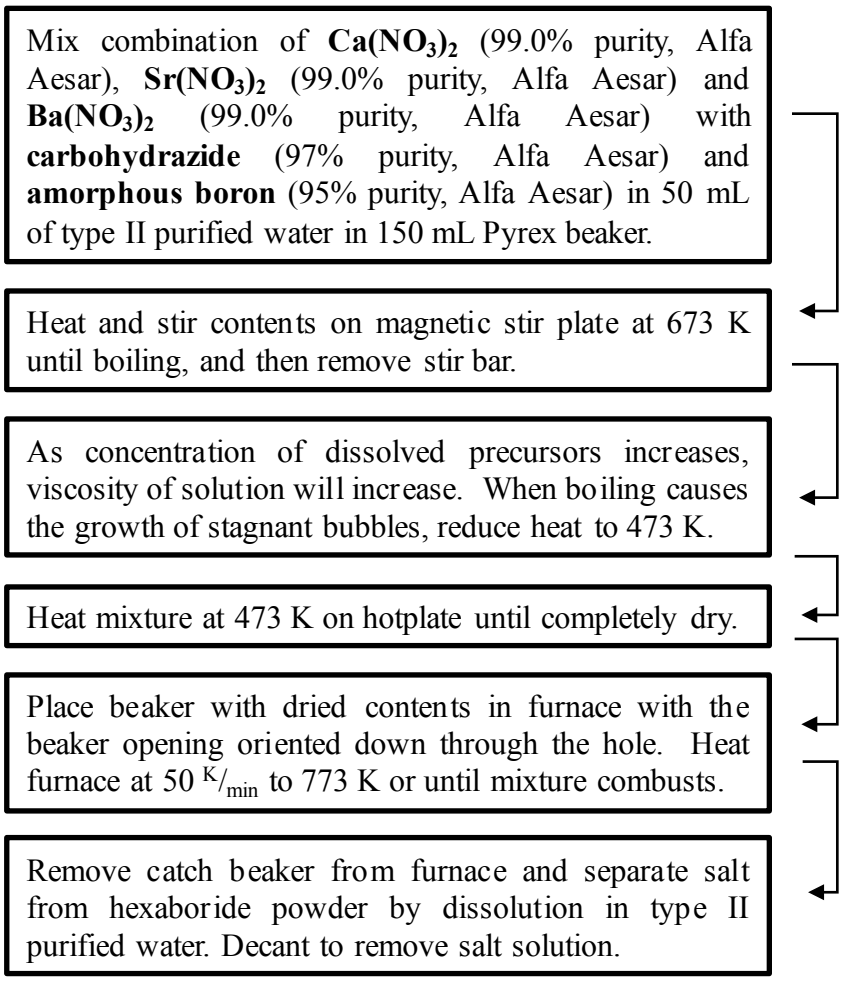

Figure 33 Flow chart procedure for alkaline-earth hexaboride combustion.

The preliminary combustions following the above procedure were ignited in a box furnace with an 0.25 m^3 interior chamber heated to 773 K at approximately 50 K/min. As previously stated, one of the benefits to combustion synthesis is that a multitude of heat sources are adequate for ignition and there is no need for an inert atmosphere. At the same time, the exposed nature of this process presents potential risk to the operator in the form of ultra-fine airborne particulates expelled along with the combustion gases. Hexaboride reactions are no exception to this and the increased intensity compared to oxide combustions produces a substantial amount of these airborne particulates. Once

this became apparent, a custom furnace was designed to protect the operator from particulate inhalation (determined by XRD to contain primarily metal borates). This custom furnace, built by hand in the lab, consisted of a cylindrical heating element encased in a stainless steel box suspended by aluminum angle within a sealed chamber built from fire-retardant fiberglass panels. Figure 34 depicts a design schematic and a picture of the final product. To remove any suspended particulates, a series of water traps were connected to an outlet in the chamber with a shop vacuum being used to pull the air through and trap the particles with the surface tension of the water.

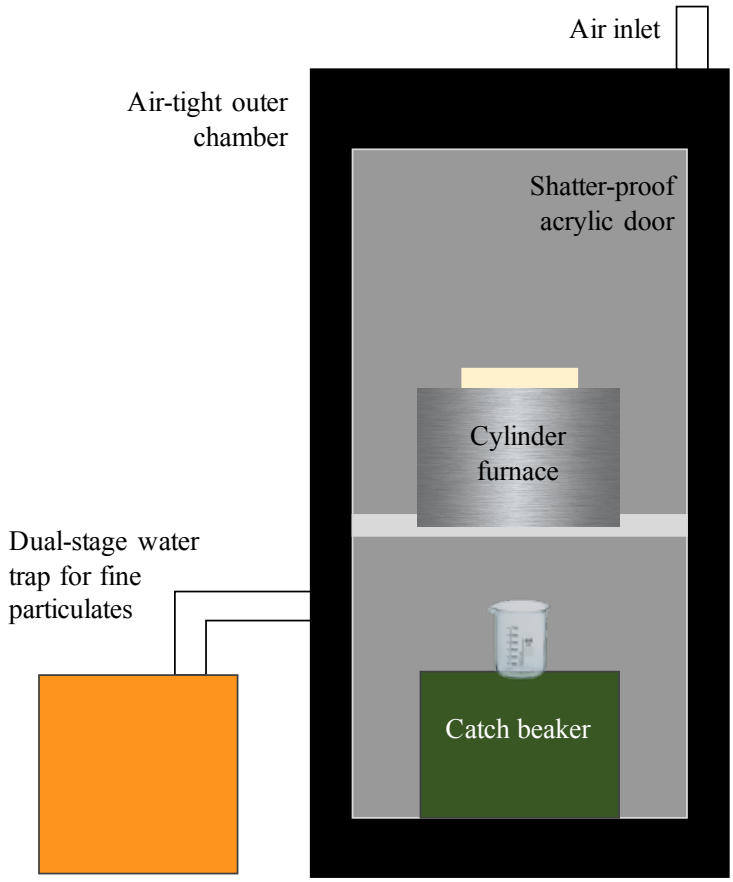

Figure 34 Custom combustion furnace designed and built by author in-house.

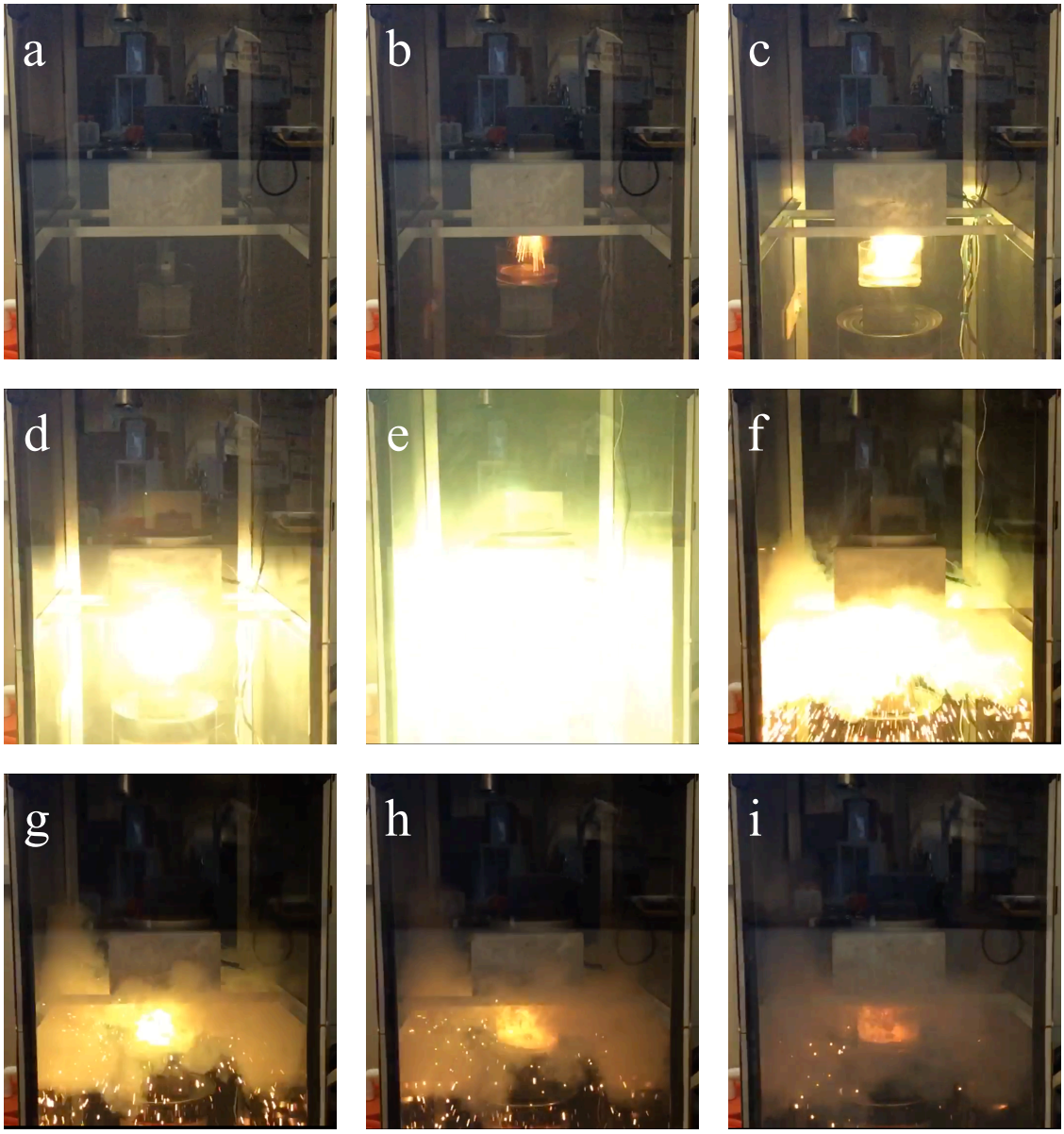

Figure 35 Series of still from video shot at 60 fps of a CaB_6 combustion. Image **a** is pre-ignition, **b** is ignition, **c-f** are propagation and **h-i** are post-combustion.

The author also used the opportunity for customization to address the issue of powder ejection: at the proper intensity require to fully react the boron precursor, the majority of the ensuing powder is ejected from the Pyrex beaker. This obviously presents an issue in terms of powder yield, addressed by orienting the beaker containing the dried

precursor with the opening down so that the contents would be expelled out of the bottom of the furnace into a "catch" beaker waiting below. To increase beaker longevity, reduce borosilicate contamination and facilitate powder collection, a thin layer of NaCl (99.0% purity, Alfa Aesar) is spread along the bottom of the catch beaker to prevent contact of the glass with the newly synthesized hexaboride powder. The NaCl is then removed by a simple soak in water, in which it is dissolved and then decanted off the powder. Figure 35 depicts a combustion in the custom furnace as a series of still frames shot at 60fps.

After removal of the salt, the as-synthesized hexaboride powder is dried and weighed. The presence of several oxygen sources (nitrate, carbohydrazide, air) ensures a degree of precursor oxidation in the form of metal oxides, borates and metal borates. All of these oxide phases are soluble in HCl, and can be removed with a concentrated solution of 80 vol% HCl (36.5-38%, Alfa Aesar) and 20 vol% water (type II purified) from the hexaboride compounds, which are only barely soluble in HCl (to such a low degree that we will refer to them insoluble here). 2 g of as-synthesized hexaboride powder is stirred (or "washed") in 100 mL of this concentrated HCl solution for 10 minutes, followed by two 10-minute purified water washes with 100 mL of water each. After each wash the suspensions are separated in 50 mL Corning polypropylene tubes and spun at 6000 rpm for 10 minutes in an Eppendorf model 5810 centrifuge and subsequently decanted. Powders are dried overnight in air at 353 K after the final water wash, and appear dark brown or black to the naked eye. SEM images of the HCl-washed powders can be seen in Figure 36 through Figure 41.

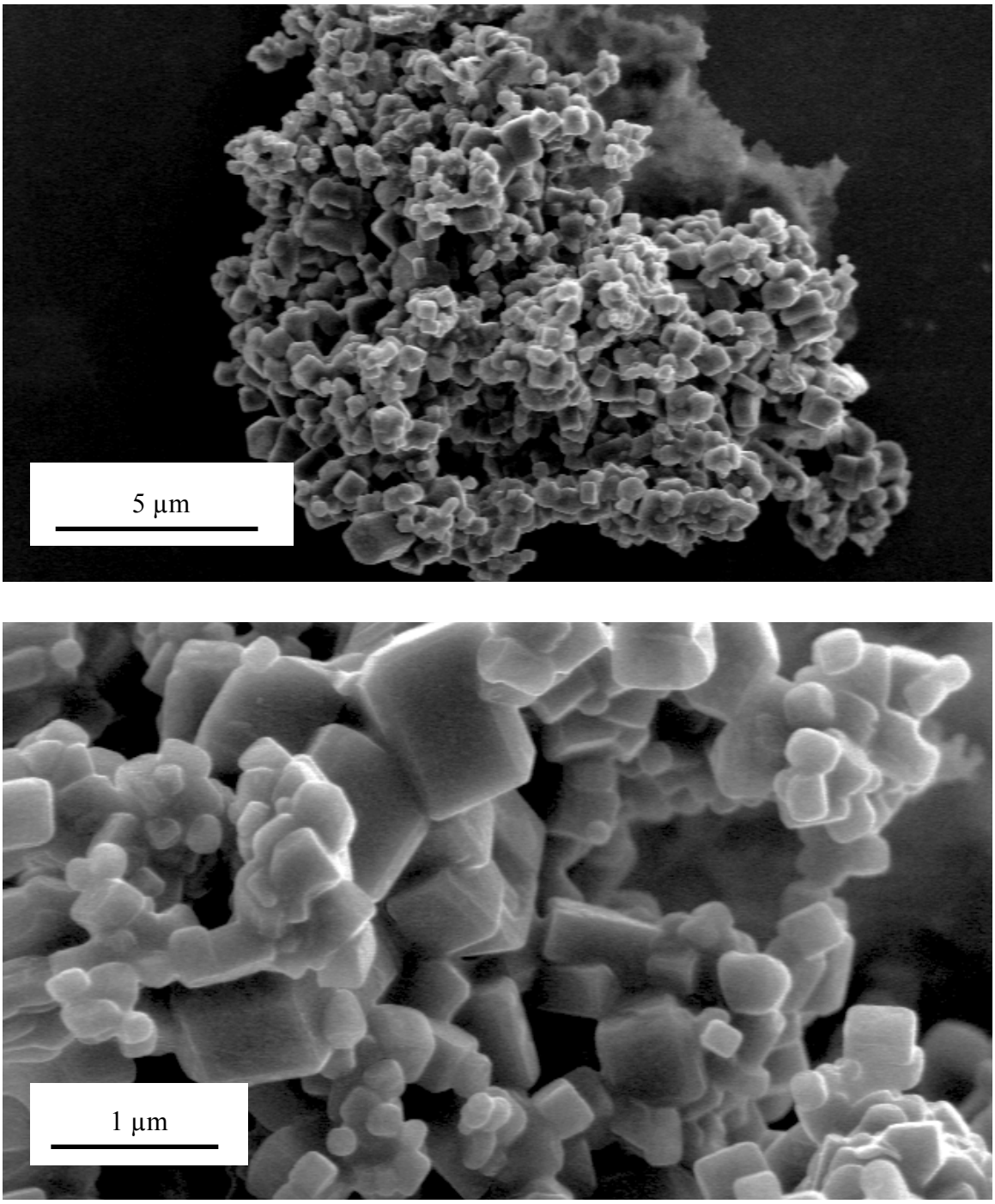

Figure 36 Scanning electron micrographs of CaB_6 powders.

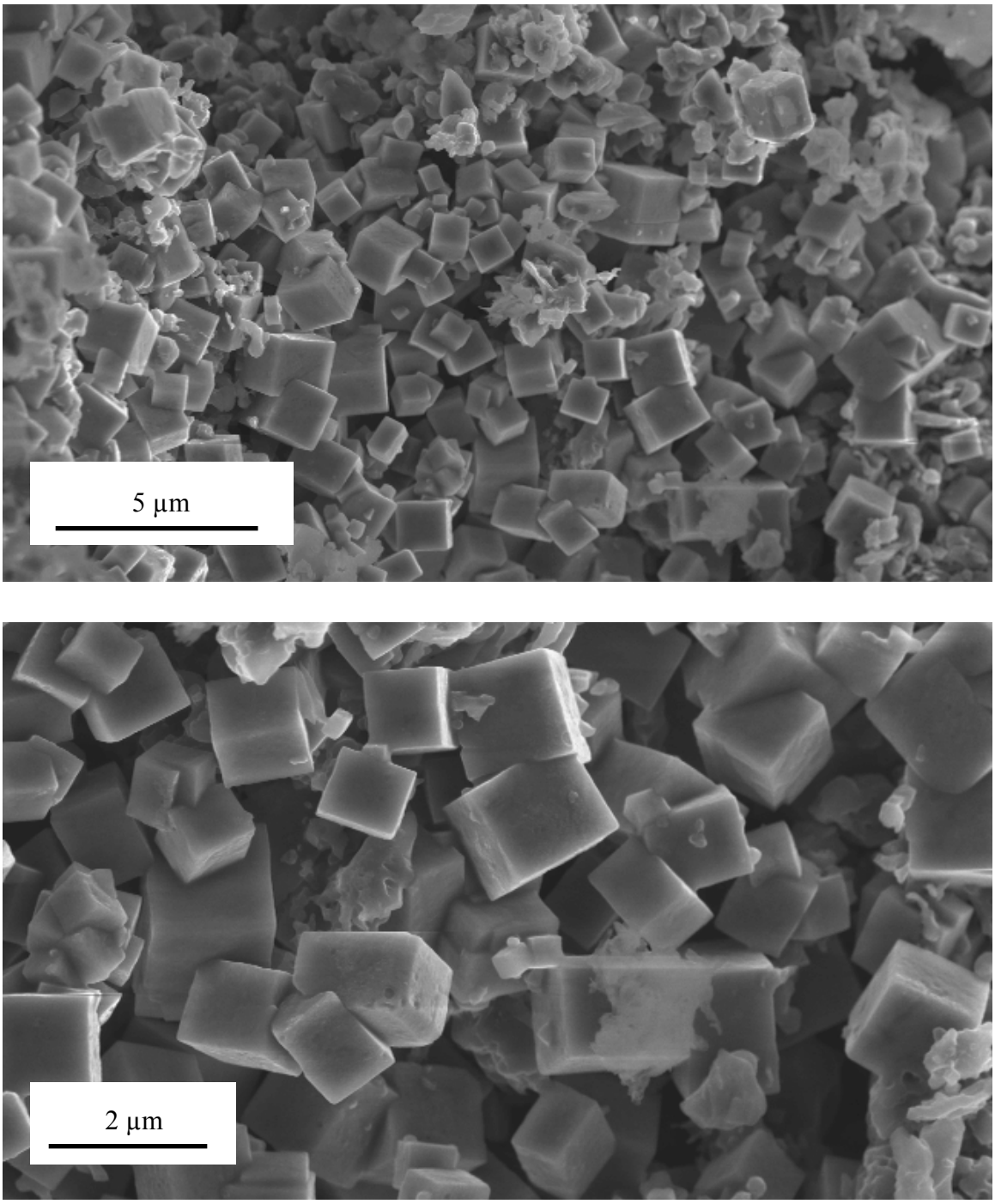

Figure 37 Scanning electron micrographs of SrB_6 powders.

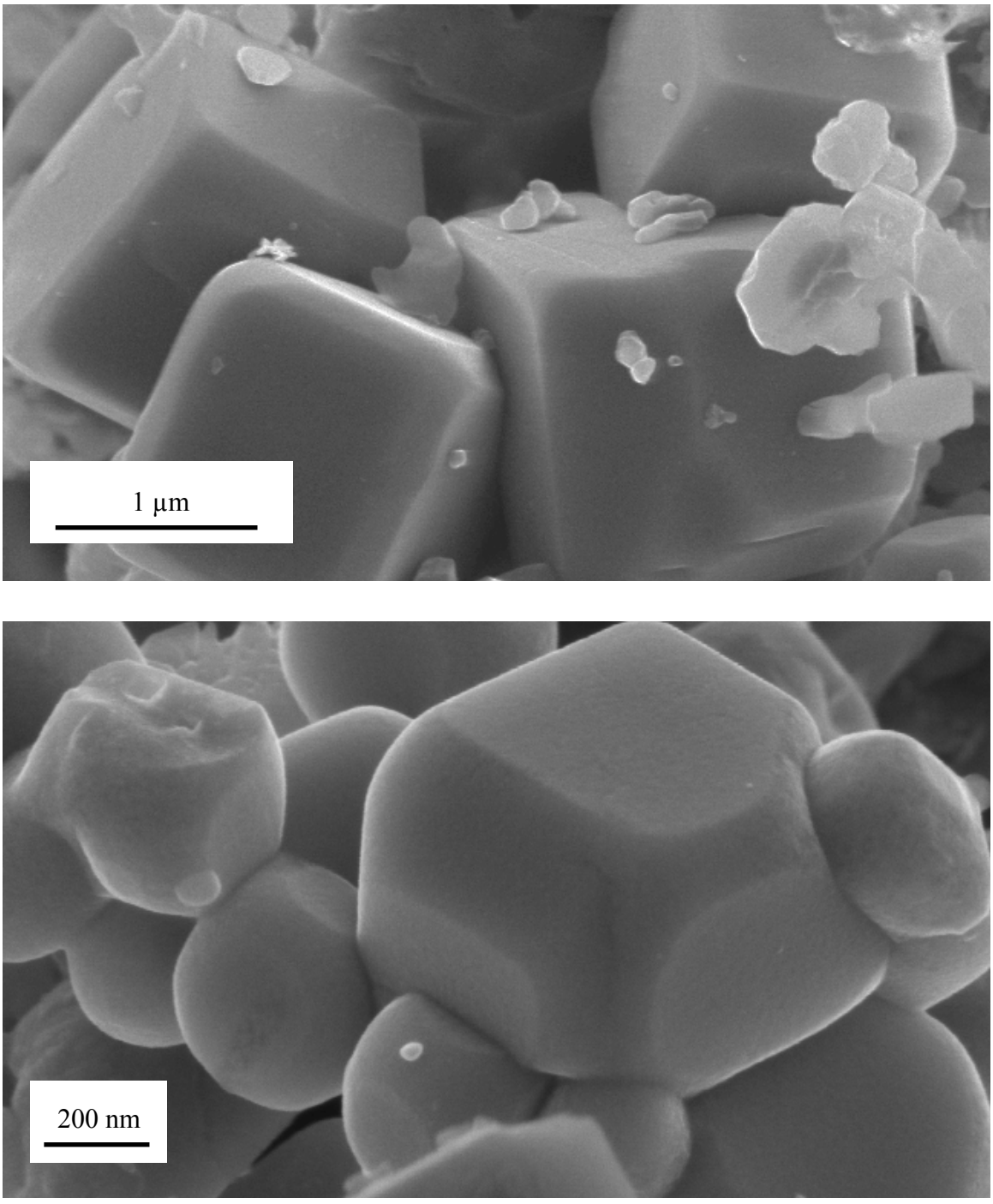

Figure 38 Scanning electron micrographs of BaB_6 powders.

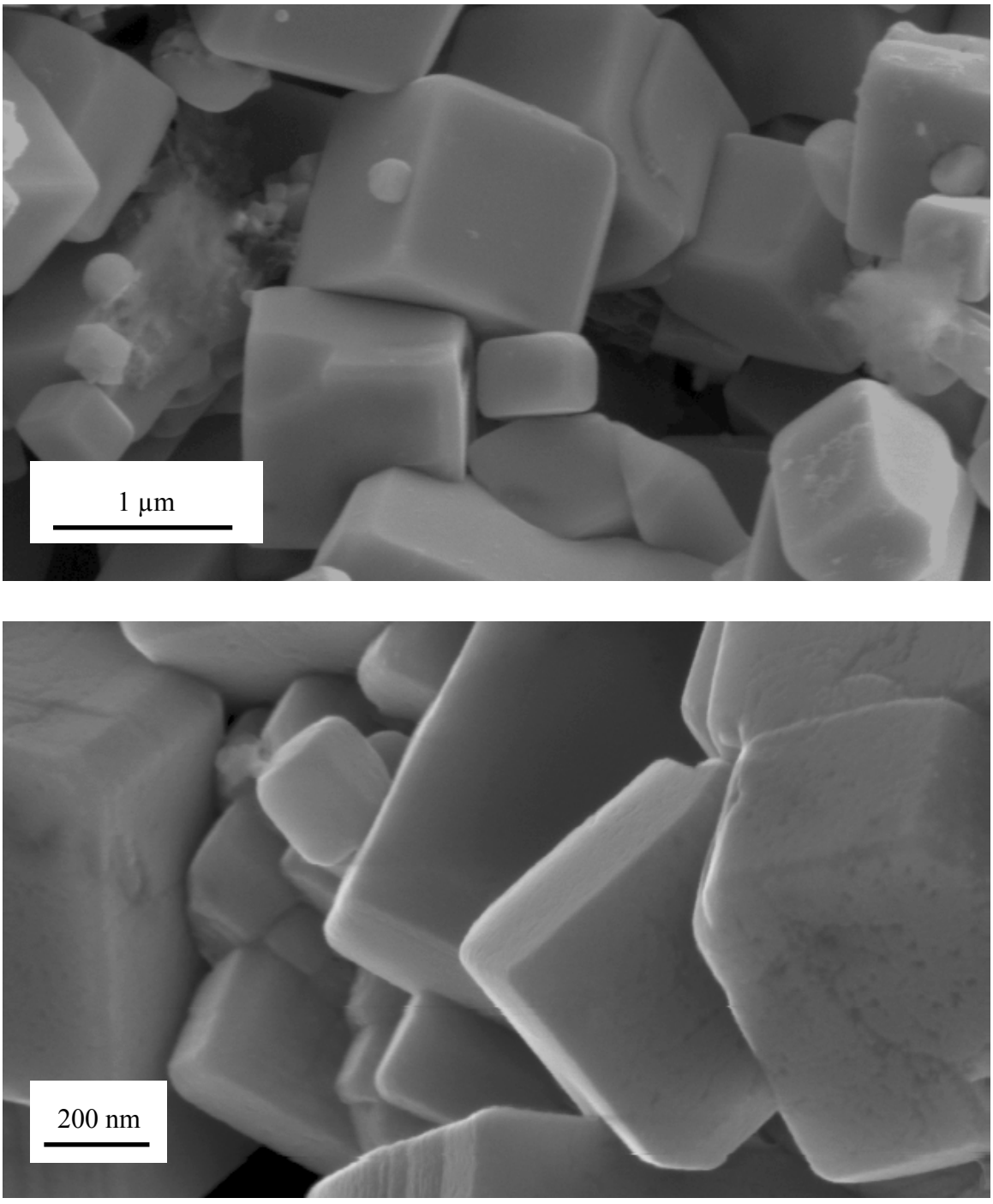

Figure 39 Scanning electron micrographs of CaB_6 powders.

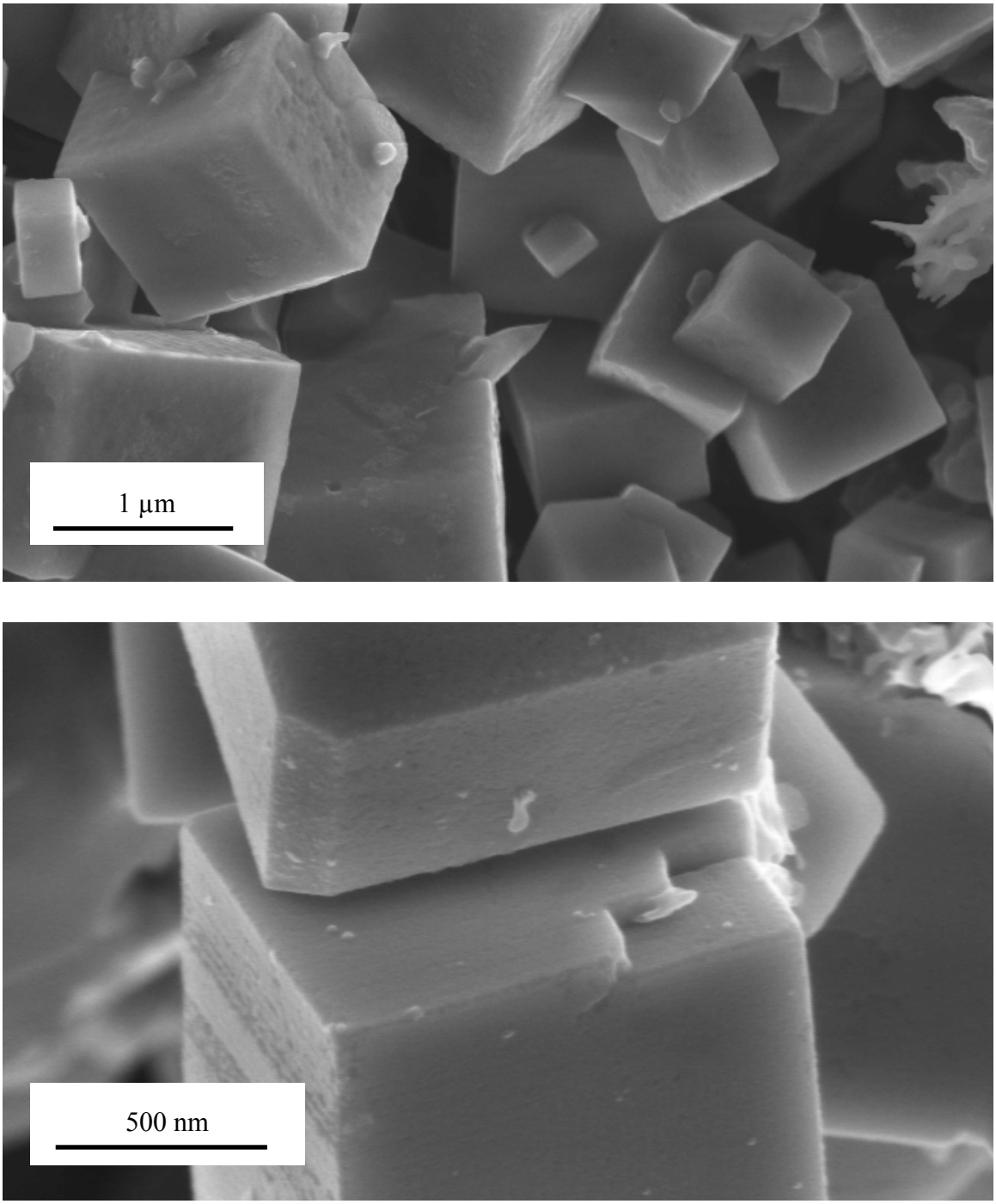

Figure 40 Scanning electron micrographs of SrB_6 powders.

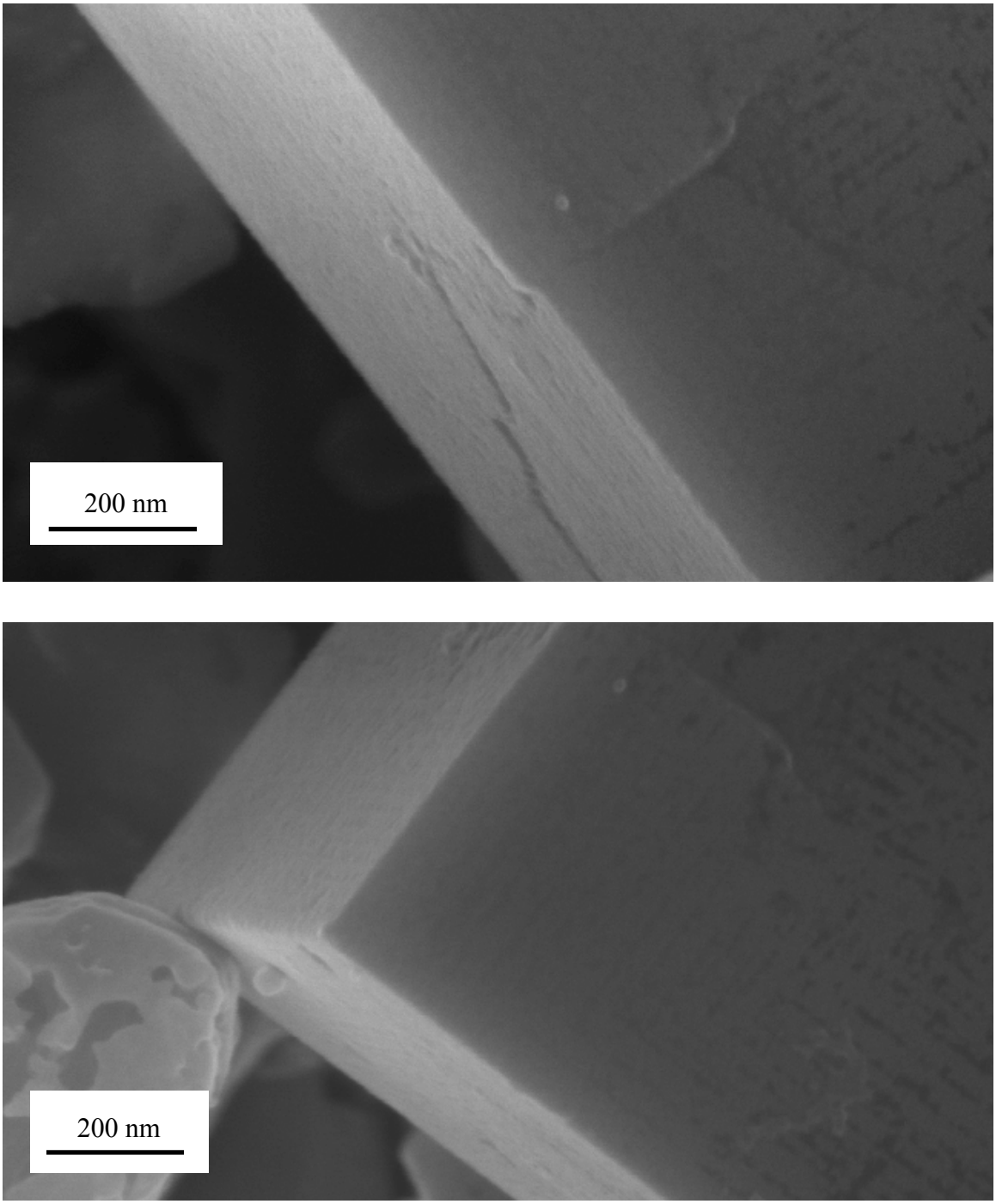

Figure 41 Scanning electron micrographs of CaB_6 powders.

2.2. Heat Treatments

Alkaline-earth hexaboride powders were heat treated in two different manners: **a)** under vacuum in an FCT Systeme D-25 spark plasma sintering unit under 50 MPa at temperatures between 1273 and 1773 K, with a heating rate of 100 K/min and cooling rate of 50 K/min. Between 3 and 5 g of powder was placed in 18.75 mm graphite dies lined with graphite foil, resulting in disks measuring ~5 mm in thickness. **b)** under vacuum in a Thermal Technology Inc. high-temperature graphite vacuum furnace at $8x10^{-10}$ MPa with temperatures between 1273 and 1973 K using a heating and cooling rate of 15 K/min. 2 g of powder was placed in a boron nitride crucible and placed in the center of the graphite furnace, beneath the main thermocouple. Samples that underwent sintering from the higher temperatures were cut with diamond blades and polished with diamond pads in preparation for characterization. In every single-temperature heat treatment, the as-synthesized hexaboride powders were used.

2.3. Consolidation

Alkaline-earth hexaboride powders were consolidated using the same FCT Systeme D-25 spark plasma sintering unit located at Alfred University in Alfred, NY. Powder was placed in 18.75 mm graphite dies (Electrodes, Inc.) lined with graphite foil and pre-pressed to 10 kN. Target thickness for consolidated samples is approximately 5 mm, which requires between 3 and 5 of powder depending on the composition, and therefore density, of the alkaline-earth hexaboride. Dies were wrapped with a carbon felt jacket and placed between two graphite cones within the SPS chamber. All sintering was performed under vacuum and the SPS chamber was flooded with argon at the end of each run. Sintering runs were always performed in the same order: 1) pressing of sample to

desired pressure 2) 50% power heating until optical pyrometer measures 673 K on die surface 3) 70% power heating to the desired maximum temperature 4) simultaneous release of pressure and temperature at consistent ramp down to ambient conditions 5) flood furnace with argon gas.

The sintering temperature used in an SPS run is dependent on several factors, and may vary from instrument to instrument. When a sample has never been sintered by SPS, it is customary to perform trial runs to determine the sintering behavior of the material. There are many parameters that can be altered in an SPS, including force, heating rate, hold temperature, cooling rate, % power and pulse time. Many of these parameters are set based on the operator's experience with the instrument and the sintering behavior of similar materials. For hexaboride consolidation, the heating and cooling rates were fixed to 100 K/min and 50 K/min, respectively, while the force was fixed at 14 kN (50 mPa with the 18.75 mm dies). The first trial run involves heating the sample at 100 K/min until a noticeable peak in the piston speed indicates that densification is occurring. If the piston speed flat lines after this peak, then the temperature corresponding with the end of that peak is deemed the sintering temperature.

As the SPS used in these experiments utilizes an optical pyrometer focused on the outer die wall, the reported temperature is lower than the actual inner temperature of the sample. This difference can be accounted for using from a calibration study comparing the outer die wall temperature with the more accurate value measured by the top optical pyrometer [196]. Calibrated temperatures will be considered for the remainder of the discussion (i.e., 1723 K is calibrated to 2007 K).

$$T_{top} = 1.364T_{side}\text{-}342.9 \quad \text{Equation 6}$$

2.4. Characterization

X-ray diffraction (XRD) patterns were collected using a Bruker D2 Phaser X-ray Diffractometer (Bruker Co., Karlsruhe, Germany). All measurements were taken at room temperature using monochromatized copper radiation ($\lambda = 1.54060 \times 10^{-10}$ m) and Rietveld refinements were performed using TOPAS. Powder XRD samples were prepared by tight packing within a polymer holder against a flat surface, while solid sintered samples were cut with a diamond blade, polished with diamond pads and supported by a polymer holder.

Scanning electron micrographs and energy dispersive spectroscopy maps were obtained with an FEI Quanta environmental scanning electron microscope (ESEM) or an FEI Sirion column ultra-high resolution scanning electron microscope (UHRSEM). Powder SEM samples were dispersed in acetone and a single drop was placed on a chip of single crystal silicon to dry, while solid sintered samples were cut with a diamond blade, polished with diamond pads and supported by an aluminum pin stub. The conductivity of alkaline-earth hexaborides negates the need for sputter coating.

Atomic resolution transmission electron micrographs were obtained with a JEM ARM-200CF transmission electron microscope (HRTEM) outfitted with both energy dispersive X-ray spectroscopy (EDXS) and electron energy loss spectroscopy (EELS) detectors. TEM samples were made by embedding hexaboride powder in silicon and thinning by polishing and focused ion beam milling. TEM images were analyzed with GATAN to produce fast Fourier transformations (FFTs) and measure d-spacings.

Density values were obtained by the Archimedes method involving three measurements on the same solid specimen – one dry, one saturated with water using

moderate vacuum and one saturated with water submerged in water. Density values are reported as a percentage of the theoretical density.

2.5. Diffusion Measurements

Diffusion measurements in alkaline-earth hexaboride samples were obtained by observing the relative movement of the metal cations. This was accomplished by creating diffusion couples formed by sintering together two previously consolidated hexaboride specimens with different metal cations. A sample of CaB_6 produced by combustion would be sintered by SPS at 1573 K and then polished down to 1 micron with diamond pads to remove graphite and obtain a flat surface. It was then combined with a SrB_6 sample prepared in the same fashion in a graphite die and re-sintered at 1723 K for 5 minutes, using heating and cooling rates of 100 K/min and 50 K/min, respectively, and a maximum force of 5 kN. Two identical diffusion couples were prepared, with the only difference being orientation in the SPS; sample 1 was oriented the CaB_6 sample down while sample 2 was oriented SrB_6 sample down. After re-sintering, the samples were cut in half perpendicular to the interface plane and polished with diamond pads down to 6 microns. The interfaces were then imaged with backscattered SEM and Sr and Ca elemental maps were created using energy dispersive X-ray spectroscopy (EDXS). EDX mapping of diffusion-couple cross-sections revealed the presence of Ca atoms on the SrB_6 side and Sr atoms on the CaB_6 side. EDX maps were transformed to numerical data by analyzing pixel brightness in ImageJ and plotted as concentration normal to the interface. Concentration data was only collected for metal atoms in opposing MB_6 pellets (i.e. Ca in SrB_6) based on the interface location determined by the SEM images, and then mirrored and normalized so that an error

function (ERF) fit would result in an interface concentration of 0.5 (under the assumption that the time-temperature profile for each sample was the exact same). Five of these profiles were created for both Ca and Sr for each diffusion couple and averaged together, resulting in four final profiles: Ca concentration with CaB_6 pellet oriented down, Ca concentration with SrB_6 pellet oriented down, Sr concentration with CaB_6 pellet oriented down and Sr concentration with SrB_6 pellet oriented down. The four final concentration profiles were fit using an ERF (Equation 7) in Origin 2016.

$$C(x,t) = A + B\ erf\left(\frac{x}{\sqrt{4Dt}}\right) \quad \text{Equation 7}$$

Error function fits were based on the non-steady diffusion characteristics of these diffusion couples. Concentration-dependent diffusivity can be derived starting with Fick's first law [198]:

$$J = -D\frac{\partial N}{\partial x} \quad \text{Equation 8}$$

where J is the flux (number of atoms passing through a unit area per unit time), D is the diffusion coefficient and $^{\delta N}/_{\delta x}$ is the gradient of matter as a function of position. Fick's second law is a partial differential equation describing how one-dimensional diffusion causes the concentration at position x to change with time:

$$\frac{\partial C(x,t)}{\partial t} = D\frac{\partial^2 C(x,t)}{\partial x^2} \quad \text{Equation 9}$$

Boltzmann [199] and Matano [200] have shown that the diffusion coefficient is also dependent on the concentration at a given x and t and the Boltzmann transformation:

$$\eta = \frac{x\text{-}x_M}{\sqrt{t}} \quad \text{Equation 10}$$

where x is the distance and x_M is the Matano interface. After applying this transformation, the partial derivatives in the diffusion equation become:

$$\frac{\delta\eta}{\delta x} = \frac{1}{\sqrt{t}} \quad \text{Equation 11}$$

and

$$\frac{\delta\eta}{\delta t} = \frac{-(x-x_M)}{2t^{3/2}} \quad \text{Equation 12}$$

Plugging these partial derivatives back into the diffusion equation yields:

$$\frac{-(x-x_M)}{2t^{3/2}}\frac{\delta C}{\delta\eta} = \frac{\delta}{\delta x}\left(D\frac{1}{\sqrt{t}}\frac{\delta C}{\delta\eta}\right) \quad \text{Equation 13}$$

and then:

$$\frac{-(x-x_M)}{2t^{3/2}}\frac{\delta C}{\delta\eta} = \frac{\delta}{\delta\eta}\frac{\delta\eta}{\delta x}\left(\frac{D}{\sqrt{t}}\frac{\delta C}{\delta\eta}\right) = \frac{\delta}{\delta\eta}\frac{1}{\sqrt{t}}\left(\frac{D}{\sqrt{t}}\frac{\delta C}{\delta\eta}\right) \quad \text{Equation 14}$$

So that the diffusion equation becomes:

$$-\frac{\eta}{2}\frac{\delta C}{\delta\eta} = \frac{\delta}{\delta\eta}\left(D\frac{\delta C}{\delta\eta}\right) \quad \text{Equation 15}$$

Keeping in mind that this is an ordinary differential equation and using the assumptions that $c(-\infty) = c_0$ and $c(\infty) = 0$, we can cancel a $\delta\eta$ from each side and integrate:

$$\int_0^c \frac{-\eta}{2}\,dc' = D\frac{\delta c}{\delta\eta}\Big|_{c=0}^{c} \quad \text{Equation 16}$$

If we assume time *(t)* is a constant and use $\frac{\delta c}{\delta z} = 0$ at $c = 0$, and then solve, it becomes:

$$D(c) = \frac{-1}{2t}\frac{\delta z}{\delta c}\Big|_c \int_0^c z\,dc' \quad \text{Equation 17}$$

Although the error function fit can be used to calculate a diffusion coefficient for concentration-dependent diffusivity, a different approach was used to numerically compare diffusivity between the samples. Differences in diffusivity was analyzed by comparing the total dopant per unit area *Q(t)*, obtained by integrating the concentration profile along *x*:

$$Q(t) = \int_0^x C(x,t)dx$$ Equation 18

3. Consolidation Behavior of Alkaline-Earth Hexaboride Materials

3.1. Results and Discussion

The challenge of consolidating refractory materials stems from their high melting temperatures and alkaline-earth hexaborides are no exception. Another complication is the tendency of borides to oxidize at high temperatures, imposing the need for an oxygen-free environment during sintering. Although the melting temperatures of hexaborides are above 2300 K, literature reveals that sintering happens at temperatures several hundred degrees below that [5, 31, 33, 45, 127, 141, 201-203]. As discussed in the *Introduction*, the FCT SPS unit is capable of generating these high temperatures in a vacuum environment, which prevents oxidation and even encourages the volatilization of organic residue and some impurities. Comparing the sintering temperatures of hexaborides in and SPS with other methods can only be approximated as the measured value in an SPS is actually that of the outer die wall, but the work completed by Takeda and coworkers provides a decent starting point for sintering these materials in an SPS [5, 31, 33, 45, 127].

Consolidation tests run up to 1820 K revealed that the alkaline-earth hexaboride powders produced by combustion underwent two sintering events, with the second one concluding at up to 1768 K. These sintering events are revealed in the SPS data by sudden increase in piston speed and travel (piston speed is the derivative of piston travel), which signifies a densification of the powder. Figure 42 contains the measured temperature (blue line), piston travel (green line) and piston speed (black line) values for a) CaB_6, b) SrB_6 and c) as-prepared $(Sr_{0.5}Ca_{0.5})B_6$ powders during SPS consolidation.

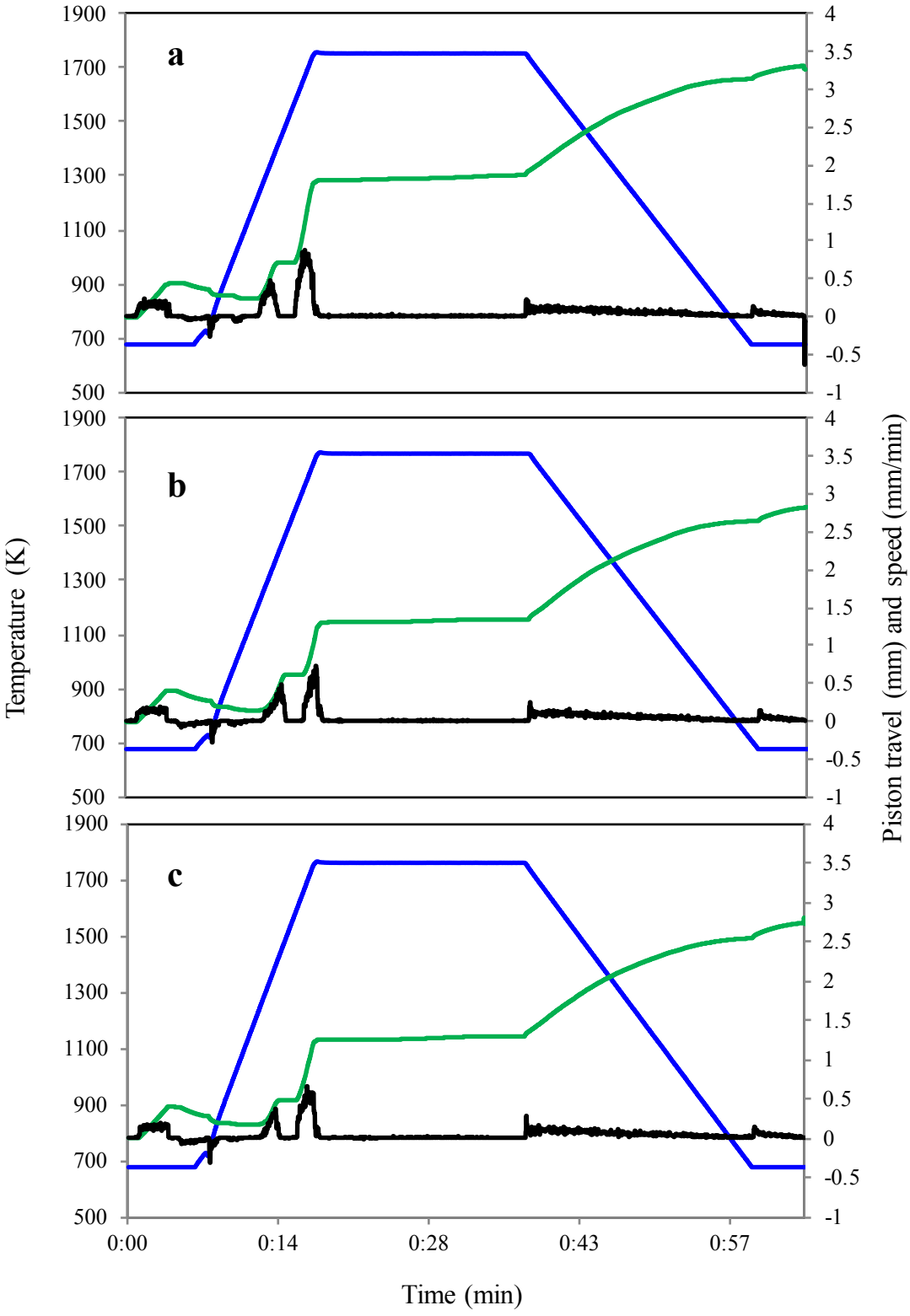

Figure 42 Sintering plots for preliminary runs of a) CaB_6 at 1753 K b) SrB_6 at 1768K and c) $Sr_{0.5}Ca_{0.5}B_6$ at 1763K.

Table 7 SPS parameters used in the consolidation of alkaline-earth hexaboride powders

Composition	Hold Temperature (K)	Hold time (min)	Pressure (Mpa)	Ramp up ($^{K}/_{min}$)	Ramp down ($^{K}/_{min}$)	Relative density (%)
SrB_6	1768	20	50	100	50	99.1
CaB_6	1738	20	50	100	50	98.9
$(Sr_{0.5}Ca_{0.5})B_6$	1753	20	50	100	50	98.6
SrB_6	1768	0.5	50	100	50	98.2
CaB_6	1738	0.5	50	100	50	98.5
$(Sr_{0.5}Ca_{0.5})B_6$	1753	0.5	50	100	50	98.1
SrB_6	1475	0.5	50	100	50	90.3
CaB_6	1425	0.5	50	100	50	89.8
$(Sr_{0.5}Ca_{0.5})B_6$	1475	0.5	50	100	50	90.6

For all three powders, both sintering events occur during the 100 K/min ramp up, with the second event concluding just before the hold temperature. The hold temperatures for each composition were based on the second sintering event and are included in Table 7 along with the temperature of the first sintering event and the remaining sintering parameters. The ramp-up rate of 100 K/min was fast enough to minimize the total time spent at elevated temperatures in order to reduce grain growth, but slow enough to give the powders time to fully densify during the ramp.

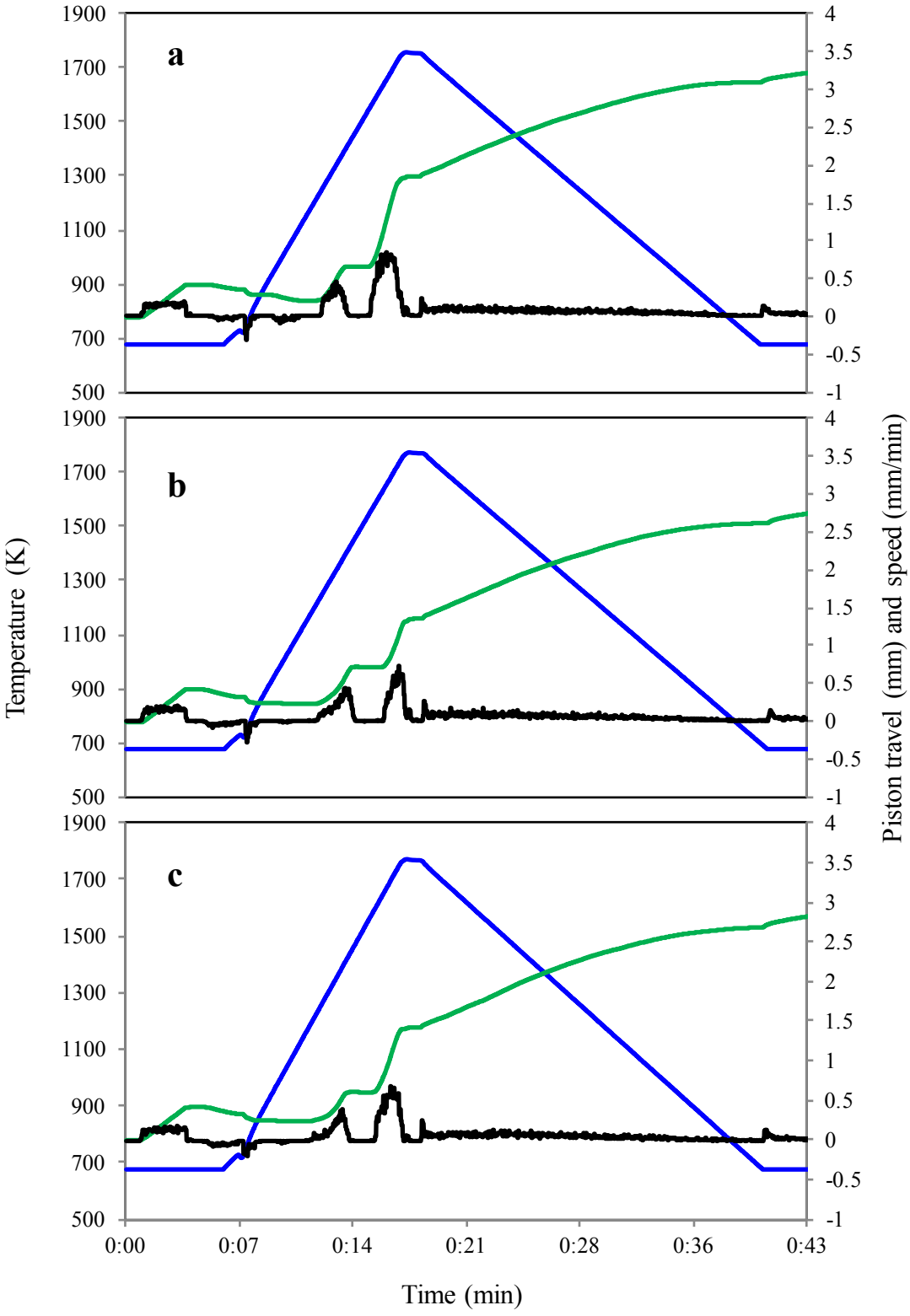

Figure 43 Sintering plots with reduced hold times for a) CaB6 at 1753 K b) SrB6 at 1768K and c) Sr0.5Ca0.5B6 at 1763K

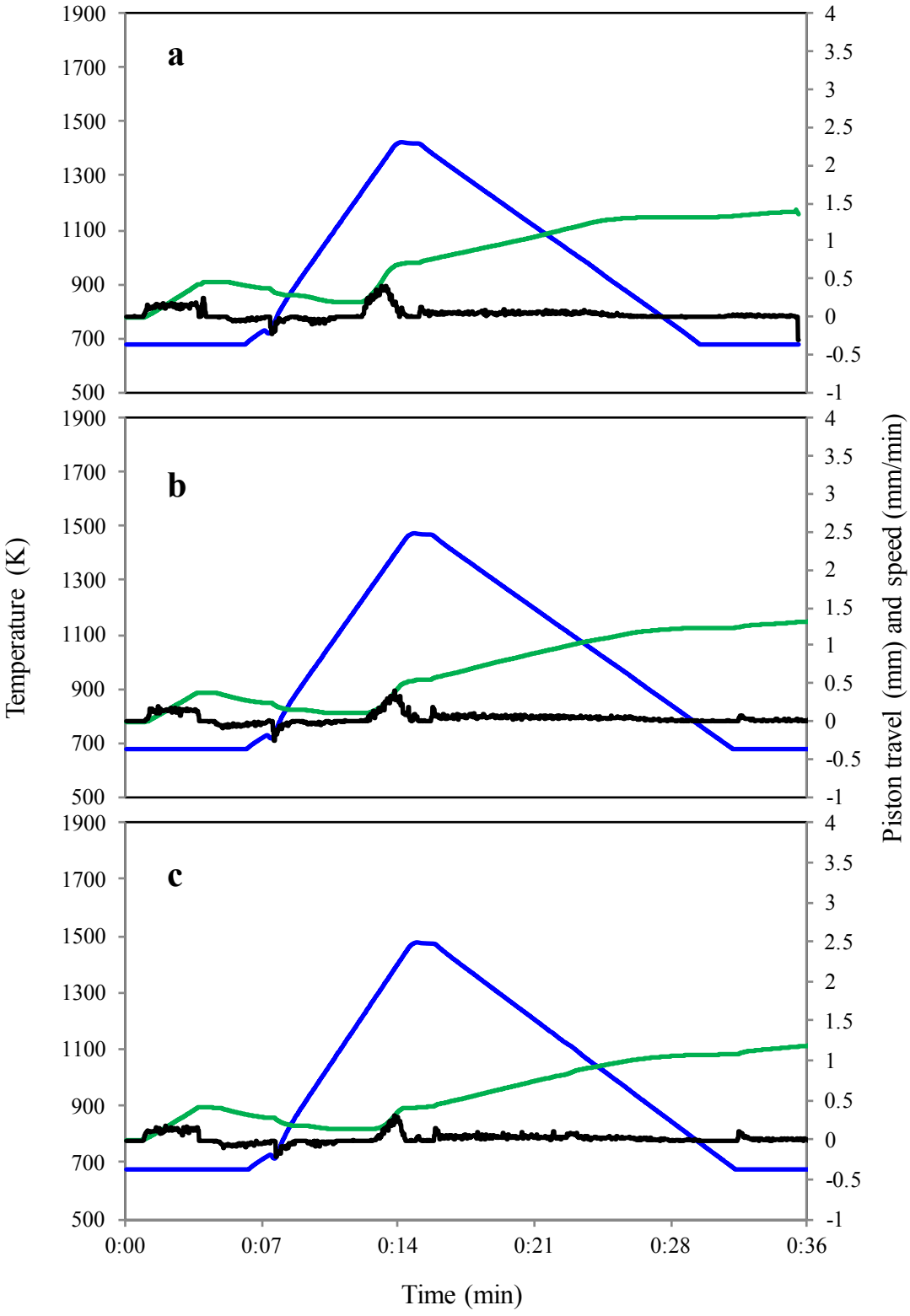

Figure 44 Sintering plots for a) CaB6 at 1425 K b) SrB6 at 1475 K and c) Sr0.5Ca0.5B6 at 1475K

The ramp-down rate of 50 K/min is slower to prevent cracking of the sintered MB_6 pellets from thermal contraction within the die. cracking of the sintered MB_6 pellets from thermal contraction within the die. The 50 MPa of pressure was applied while the powders were at room temperature and released with a controlled ramp down coinciding with the temperature ramp down. A further attempt to minimize grain growth was reducing the hold time from 20 minutes to 1 minute. As seen in Figure 42, the piston travel during the hold for each sample was very minimal and suggests that very little densification occurred during this time. Figure 43 contains the same type of plots but for the samples sintered with a reduced hold time at the same temperatures.

CaB_6, SrB_6 and as-prepared $(Sr_{0.5}Ca_{0.5})B_6$ powders were also sintered to the temperature corresponding to the conclusion of the first sintering event (Figure 44), keeping the remaining sintering parameters the same (listed in Table 7). The resulting specimens appeared porous to the naked eye and measured to ~90% relative density compared to the ~98% relative density of the specimens sintered at full temperature. SEM images of as-prepared $(Sr_{0.5}Ca_{0.5})B_6$ fracture surfaces reveal the difference in grain morphology between after the first and second sintering events (Figure 45). The specimen in Figure 45a is at 90% relative density after the first sintering event (1475 K) and it appears that the particles are fused together creating open porosity but have not grown much since the as-synthesized state of 200-800 nm. The specimen in Figure 45b is at 98% relative density after the second sintering event (1763 K) and at this point the particles have grown and filled the voids from Figure 45a to almost full density. While not representative of every grain in the specimen, Figure 45b shows that the cubic morphology of the as-synthesized powder particles can be maintained as cubic grains.

Additional SEM images of the sample sintered to 98% relative density can be seen in Figure 46.

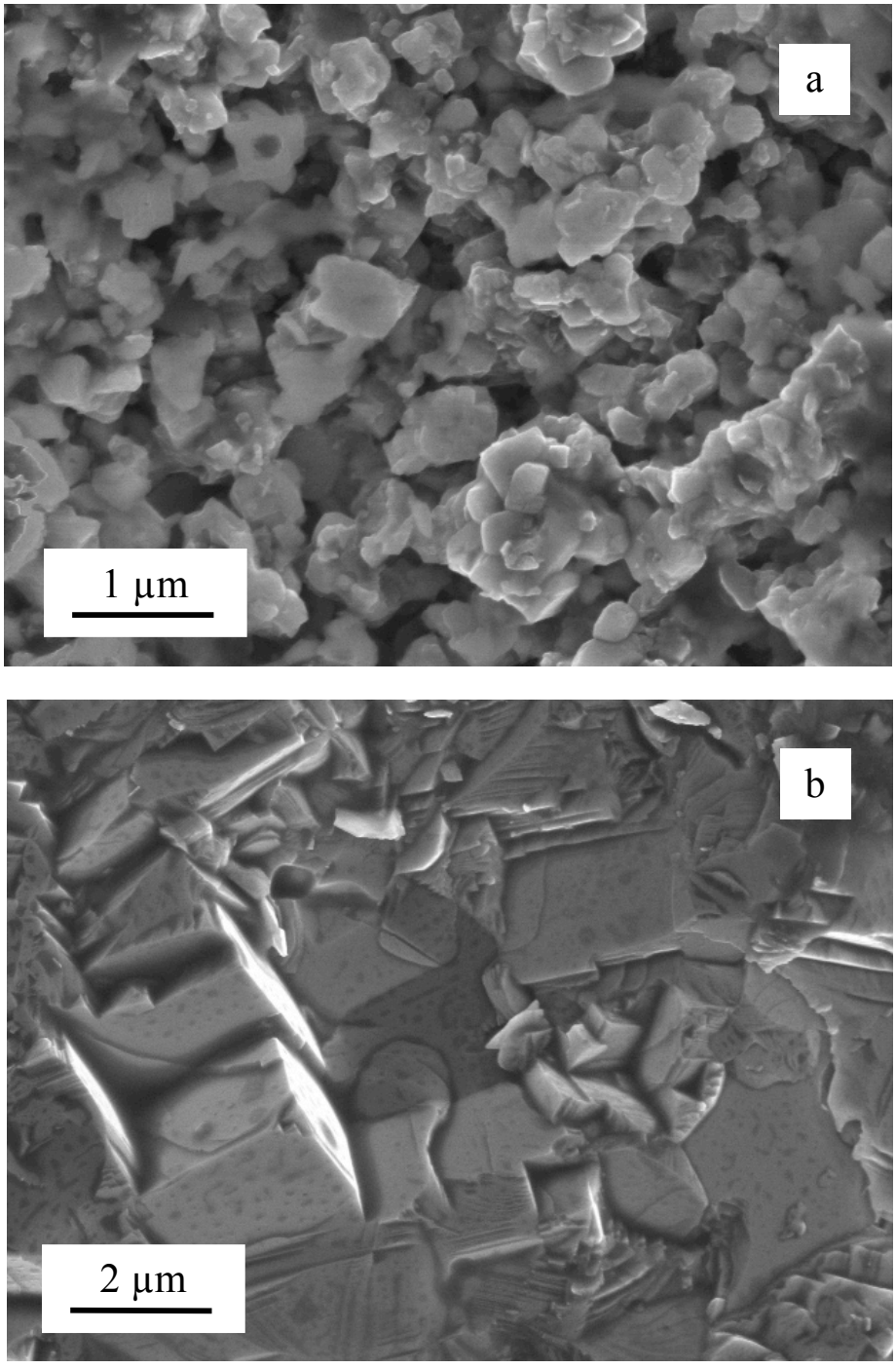

Figure 45 SEM images of $(Sr_{0.5}Ca_{0.5})B_6$ powders sintered to a) the first sintering event at 1475 K and b) the second sintering event at 1763 K.

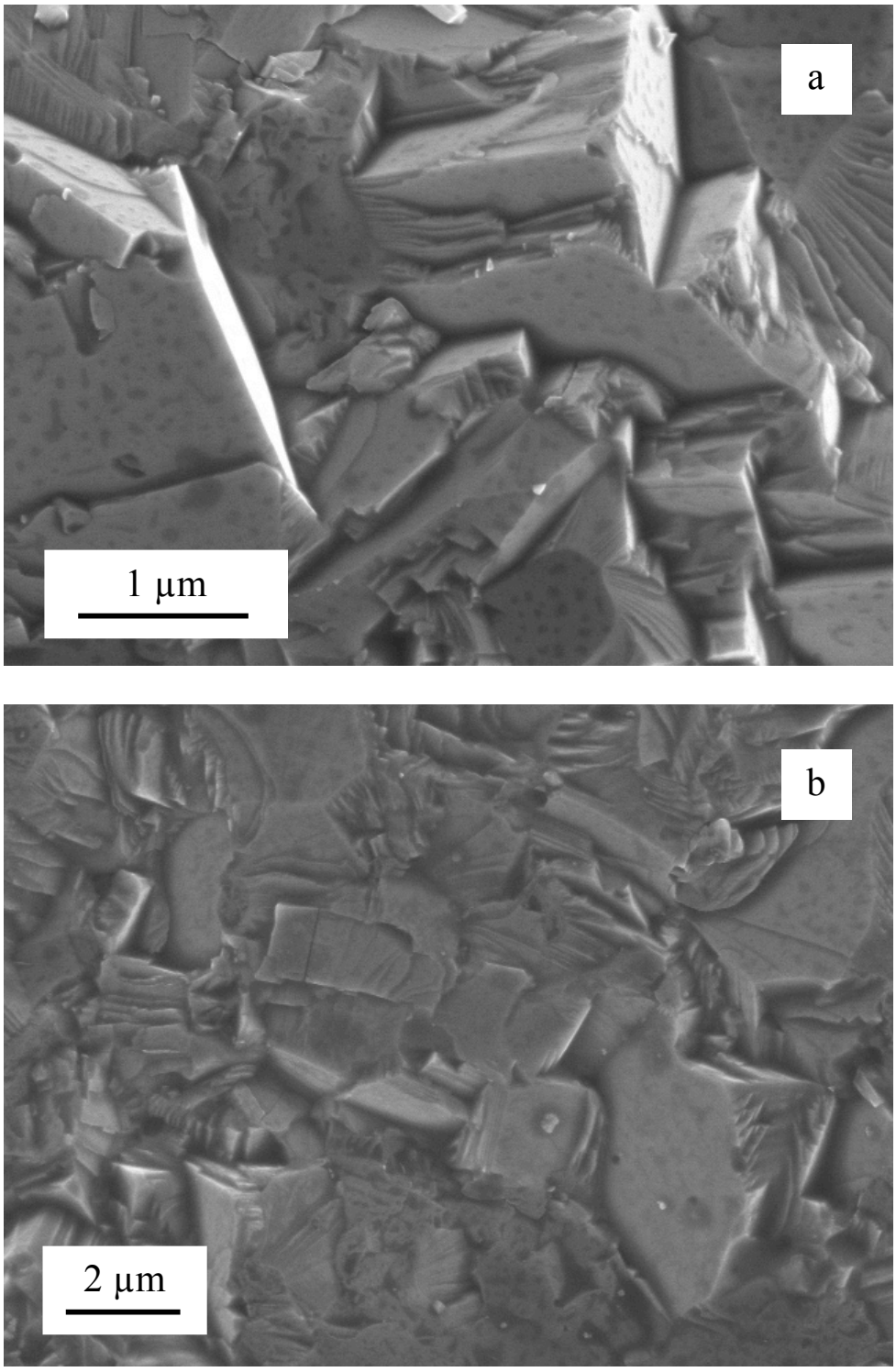

Figure 46 SEM images of $(Sr_{0.5}Ca_{0.5})B_6$ powders sintered 1763 K at two different magnifications.

For future experiments, diffusion couples composed of two different MB_6 compounds needed to be prepared. Diffusion couples are usually composed of two or more solid specimens with smooth surfaces allowing for maximum contact and the transfer of atoms across the interface(s). Due to the success of sintering CaB_6 and SrB_6 powders, these two compounds were chosen for the diffusion couples. The first attempt to create a layered CaB_6-SrB_6 specimen was using a single-step approach, consisting of layering CaB_6 powder and SrB_6 powder together in a graphite die and sintering to the highest temperature required for consolidation (i.e. 1768 K for SrB_6).

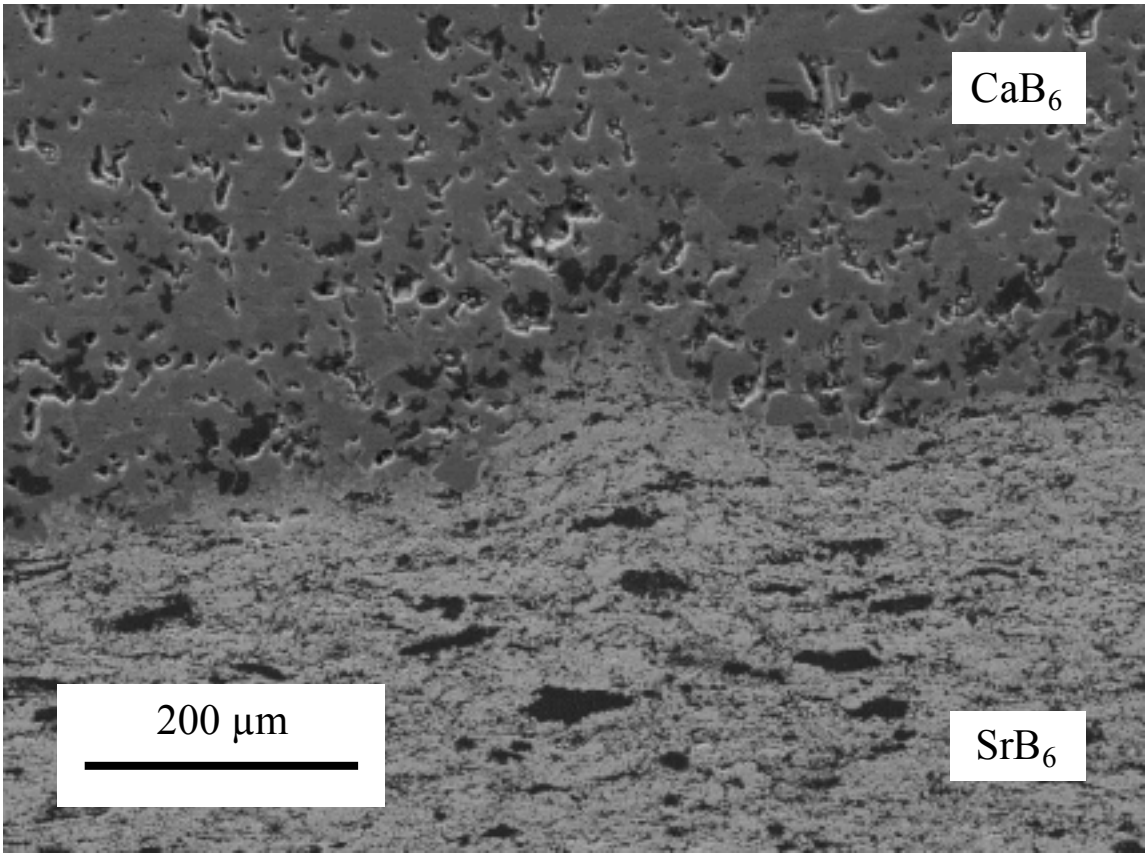

Figure 47 SEM image of CaB_6-SrB_6 diffusion couple sintered using a single-step approach with both raw powders loaded into the graphite SPS die.

This method insured complete interface contact but did not produce a two-dimensional interface (Figure 47) due to the improbable nature of achieving a perfectly flat powder surface before introduction of the second compound. Even if a two-dimensional interface was achieved in the green state, there is no guarantee that it would remain so during densification. The second attempt to create diffusion couples involved the re-sintering of separate CaB_6 and SrB_6 pellets. CaB_6 and SrB_6 powders were sintered to ~98% relative density at 1753 and 1768 K, respectively, and then polished down to 1 μm with diamond pads.

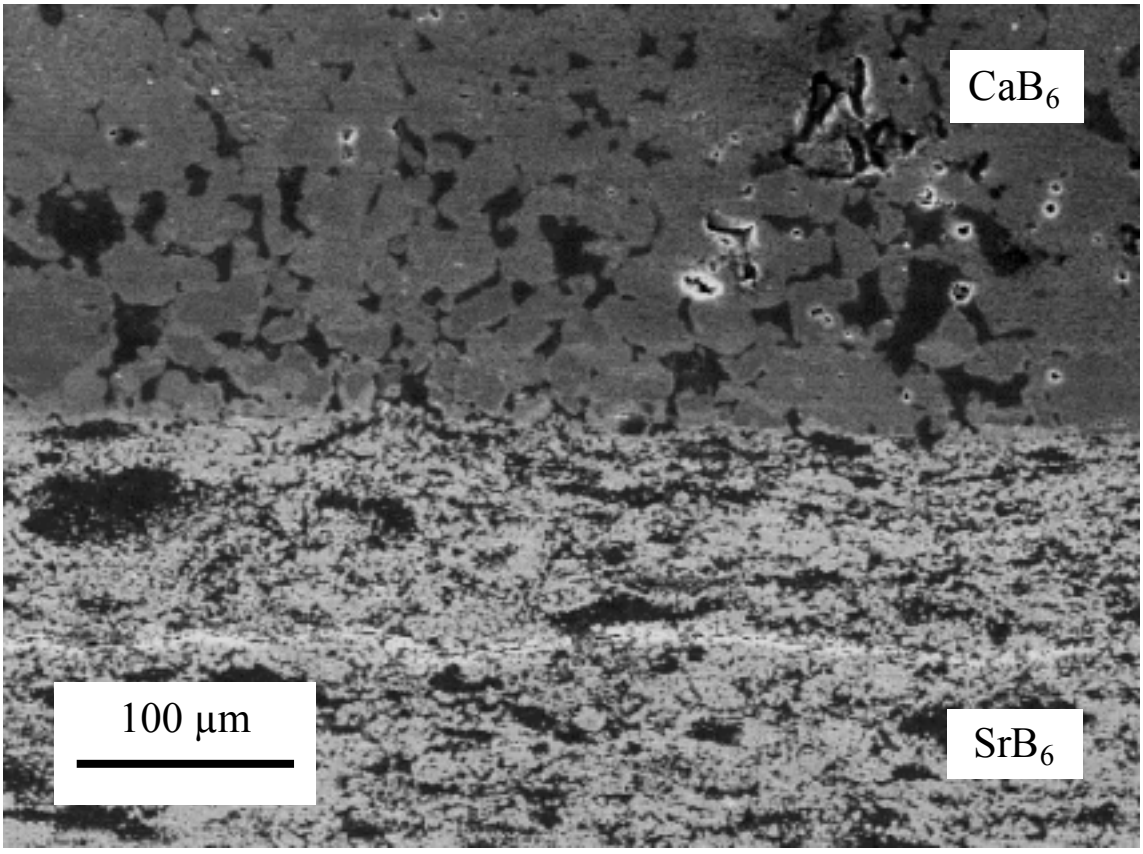

Figure 48 SEM image of CaB_6-SrB_6 diffusion couple sintered using a multi-step method involving the sintering of separate CaB_6 and SrB_6 pellets to nearly-full density and then re-sintering them in the SPS.

The two pellets were then inserted together into a graphite SPS die and re-sintered at 1723 K. Figure 48 shows and SEM image of the interface achieved with this method. Although the interface is closer to two-dimensional than the first attempt (Figure 47), the high density of the individual pellets made polishing extremely difficult and time consuming, often resulting in gaps between the two pellets at the sintered interface.

The third and final attempt to sinter CaB_6-SrB_6 diffusion couples was very similar to the second attempt except that the starting pellets were only sintered to ~90% relative density (1425 and 1475 K for CaB_6 and SrB_6, respectively) before re-sintering. The ~10% decreased density made polishing of the pellets much more efficient and complete, ensuring a more exact interface. The diffusion couple was also sintered at 1723 K and and SEM image of the resultant interface can be seen in Figure 49. This method results in a high level of interface contact and produces a clean two-dimensional interface and was chosen to produce the diffusion couples used later in the research.

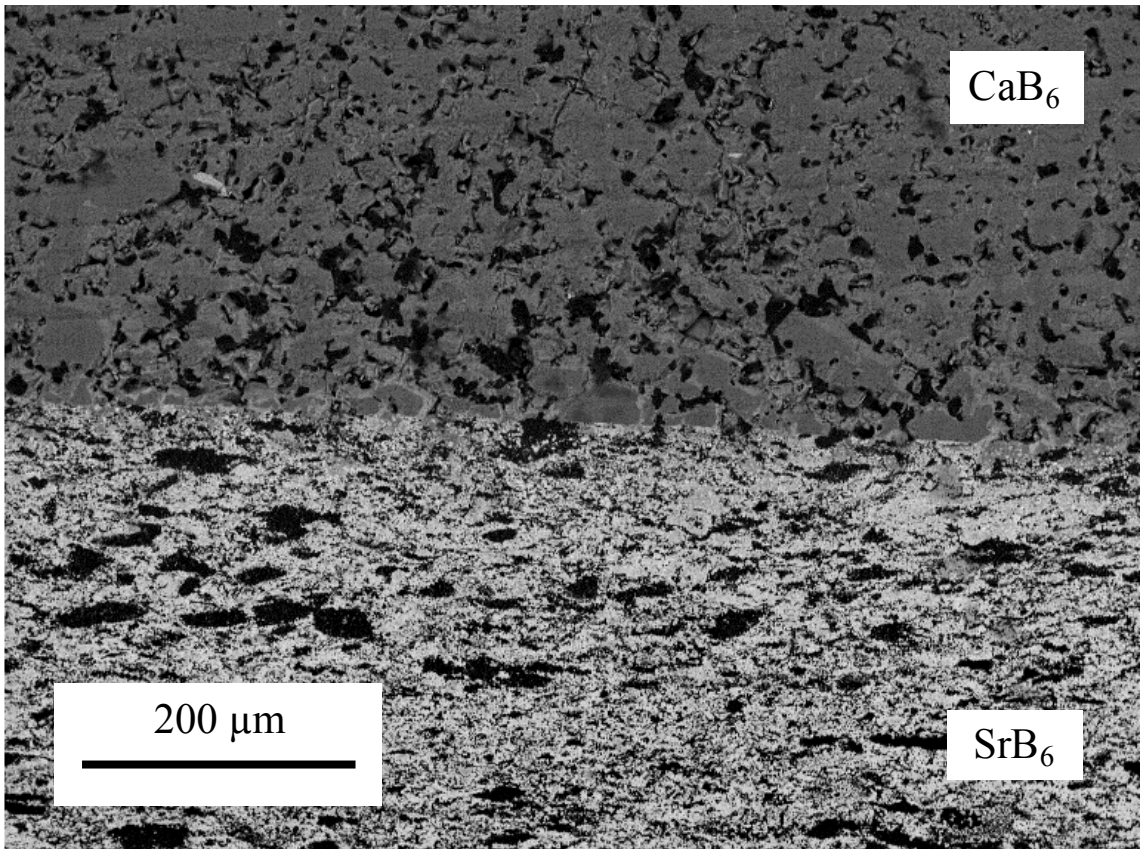

Figure 49 SEM image of CaB_6-SrB_6 diffusion couple sintered using a multi-step method involving the sintering of separate CaB_6 and SrB_6 pellets to ~90% relative density and then re-sintering them in the SPS.

4. Phase Stability of Mixed-Cation Alkaline-Earth Hexaborides

4.1. Results and Discussion

As discussed in the *Introduction*, hexaborides compounds have very similar lattice parameters and therefore readily form solid solutions with one another, with the largest and smallest lattice parameters only differing by four percent (0.4093 nm for ThB_6 and 0.4262 nm for BaB_6) [9]. Few studies have fully characterized the behavior of metal hexaboride solid solutions, although attempts have been made to synthesize and study the following (M-N)B_6 systems: (La-Y)B_6 [76], (La-Ba)B_6 [76], (La-Ce)B_6 [72, 204, 205], (La-Na)B_6 [65], (Eu-Y)B_6 [76], (Eu-Ba)B_6 [76], (Ca-Sr)B_6 [31, 45], (Ca-Ba)B_6 [45], (Sr-Ba)B_6 [45], (Ca-Yb)B_6 [31], (Ca-Sm)B_6 [31], and (Gd-Nd)B_6 [203]. Olsen and Cafiero grew single crystals of (La-Eu)B_6, (La-Y)B_6, (Eu-Y)B_6, (La-Ba)B_6 and (Eu-Ba)B_6 from oxide precursors in an aluminum flux and found a negative deviation from Vegard's law in the (La-Eu)B_6 samples (the only example of this detailed by XRD to the best of our knowledge) [76]. They attributed this deviation to the compressibility or weakness of the larger EuB_6 constituent but noted solid solutions over the entire compositional range for all ternary systems except those containing Y, which produced a mixture of MB_6 and YB_4 crystals. Badalyan et al. and Gurin et al. grew single crystals of ternary (La-Ce)B_6 by solution-melt, Al/Pb immiscible system growth and floating zone technique [72, 204]. After characterizing the surface of each crystal with energy dispersive X-ray microanalysis (EDX) and wavelength dispersive X-ray microanalysis (WDX) they found slight variations in the ratio of La:Ce across the length of the crystal. The authors attributed the deviations to the error associated with the analytical technique and the low concentration of Ce in the $La_{1-x}Ce_xB_6$ ($x = 0.01$ to 0.05), and therefore concluded even

distribution of Ce across the crystal. Takeda et al. produced ternary $(Sr\text{-}Ca)B_6$ by borothermal reduction of metal oxides in increments of 25 at.% across the compositional range, and the subsequent powders were consolidated by spark plasma sintering (SPS) at 2073 K, noting that the ternary powders were held at the sintering temperature for 50 min longer than the binary counterparts to ensure uniformity of the specimen [31]. Gürsoy et al. also synthesized hexaborides in the $(Sr\text{-}Ca)B_6$, $(Ba\text{-}Sr)B_6$ and $(Ba\text{-}Ca)B_6$ systems by heating high purity metals with amorphous boron in a high-frequency induction furnace [45]. The powders were also sintered by SPS at temperatures between 1673 and 2173 K. They found that samples in all three systems of $M^1_xM^2_{1-x}B_6$ (x = 0.25, 0.5, 0.75) were monophasic with lattice parameters following Vegard's Law.

In this work, samples were prepared in the ternary systems of alkaline-earth hexaborides for Ca, Sr and Ba using both combustion synthesis [110, 111] and borothermal reduction of carbonates [30]. In the $(Ba\text{-}Sr)B_6$ and $(Ba\text{-}Ca)B_6$ systems, samples containing two hexaboride solid-solutions with varying in compositions were observed. Electron microscopy of these samples showed nano-regimes of solid solutions with varying cation ratios throughout the crystal. Further heat treatments and subsequent x-ray diffraction analysis was used to understand the stability of these biphasic mixtures.

Figure 50 illustrates scanning electron micrographs of the samples prepared by combustion synthesis and borothermal reduction. The samples produced by combustion synthesis had submicron, cubic-shaped particles, whereas those produced by borothermal synthesis had particles that approached tens of micrometers in size.

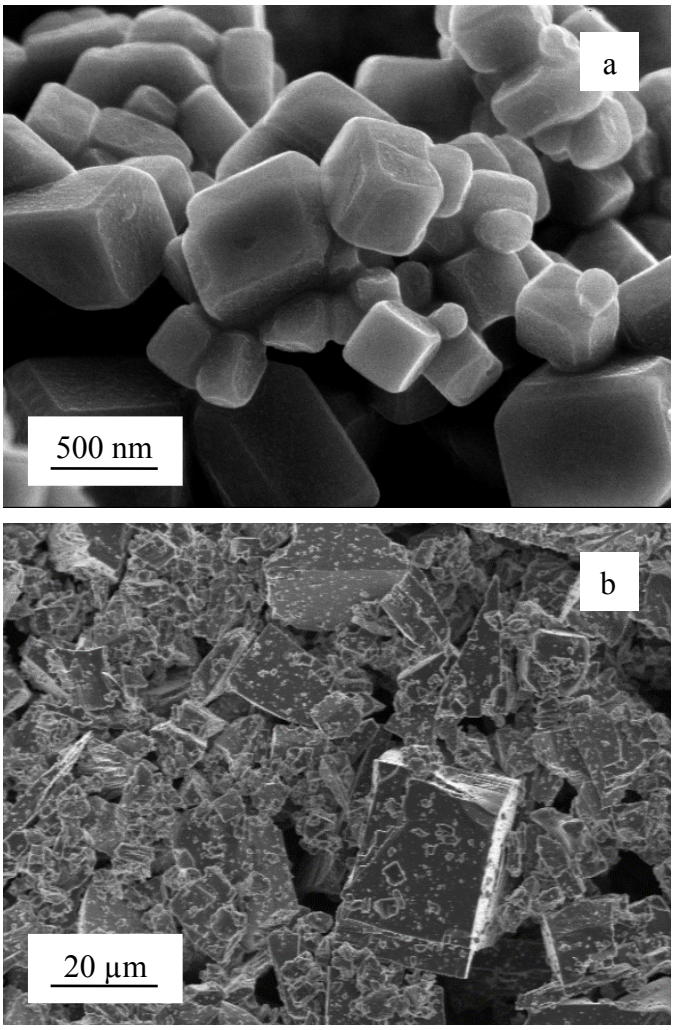

Figure 50 Scanning electron micrographs of CaB_6 produced by a) combustion and b) reduction

The different morphology resulting from the two methods can be attributed in part to the time spent at elevated temperatures. The entire combustion process is completed in under 10 minutes with less than a second spent at temperatures above 1200 K during the production of the adiabatic flame [206, 207]. In contrast, the slow heating rate and long dwell of the borothermal reduction provided the particles more time to grow with a total of 250 minutes spent above 1200 K. XRD patterns collected from the single-metal (binary) hexaboride powders, depicted in Figure 51, result in lattice parameters with

minor percent differences to those in the diffraction database (0.099% for CaB_6, 0.095% for SrB_6 and 0.187% for BaB_6).

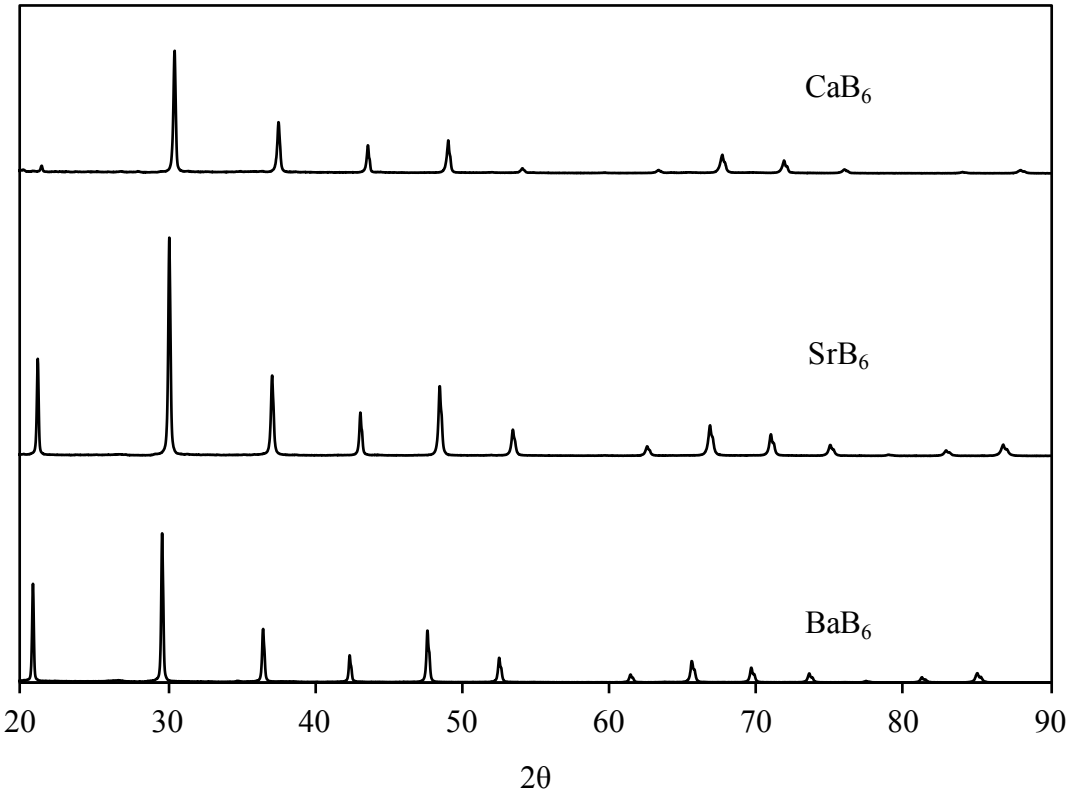

Figure 51 XRD patterns of CaB_6, SrB_6 and BaB_6 powders produced by combustion

Figure 52 shows the X-ray diffraction patterns of the samples with compositions $(Sr_xCa_{1-x})B_6$ produced by both combustion synthesis (Figure 52a) and borothermal reduction (Figure 52b). As expected from previous literature [45], the X-ray diffraction patterns indicate a single solid solution phase. In general, the peak positions shift to lower angle 2θ with increasing Sr content, as expected based on the ionic radii of Sr compared to Ca.

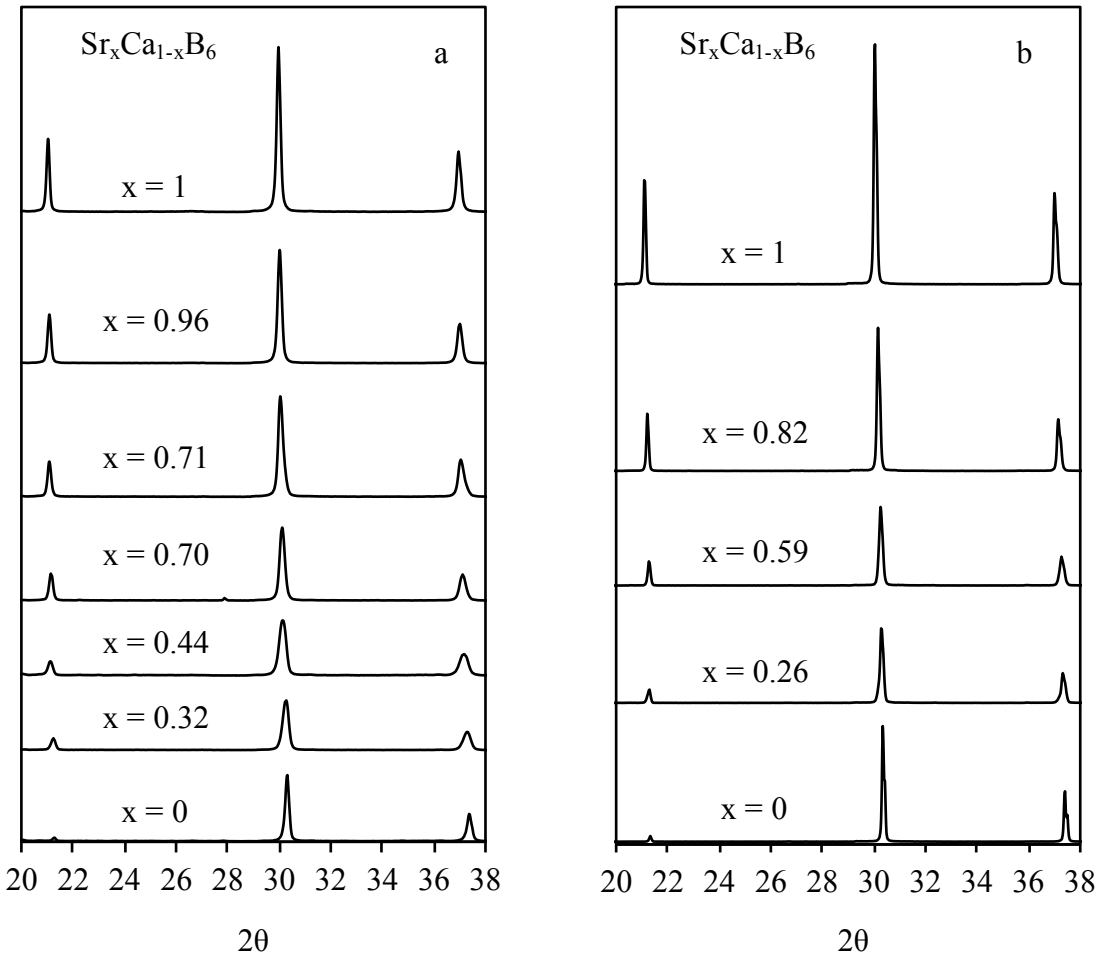

Figure 52 Truncated XRD patterns for the (Sr-Ca)B_6 samples produced by a) combustion and b) reduction where x is atomic % Sr.

The lattice parameters of some of the samples produced in this study deviated from those expected based on Vegard's Law, and in general, the deviation of the combusted samples was greater than those produced by borothermal synthesis. The fraction of [Sr] and [Ca] on the metal-cation site of the materials was determined from the lattice parameters of the end members, assuming adherence to Vegard's law [45], as follows:

$$[Ca]_{solid\ solution} = \frac{a_{solid\ solution} - a_{SrB_6}}{a_{CaB_6} - a_{SrB_6}} \qquad \text{Equation 19}$$

where $a_{solid\ solution}$ is the lattice parameter of the solid solution and a_{CaB_6} and a_{SrB_6} are the lattice parameters of the end members.

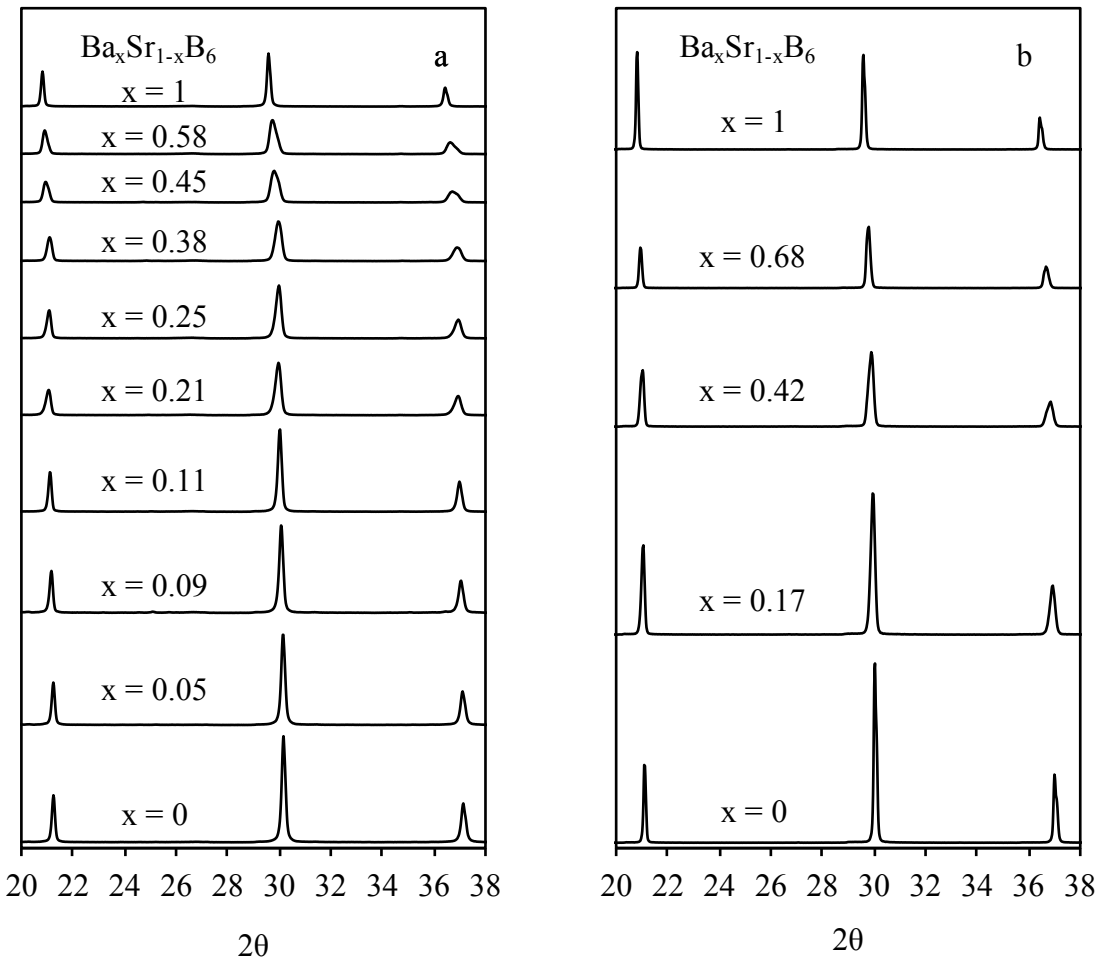

Figure 53 Truncated XRD patterns for the (Ba-Sr)B_6 samples produced by a) combustion and b) reduction where x is atomic % Ba.

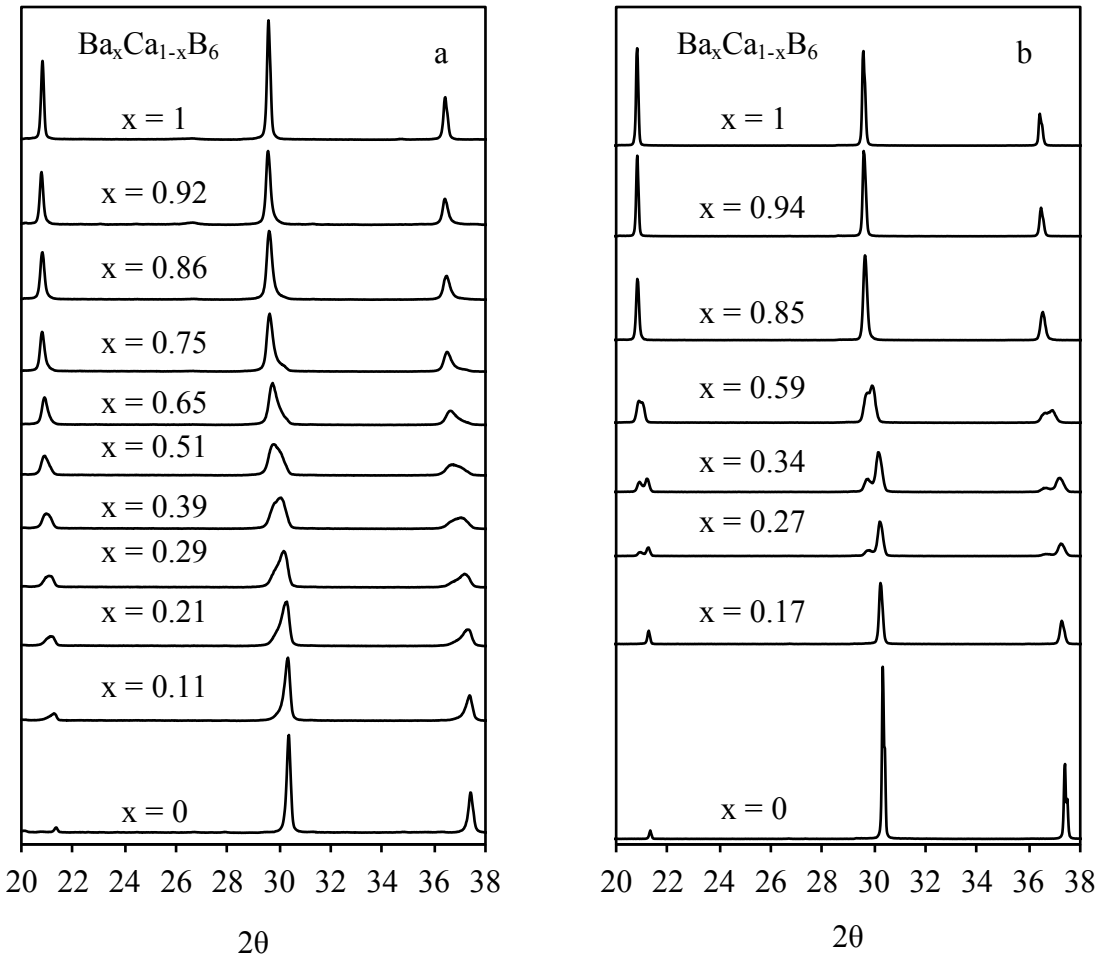

Figure 54 Truncated XRD patterns for the (Ba-Ca)B_6 samples produced by a) combustion and b) reduction where x is atomic % Ba.

Figure 53 and Figure 54 illustrate the XRD patterns for samples prepared with the composition $(Ba_xSr_{1-x})B_6$ and $(Ba_xCa_{1-x})B_6$, respectively. Unlike the SrB_6-CaB_6 system, many of the peaks in the XRD patterns collected from the powders in the BaB_6-SrB_6 and BaB_6-CaB_6 systems appeared broad and asymmetrical. In some of the BaB_6-CaB_6 samples produced by borothermal reduction peak splitting was observed, suggesting the formation of two distinct phases. For powders synthesized by both combustion and reduction, the (Ba-Ca)B_6 samples contained the greatest degree of phase separation as

defined by peak broadening, asymmetry and splitting. Separation was less evident in the Ba-Sr system; however, the powders closer to 50% Ba show some degree of both broadening and asymmetry. These results differ from those obtained by Gürsoy *et al*., who synthesized the same three alkaline-earth hexaborides and reported no signs of XRD peak splitting [45].

All patterns showing peak asymmetry were refined both as two phases (a) and as a single phase (b), as illustrated in Figure 55 for a sample of composition $(Ba_{0.5}Ca_{0.5})B_6$, to determine which method provided a better fit.

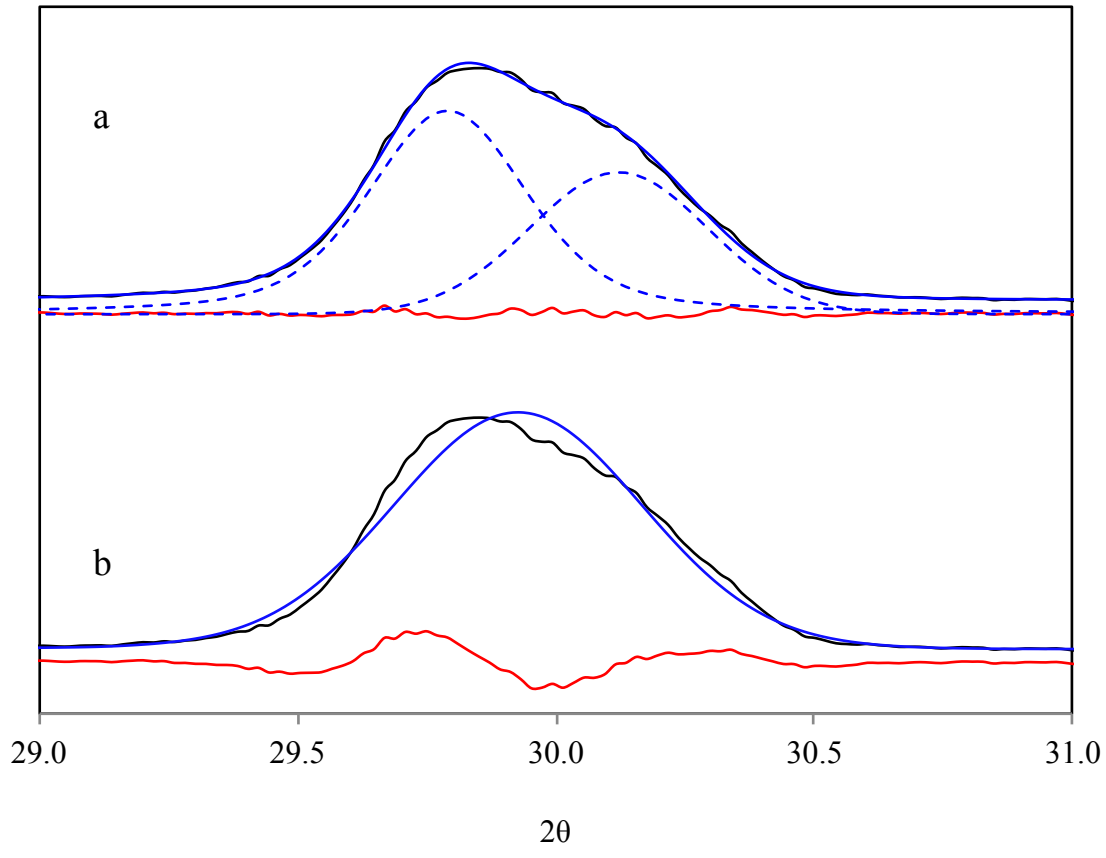

Figure 55 XRD pattern for as-synthesized $(Ba_{0.5}\ Ca_{0.5})Ba_6$ produced by combustion showing a) the blue fit line, dotted blue individual phase lines and red difference line when fitting data with two phases and b) the blue fit line and red difference line when fitting the data with one phase.

In general, refinement of the patterns using two phases produced a better fit to the data, as illustrated by the difference curve (red line) in Figure 55. In the subsequent analysis, all patterns showing asymmetry or splitting were refined using two phases with the same crystal structure, but different lattice parameters. Refinements were first conducted to determine the lattice parameter of both phases. The composition (metal cation ratio) in each phase was then calculated assuming Vegard's Law. The composition of each phase was then fixed in further refinements of lattice parameter and phase fraction, with no constraints on either. The phase fractions determined by TOPAS, along with phase composition determined by Vegard's Law, were then used to calculate an overall sample composition. For the case of Ba:

$$[Ba]_{total} = f1[Ba1] + f2[Ba2] \quad \text{Equation 20}$$

where f1 and f2 are fractions of each phase and [Ba1] and [Ba2] are the Ba content (cation basis) in each phase.

The results of this refinement can be found in Table 8 and Table 9, which include as-prepared and as-synthesized sample compositions, the number of phases for each sample, the lattice parameter of each phase, and the refinement goodness of fit (GOF). Some of this data is represented graphically in Figure 56, which contains the lattice parameters for each sample as a function of cation composition. While there is no phase separation in the $(Sr_xCa_{1-x})B_6$ samples, some of the $(Ba_xSr_{1-x})B_6$ samples display partial separation, and powders of $(Ba_xCa_{1-x})B_6$ display separation at nearly every composition synthesized (excluding the samples with $x = 0$ and 1).

Table 8 Compilation of refinement data from all binary alkaline-earth hexaboride systems produced by combustion and reduction (solid solution phase 1).

	As-prepared total M_1	SS1 frac	Lattice Parameter (Å)	M_1	M_2	microstrain
	Sr			Sr	Ca	
Sr-Ca Combustion	0.00	1.00	4.15553(7)	0.00	1.00	0.1162(52)
	0.20	1.00	4.16967(20)	0.32	0.68	0.166(50)
	0.30	1.00	4.17464(15)	0.44	0.56	0.208(40)
	0.50	1.00	4.186138(81)	0.70	0.30	0.1399(23)
	0.60	1.00	4.186789(68)	0.71	0.29	0.1413(21)
	0.90	1.00	4.197592(76)	0.96	0.04	0.0627(28)
	1.00	1.00	4.199297(49)	1.00	0.00	0.0633(19)
Sr-Ca Reduction	0.00	1.00	4.15371(2)	0.00	1.00	0.02204(56)
	0.25	1.00	4.165317(89)	0.26	0.74	0.0938(15)
	0.50	1.00	4.179582(62)	0.59	0.41	0.1049(10)
	0.75	1.00	4.189715(27)	0.82	0.18	0.04985(56)
	1.00	1.00	4.197624(23)	1.00	0.00	0.04232(47)
	Ba			Ba	Sr	
Ba-Sr Combustion	0.00	1.00	4.199297(49)	0.00	1.00	0.0633(19)
	0.10	1.00	4.202849(48)	0.05	0.95	0.0692(18)
	0.20	1.00	4.205872(62)	0.09	0.91	0.0936(22)
	0.30	1.00	4.207124(49)	0.11	0.89	0.1034(16)
	0.40	0.61	4.20774(21)	0.12	0.88	0.1166(35)
	0.50	0.59	4.20988(24)	0.15	0.85	0.1347(32)
	0.60	0.34	4.21489(47)	0.22	0.78	0.1512(54)
	0.70	0.42	4.21645(32)	0.24	0.76	0.162(58)
	0.80	0.56	4.23086(68)	0.45	0.55	0.2284(79)
	1.00	1.00	4.269803(32)	1.00	0.00	0.0552(12)
Ba-Sr Reduction	0.00	1.00	4.197624(23)	0.00	1.00	0.04232(47)
	0.25	1.00	4.209383(55)	0.17	0.83	0.13983(99)
	0.50	1.00	4.227032(84)	0.42	0.58	0.1786(13)
	0.75	1.00	4.245116(61)	0.68	0.32	0.4095(37)
	1.00	1.00	4.267936(91)	1.00	0.00	0.04780(71)
	Ba			Ba	Ca	
Ba-Ca Combustion	0.00	1.00	4.15553(6)	0.00	1.00	0.0708(23)
	0.10	0.27	4.187493(57)	0.28	0.72	0.283(35)
	0.20	0.33	4.202202(69)	0.41	0.59	0.409(13)
	0.30	0.34	4.214123(42)	0.51	0.49	0.391(10)
	0.40	0.34	4.227277(35)	0.63	0.37	0.364(8)
	0.50	0.46	4.237924(21)	0.72	0.28	0.3053(58)
	0.60	0.56	4.245755(13)	0.79	0.21	0.2301(45)
	0.70	0.52	4.252800(45)	0.85	0.15	0.1767(33)
	0.80	0.66	4.260372(90)	0.92	0.08	0.1369(36)
	0.90	0.60	4.265301(61)	0.96	0.04	0.1044(61)
	1.00	1.00	4.269803(32)	1.00	0.00	0.0552(12)
Ba-Ca Reduction	0.00	1.00	4.15371(2)	0.00	1.00	0.02204(56)
	0.15	1.00	4.173285(68)	0.17	0.83	0.0862(17)
	0.20	0.12	4.23696(24)	0.73	0.27	0.267(15)
	0.25	0.16	4.24233(17)	0.78	0.22	0.2365(84)
	0.50	0.32	4.24473(18)	0.80	0.20	0.1707(49)
	0.75	1.00	4.250965(52)	0.85	0.15	0.1042(13)
	0.87	1.00	4.261164(47)	0.94	0.06	0.0645(11)
	1.00	1.00	4.267936(99)	1.00	0.00	0.04780(71)

Table 9 Compilation of refinement data from all binary alkaline-earth hexaboride systems produced by combustion and reduction (solid solution phase 2) including calculated total M^1 and GOF.

	As-prepared total M^1	SS2 frac	Lattice Parameter (Å)	M^1	M^2	microstrain	Calculated total M^1	GOF
	Sr			Sr	Ca		Sr	
Sr-Ca	0.00	0.00					0.00	2.57
Combustion	0.20	0.00					0.32	3.29
	0.30	0.00					0.44	3.72
	0.50	0.00					0.70	3.44
	0.60	0.00					0.71	1.71
	0.90	0.00					0.96	2.97
	1.00	0.00					1.00	4.04
Sr-Ca	0.00	0.00					0.00	1.7
Reduction	0.25	0.00					0.26	1.98
	0.50	0.00					0.59	1.49
	0.75	0.00					0.82	1.69
	1.00	0.00					1.00	2.26
	Ba			Ba	Sr		Sr	
Ba-Sr	0.00	0.00					0.00	4.04
Combustion	0.10	0.00					0.05	3.6
	0.20	0.00					0.09	3.68
	0.30	0.00					0.11	3.14
	0.40	0.39	4.2246(12)	0.36	0.64	0.17(13)	0.21	2.35
	0.50	0.41	4.22651(97)	0.39	0.61	0.161(11)	0.25	2.52
	0.60	0.66	4.23242(71)	0.47	0.53	0.1942(77)	0.38	2.26
	0.70	0.58	4.24219(23)	0.61	0.39	0.1718(43)	0.45	2.15
	0.80	0.44	4.2517(21)	0.74	0.26	0.1379(63)	0.58	2.24
	1.00	0.00					1.00	2.5
Ba-Sr	0.00	0.00					0.00	2.26
Reduction	0.25	0.00					0.17	1.75
	0.50	0.00					0.42	1.58
	0.75	0.00					0.68	1.33
	1.00	0.00					1.00	1.64
	Ba			Ba	Ca		Ba	
Ba-Ca	0.00	0.00					0.00	2.57
Combustion	0.10	0.73	4.1613124(74)	0.05	0.95	0.1448(29)	0.11	1.92
	0.20	0.67	4.168133(11)	0.11	0.89	0.1986(44)	0.21	1.81
	0.30	0.66	4.1760661(12)	0.18	0.82	0.2365(53)	0.29	1.54
	0.40	0.66	4.185595(26)	0.26	0.74	0.2692(71)	0.39	1.59
	0.50	0.54	4.1938747(37)	0.34	0.66	0.3043(92)	0.51	1.61
	0.60	0.44	4.2083908(85)	0.46	0.54	0.352(16)	0.65	1.71
	0.70	0.48	4.2278207(11)	0.63	0.37	0.431(17)	0.75	1.71
	0.80	0.34	4.2425161(50)	0.76	0.24	0.274(17)	0.86	1.84
	0.90	0.40	4.2546941(63)	0.87	0.13	0.301(18)	0.92	2.39
	1.00	0.00					1.00	2.5
Ba-Ca	0.00	0.00					0.00	1.7
Reduction	0.15	0.00					0.17	1.23
	0.20	0.88	4.17702(12)	0.20	0.80	0.1734(28)	0.27	1.17
	0.25	0.84	4.18321(12)	0.26	0.74	0.2134(30)	0.34	1.22
	0.50	0.68	4.21088(17)	0.50	0.50	0.1966(39)	0.59	1.18
	0.75	0.00					0.85	1.46
	0.87	0.00					0.94	1.57
	1.00	0.00					1.00	1.64

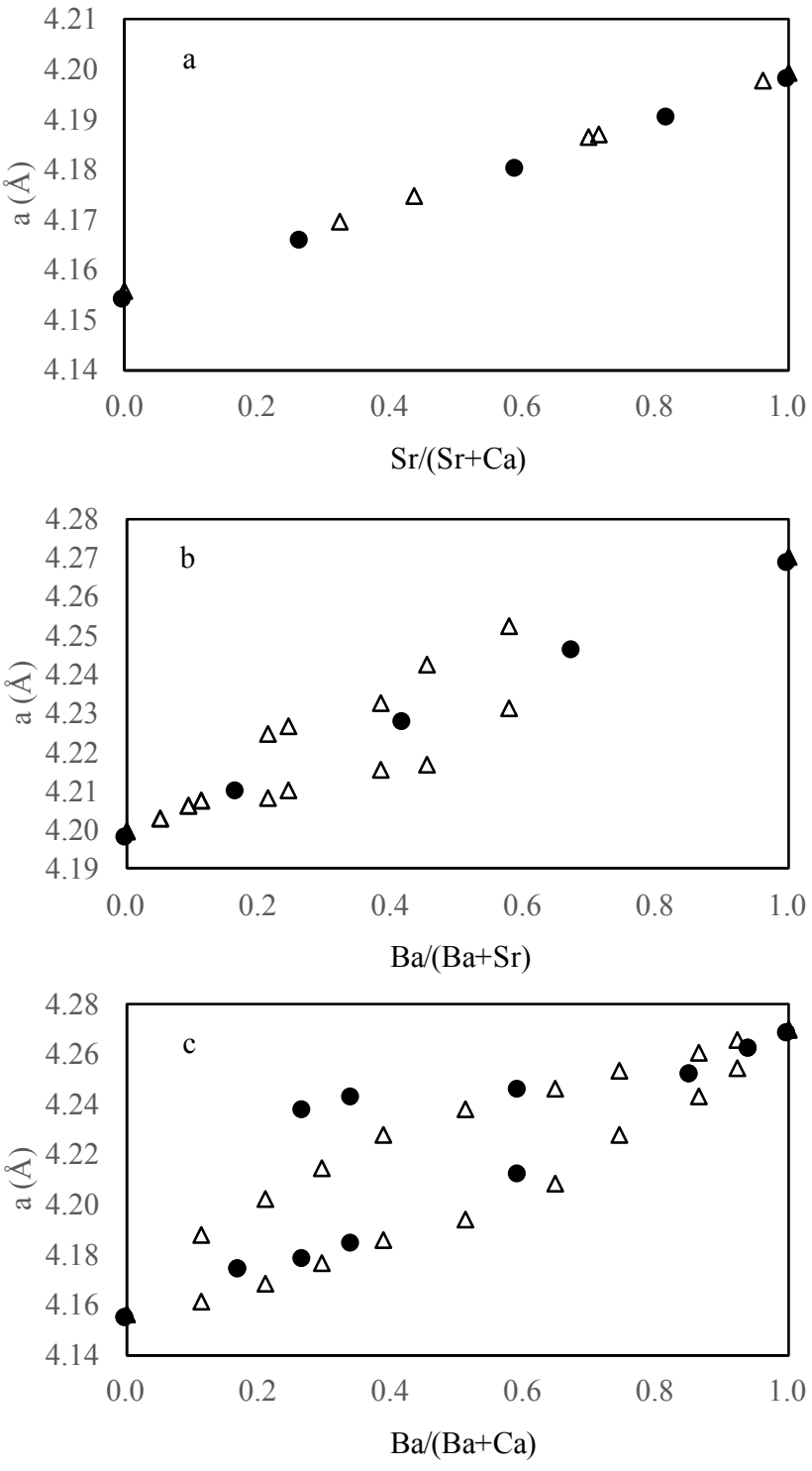

Figure 56 Lattice parameters calculated from TOPAS refinements for a) the (Sr-Ca)B_6 samples, b) the (Ba-Sr)B_6 samples and c) the (Ba-Ca)B_6 samples. Δ represents data from combustion powders and ● represents data from reduction powders.

There are at least two possible reasons for the presence of two phases in BaB_6-SrB_6 and CaB_6-BaB_6. One possible explanation is the presence of an immiscibility gap in the BaB_6-SrB_6 and CaB_6-BaB_6 systems. If this were the case, it should be thermodynamically possible to achieve homogenous, single-phase samples, at higher temperature and stable two-phase mixtures at lower temperatures. Moreover, one might expect evidence of two phases to be most evident in samples with x near 0.5. A second possible explanation is that the samples were not reacted long enough at higher temperature to ensure homogenization. In other words, the two-phase mixture would not be thermodynamically stable and the mixture is simply a kinetic effect. A series of heat treatments were performed on $Ba_xCa_{1-x}B_6$ samples to test the validity of these explanations.

Two different heating methods were used to explore phase stability in the materials (spark plasma sintering and heating in a graphite vacuum furnace). Both methods utilized a low-pressure atmosphere to reduce oxygen contamination. Figure 57 illustrates the XRD patterns collected from heat-treated $(Ba_{0.5}Ca_{0.5})B_6$ powders. Figure 57a and Figure 57b are for the combustion and reduction powders, respectively, heated in the SPS, and Figure 57c is for the combustion powders heated in the high temperature vacuum furnace. For the combustion synthesized samples Figure 57a and Figure 57c, heating to increasingly higher temperatures ultimately resulted in a decrease in the full-width half maximum (FWHM), an increase in symmetry, and an increase in peak intensity. For the reduction samples, the distinct diffraction peaks in the as-synthesized samples appear to merge to a single more symmetric peak at 1973 K. While the sharpening of the peaks could be a result of crystallite growth, the merging of the two

peaks suggests the formation of a uniform solid solution. Heating to higher temperature also resulted in a decrease in microstrain, as seen in Figure 58. While the peaks are sharper in the patterns taken from the SPS heated samples, the trend in both methods is the same, suggesting that the preferred state of mixed-cation hexaborides at high temperatures is a homogenous solid solution.

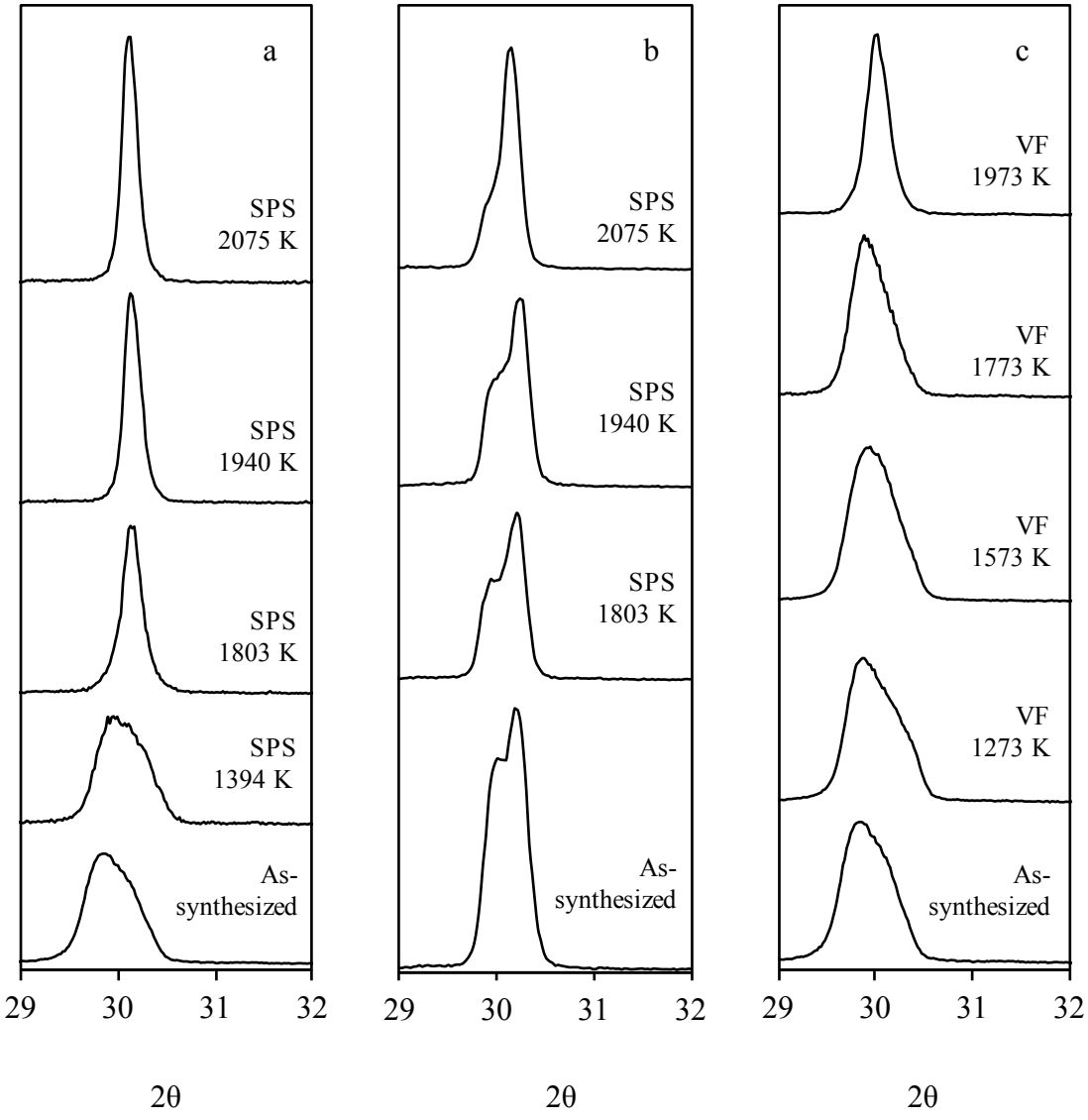

Figure 57 XRD data collected from heat-treated $(Ba_{0.5}Ca_{0.5})B_6$ powders for a) combustion powders in the SPS, b) reduction powders in the SPS and c) combustion powders in the high temperature vacuum furnace.

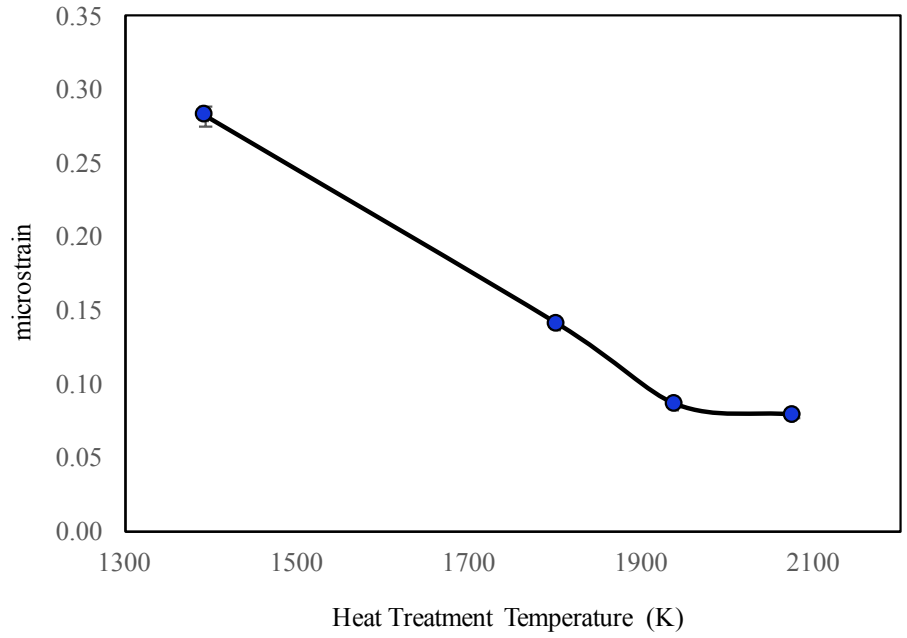

Figure 58 Microstrain values calculated from TOPAS refinement of XRD data from $(Ba_{0.5}Ca_{0.5})B_6$ powders heat treated to various temperatures.

For the combustion synthesis and subsequently spark plasma sintered samples, there does not seem to be any change in the XRD patterns of the powders treated at 1394 K when compared to the as-synthesized samples, leading us to question whether two distinct phases were stable at these temperatures. To test this concept, alkaline-earth hexaboride powders produced by combustion synthesis were heat treated to 1973 K and then cooled down to 1273 K and held for 6 hours in the vacuum furnace. Powder from the same batch was heated to 1940 K in the SPS and then cooled to 1257 K and held for 30 minutes. Figure 59 contains the XRD data collected from these powders in comparison with the as-synthesized powders and the powders heated to 1973 K (vacuum furnace) and 1940 K (SPS), and subsequently cooled directly to room temperature.

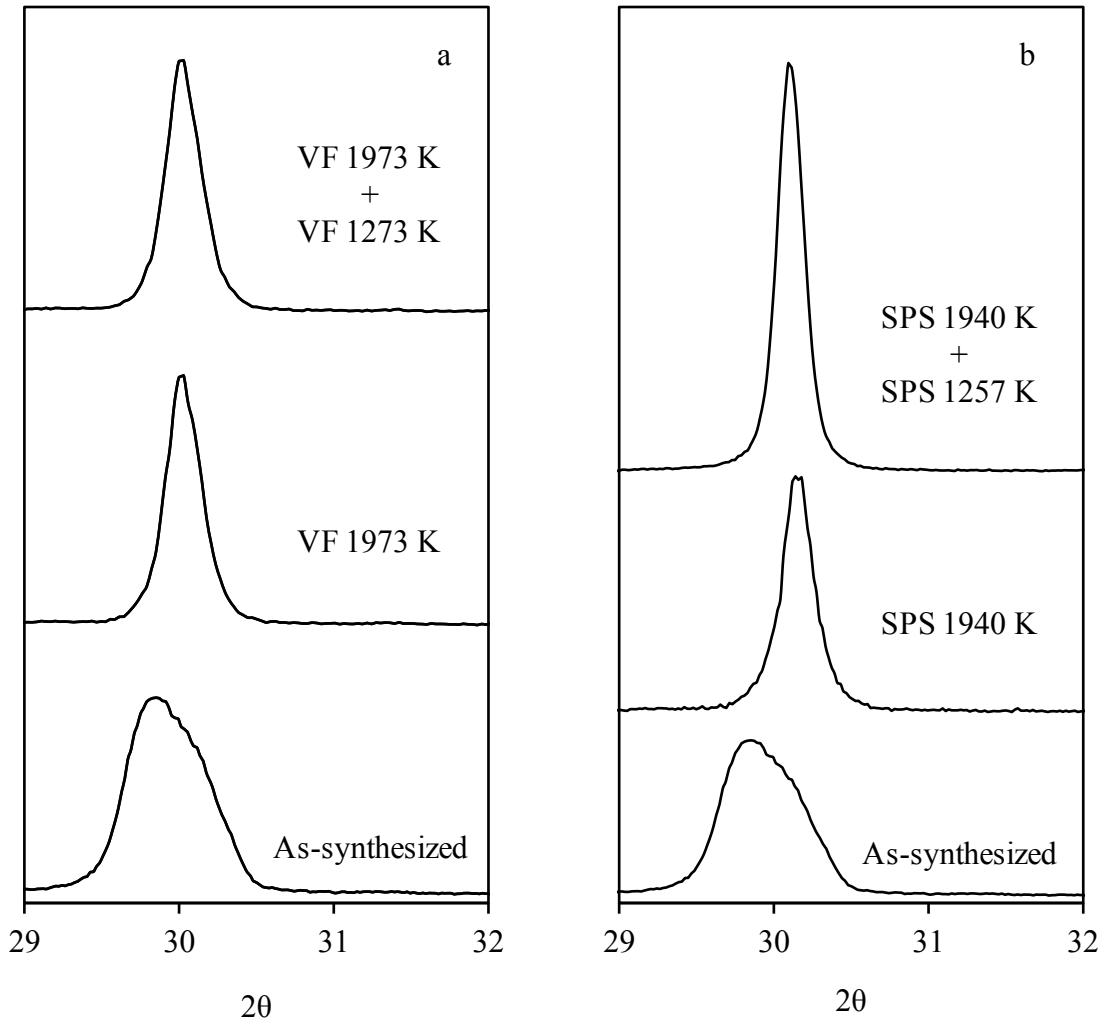

Figure 59 XRD data collected from $(Ba_{0.5}Ca_{0.5})B_6$ powders heat-treated in a) high temperature vacuum furnace and b) the SPS. Both methods utilized a high temperature treatment immediately followed by a lower temperature treatment.

The patterns in Figure 59 show no sign of peak splitting after the secondary 1273 K (vacuum furnace) or 1257 K (SPS) heat treatments and almost no discernable difference between the powders cooled directly from 1973 or 1940 K, confirming that a single solid solution is the preferred state at these temperatures.

Although the data gathered from XRD is useful for examining the bulk powder behavior, it does not reveal specific information about the morphology of the phase

separation seen in the mixed cation alkaline-earth hexaborides. HRTEM allows us to view the structure of crystalline materials as well as determine bond lengths and observe crystallites or dislocations to learn more about the structural behavior of their samples. One sample of $(Ba_xSr_{1-x})B_6$ and one of $(Ba_xCa_{1-x})B_6$, both produced by combustion synthesis, were selected for atomic-resolution TEM analysis to try and observe the phase separation seen in the XRD data. Figure 60, Figure 61 and Figure 62 contain the HTEM images taken from the as-prepared $(Ba_{0.5}Sr_{0.5})B_6$ powder particles, while Figure 63, Figure 64 and Figure 65 are from the as-prepared $(Ba_{0.5}Ca_{0.5})B_6$ powder particles.

Each of the HRTEM micrographs portray some level of inhomogeneity in the crystal structure ranging from lattice misalignment and dislocations to changes in crystallite orientation. Images from the as-prepared $(Ba_{0.5}Sr_{0.5})B_6$ powder contain what appear to be clusters or nano-regimes with various crystal orientations (Figure 60) and lattice misalignment (Figure 61 and Figure 62), while Figure 63 and Figure 64 from the as-prepared $(Ba_{0.5}Ca_{0.5})B_6$ powder depict distinct differences in crystal orientation at both magnifications. The magnified lattices seen in Figure 62 and Figure 65 are more uniform; however, each contain a small degree of misalignment visible in each of the orientations. An as-prepared $(Ba_{0.5}Ca_{0.5})B_6$ lattice shown in Figure 66a appears uniform, but an EDS scan (Figure 66b) reveals the presence of both Ca and Ba cations. The ratio of Ba:Ca as observed by EDS is approximately 73:27, (Ca-Kα, 3.691 keV and Ba-Lα, 4.465 keV) and by using Vegard's law from Equation 19 this equates to a lattice parameter of 0.424 nm.

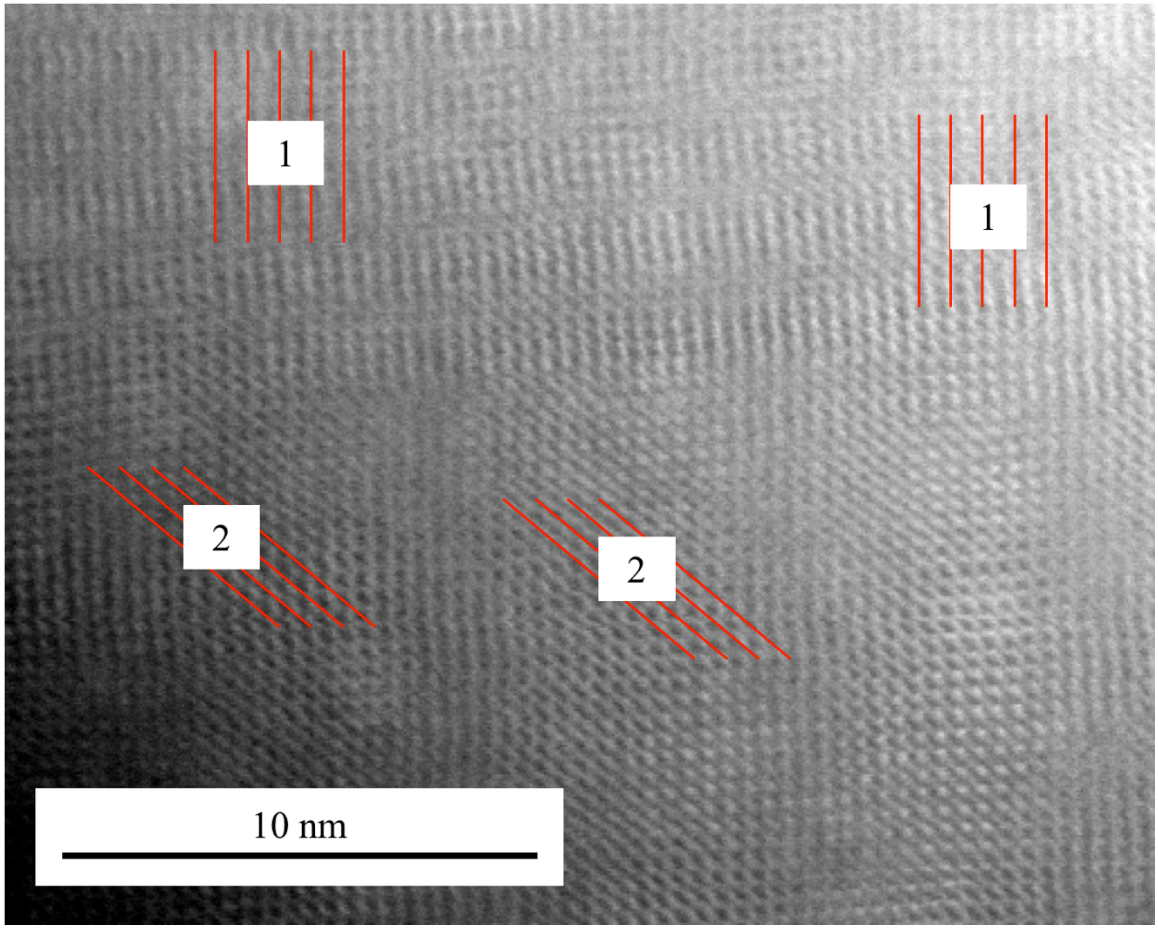

Figure 60 HRTEM micrograph of a $(Ba_{0.5}Sr_{0.5})B_6$ particle displaying two distinct crystallographic orientations (red lines).

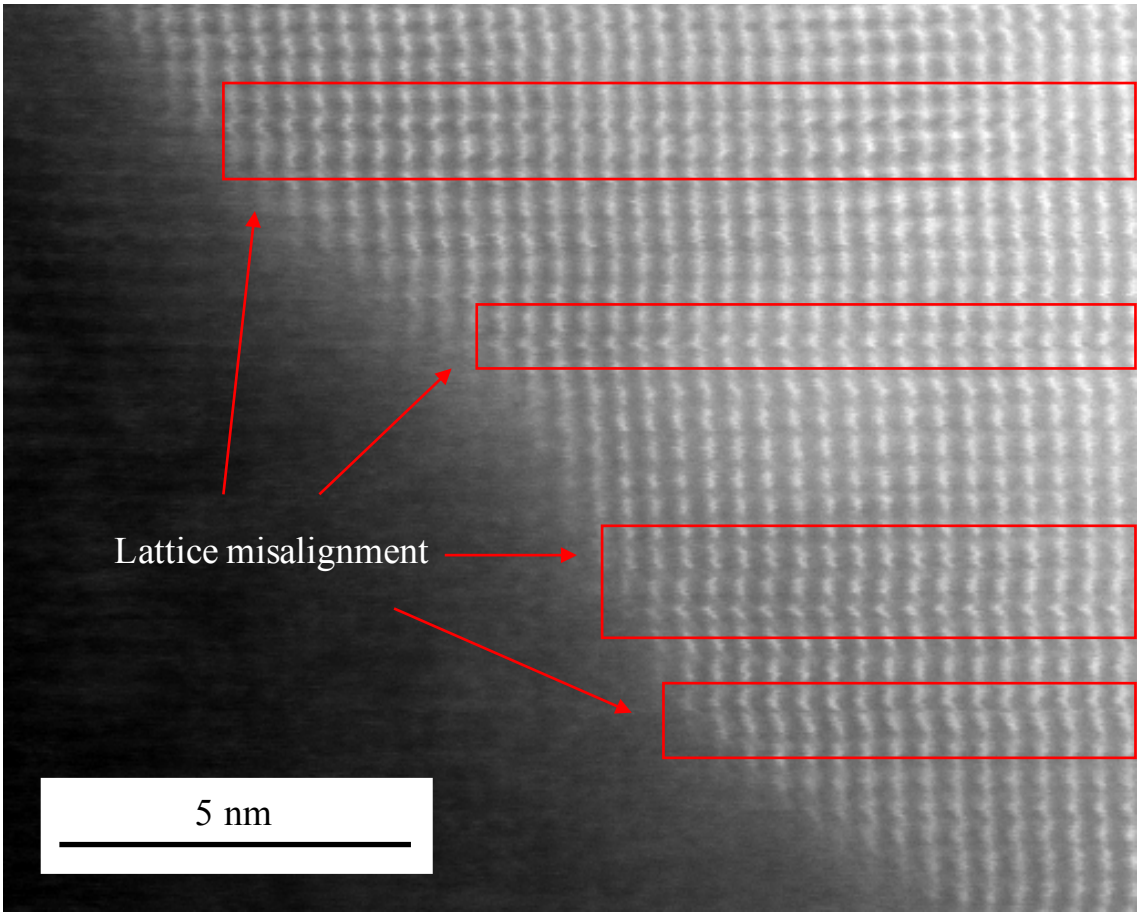

Figure 61 HRTEM micrograph of a $(Ba_{0.5}Sr_{0.5})B_6$ particle with several planes containing lattice misalignment highlighted in red.

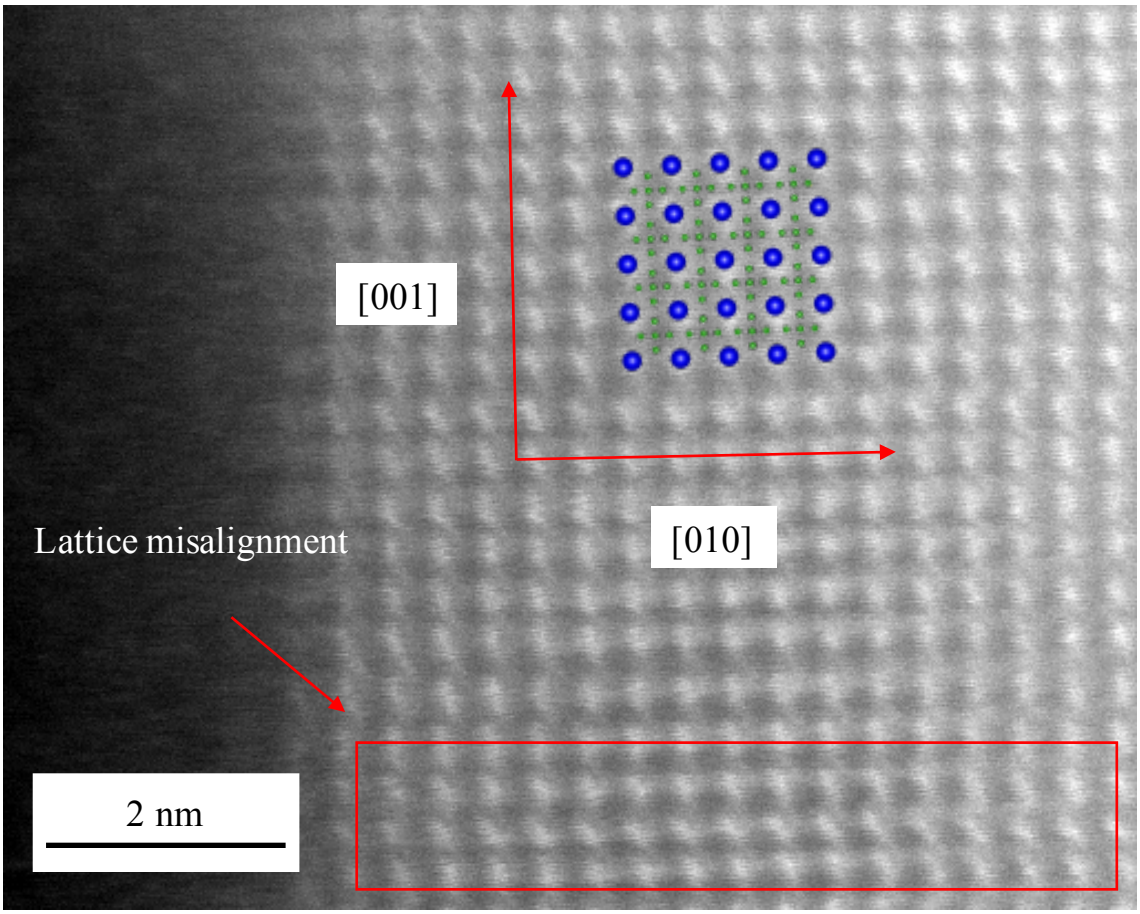

Figure 62 HRTEM micrograph of a $(Ba_{0.5}Sr_{0.5})B_6$ particle containing lattice misalignment (red box). A schematic of the MB_6 crystal structure has been overlaid depicting metal atoms (blue) and boron atoms (green).

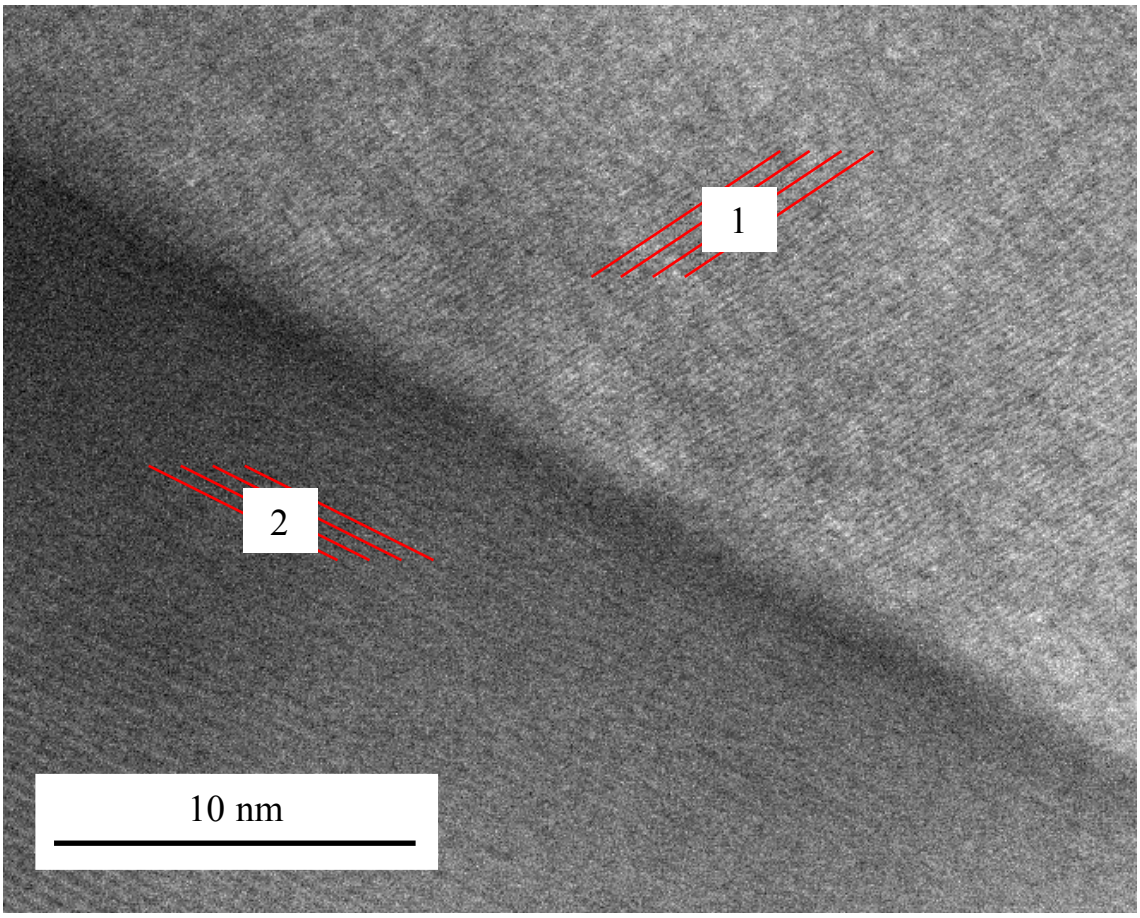

Figure 63 HRTEM micrograph of a $(Ba_{0.5}Ca_{0.5})B_6$ particle displaying two distinct crystallographic orientations (red lines).

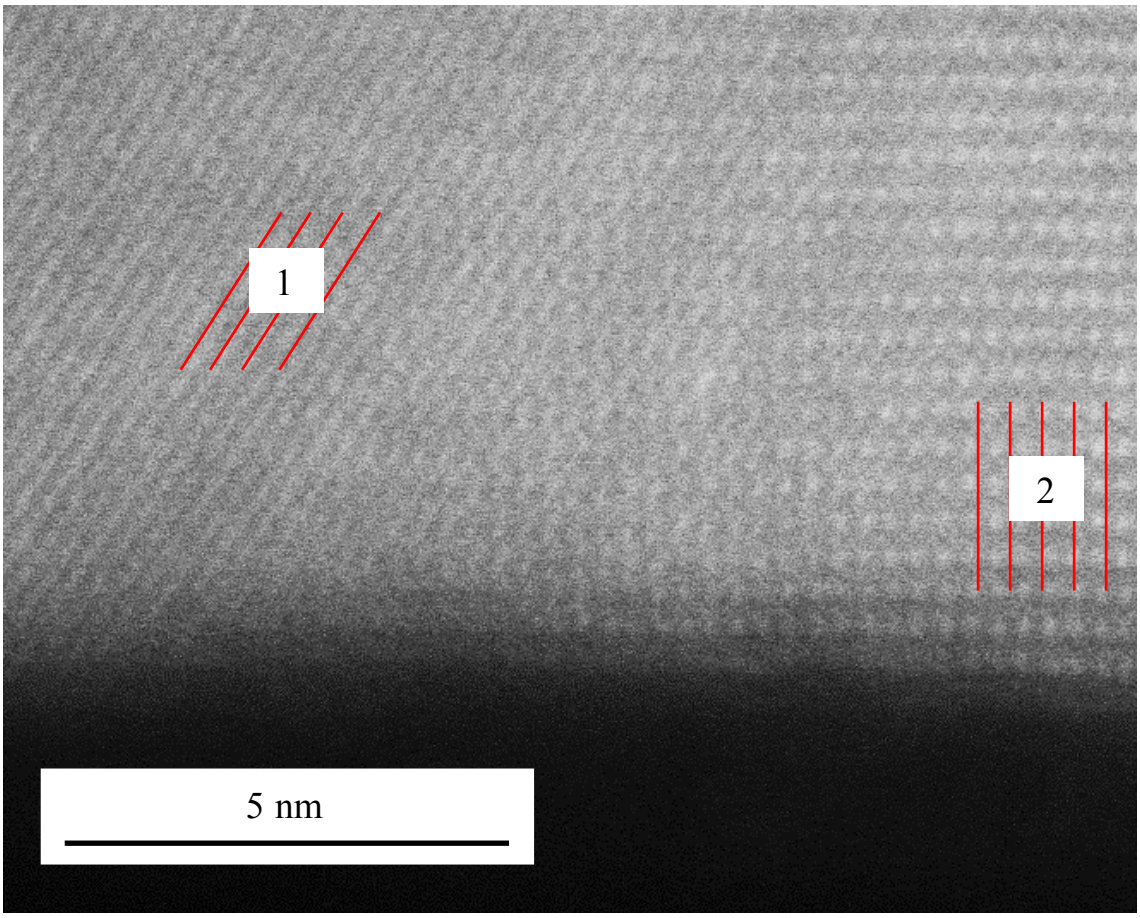

Figure 64 HRTEM micrograph of a $(Ba_{0.5}Ca_{0.5})B_6$ particle displaying two distinct crystallographic orientations (red lines).

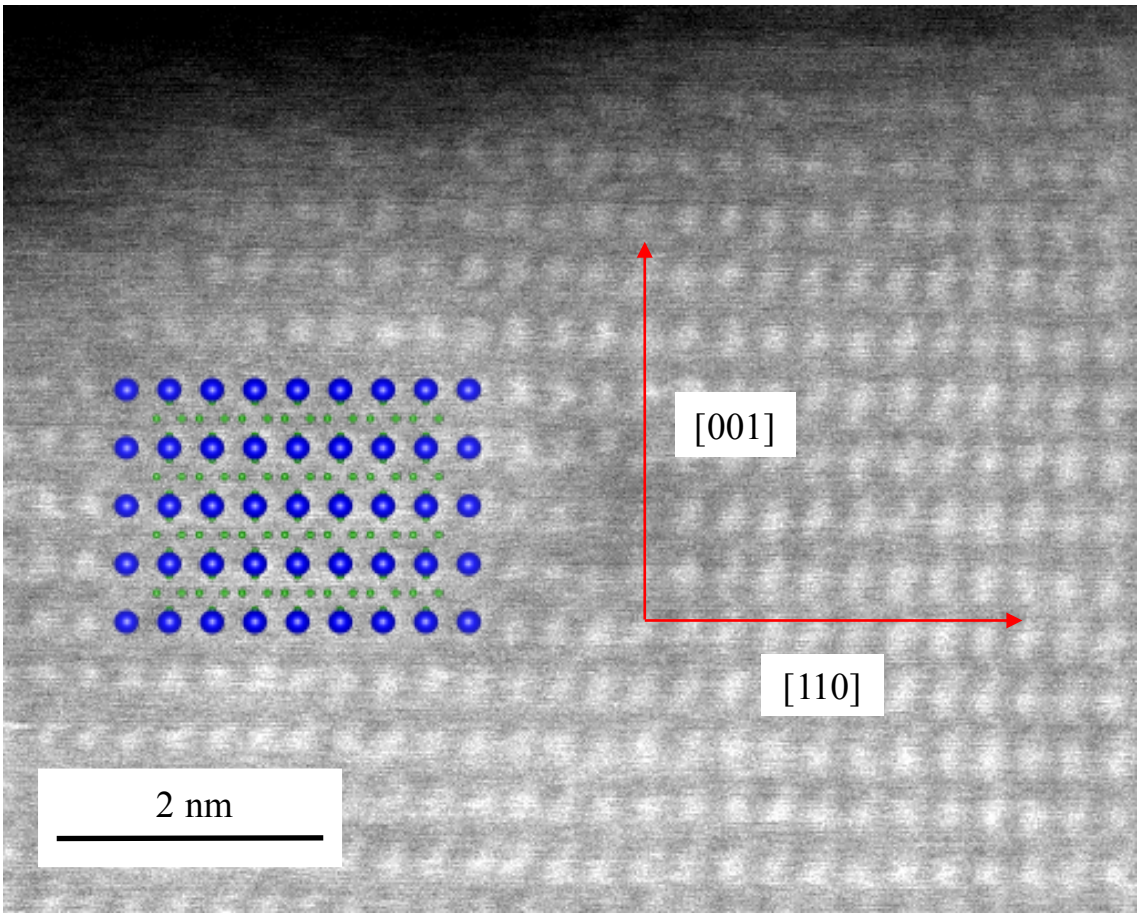

Figure 65 HRTEM micrograph of a $(Ba_{0.5}Ca_{0.5})B_6$ particle with a schematic of the MB_6 crystal structure has been overlaid depicting metal atoms (blue) and boron atoms (green).

A micrograph with high resolution like the one in Figure 66a can also be used to extract structural information with FFT. Figure 66c contains an FFT of the same selected area with the corresponding *d*-spacing values for the {100} and {110} families of planes, which are then used to calculate a lattice parameter. The *d*-spacing value for the {110} family of planes yields a lattice parameter of 0.423 nm while the *d*-spacing value for the {100} family of planes yields a lattice parameter of 0.422 nm. Comparing these values to that obtained from EDS analysis and Vegard's law, results in only 0.3% difference.

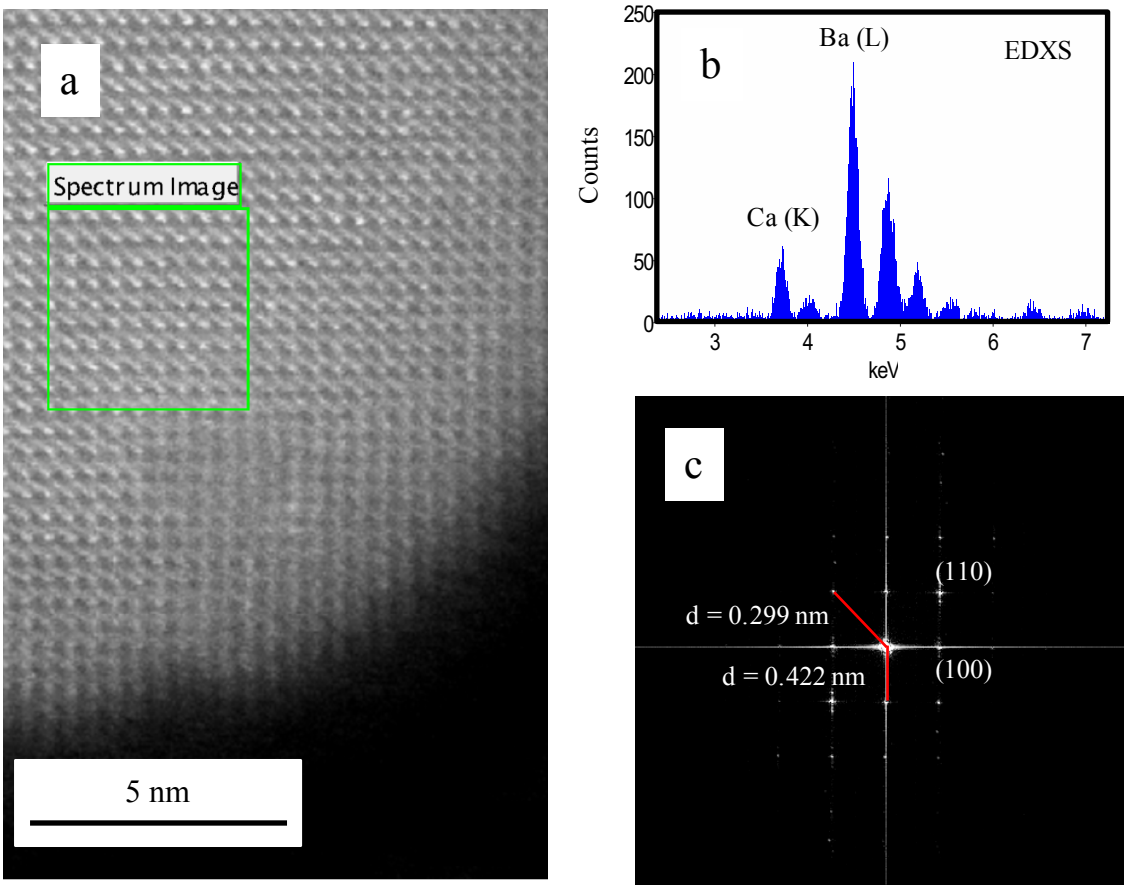

Figure 66 a) HRTEM image of a $(Ba_{0.5}Ca_{0.5})B_6$ particle with the corresponding spectrum area highlighted, b) an EDXS scan of the selected area and c) an FFT of the selected area with d-spacing values.

As seen in both the XRD data and TEM images, several of the alkaline-earth hexaboride ternary compositions display a degree of phase separation or nano-regimes. $(Ba_xCa_{1-x})B_6$ powders produced by combustion synthesis possess two distinct regions with slightly different lattice parameters, and $(Ba_xSr_{1-x})B_6$ compositions near 50% Ba display similar phase separation. $(Ba_xCa_{1-x})B_6$ powders produced by reduction show very distinct phase separation near 50% Ba, but no distinguishable separation in $(Ba_xSr_{1-x})B_6$ samples. Powders produced by both combustion synthesis and reduction demonstrated complete solid solutions for $(Sr_xCa_{1-x})B_6$ samples. The morphology of this separation as

observed in TEM is represented by rounded clusters and crystallites, suggesting a nucleation and growth type behavior. Coupling this idea with the XRD data, showing that the phases merge during heat treatments and do not re-separate at synthesis temperatures, suggests that these nano-regimes are a product of the synthesis method. Although both synthesis methods produce powders with phase separation they each utilize different time scales, heating methods and environments. The metal precursors used in each method are more closely related, nitrates for combustion synthesis and carbonates for the reduction. Both of these metal salt precursors decompose at elevated temperatures (Equation 21 and Equation 22) into metal oxides and gas with thermal stability increasing with cation size as seen in Table 10.

$$M(NO_3)_2(s) \rightarrow MO(s) + 2NO_2(g) + \tfrac{1}{2}O_2(g) \quad \text{(nitrate decomposition)} \quad \text{Equation 21}$$

$$MCO_3(s) \rightarrow MO(s) + CO_2(g) \quad \text{(carbonate decomposition)} \quad \text{Equation 22}$$

Table 10 Enthalpies and decomposition temperatures for alkaline-earth metal nitrates and carbonates

Nitrate	**ΔH (kJ mol^{-1})**	**$T_{decomp, air}$ (K)**
$Ca(NO_3)_2$	+24	834
$Sr(NO_3)_2$	+36	843
$Ba(NO_3)_2$	+42	865
Carbonate	**ΔH (kJ mol^{-1})**	**$T_{decomp, vacuum}$ (K)**
$CaCO_3$	+178	1247
$SrCO_3$	+235	1256
$BaCO_3$	+267	1458

In either case, each synthesis method relies on the ability to separate the M-O bond to promote formation of an M-B bond. Although thermal stability of the alkaline-earth nitrates and carbonates increases with increasing cation size, the cohesion energy (E_a) of alkaline-earth oxides of the MO form follows the opposite trend such that CaO > SrO > BaO [208, 209]. Serebryakova and Marek [30] used borothermal reductions to produce CaB_6 and BaB_6 and noted that the temperature of formation for these two compounds was approximately 1873 K and 1673 K, respectively. They also took into account the electronic structure of alkaline-earth metals, observing that the mobility of electrons due to differences in orbital shell transitions for Ca ($3d^0 4s^2$) and Ba ($5d^0 5f^0 6s^2$) was vital for promoting M-B bonds, therefore affecting the hexaboride temperature of formation, again decreasing as CaB_6 > SrB_6 > BaB_6 [30]. Bao *et al*. also synthesized binary alkaline-earth metal hexaborides using MO precursors and $NaBH_4$ at a lower reaction temperature of 1423 K and demonstrated with XRD the formation of an MB_6 phase at temperatures as low as 1223 K [210]. This supports the idea proposed by Serebryakova and Marek that the strength of the hexaboride bonds and the mobility of electrons promotes the M-B bonding at temperatures significantly lower than the melting point of the MO precursors.

The difference in MB_6 formation temperatures is a non-issue for the synthesis of binary hexaboride compounds as the separation of the M-O bonds happens at relatively the same time and there is no cation diversity to cause lattice parameter variance. During the synthesis of mixed-cation hexaborides utilizing the reduction of metal oxides, $\Delta T_{formation}$ increases while still selectively forming M-B bonds at the temperature where the respective M-O bonds are broken. Selective formation could potentially cause cation-

rich MB_6 regions as the temperature is ramped up during synthesis. This clustering may also be enhanced by the variance in the decomposition temperature of the metal nitrates and metal carbonates used in these experiments. As the greatest degree of variance for both precursor decomposition and MB_6 formation temperatures exists in the BaB_6-CaB_6 system, it is no surprise that the greatest degree of phase separation was observed in those powders. On the opposite end, the SrB_6-CaB_6 system contains the smallest degree of population variance and shows no distinguishable phase separation in the collected XRD patterns. None of the ternary alkaline-earth hexaboride samples produced by Gürsoy *et al*. [45] displayed any phase separation as their synthesis involved the direct reaction of elemental metals with boron and synthesis temperatures above the boiling point of those metals. While the (Sr-Ca)B_6 powders produced by Takeda *et al*. utilized metal oxides, the reported XRD patterns were that of the sintered specimens after an extended period at 2073 K to enhance homogeneity, but even then there is no separation in the (Sr-Ca)B_6 samples [31]. The oxide precursors used by Olsen and Cafiero to produce ternary hexaboride crystals were held at 1773 K for 5 days, more than enough time to allow for homogenization of the metal cations within the hexaboride [76]. The negative deviation from Vegard's law reported in (La-Eu)B_6 samples is curious, and without detailing the peak shape in the XRD patterns it is difficult to know if this is in fact due to compressibility of the EuB_6 or an artifact of peak asymmetry similar to the results of this study.

The phase separation observed in this work is unique due to the combination of synthesis conditions and detailed XRD analysis over a range of temperatures and processes. The uncommonly synthesized ternary hexaborides are rarely characterized by

XRD until after sufficient exposure to temperature, making it easy to miss any potential phase separation. This work illustrates the desired homogeneity easily achievable in ternary hexaborides due to readily diffusing metal cations at elevated temperatures. As the mixing of metal cations in hexaboride compounds is often used to tailor their electrical, thermal, magnetic or optical properties, understanding the formation of these nano-regimes is crucial to the success and control of that optimization.

4.2. Conclusions: Phase Stability of Mixed-Cation Alkaline-Earth Hexaborides

Ternary alkaline-earth hexaborides synthesized by combustion and borothermal reduction contain various levels of phase separation as a result of selective M-O bond separation and M-B bond formation. These phases are present as nano-regimes within the MB_6 crystals, distinguishable by solid solutions with differing M^1:M^2 cation ratios and subsequent MB_6 lattice parameters. XRD data contains peak splitting and asymmetry, signifying the presence of multiple phases with slightly different lattice parameters. HRTEM analysis shows a degree of lattice disorder in (Ba-Ca)B_6 and (Ba-Sr)B_6 particles, complementing the peak separation and high microstrain seen in the XRD data. EDX and FFT analysis of a (Ba-Ca)B_6 lattice reveals a solid solution with higher Ba content than the as-prepared or as-calculated values and is evidence of homogeneity within the nano-regimes. Heating these powders in both the SPS and HT vacuum furnace results in the merger of the separated phases into one solid solution, revealing the thermodynamic instability of the as-synthesized state.

Chapter 4, in part, is being prepared for publication authored by J.T. Cahill, M. Alberga, J. Bahena, C. Pisano, R. Borja-Urby, V.R. Vasquez, S.T. Misture, D. Edwards, and O.A. Graeve. The dissertation author was the primary author of this paper.

5. The Effect of Electric Fields on Diffusion in Alkaline-Earth Hexaborides

5.1. Brief Introduction

The mobility of the metal atom within the rigid boron sublattice presents an opportunity to use these materials to be used as a host for the storage of atoms or ions if transport can be reversibly controlled with an electric field. Increased reactivity in the presence of current in metallic and intermetallic diffusion couples has been attributed to enhanced mobility of defects [211, 212], enhanced product growth rate [212-214] and enhanced nucleation of product phase [212, 214]. Examples of the effect of current on mass transport include the increased dissolution of Ni in liquid Al [215], increased neck growth between copper spheres and plates [216] and increased product phase formation between Sn/Ni [217], Sn/Ag [218], Bi/Ni [219], Al/Ni [214] Al/Au [212], Ag/Zn [213], and Si/Mo [211] diffusion couples. Chen et al. observed enhanced formation of the product phase in Si/Ni couples (Ni_3Sn_4) when the flow of electrons was in the same direction as the diffusion of Sn, but retarded growth in the opposite direction [217]. The same authors reported a similar effect in Sn/Ag couples, noting that the growth of the product phase was enhanced when electrons flowed in the same direction as Sn, but only observed this at lower temperatures (413 K) and not higher temperatures (473 K) [218].

Recent studies have also shown that mass transport is enhanced due to the presence of an electric current in spark plasma sintering (SPS) [188, 196, 220-225]. Diffusion couples produced by Munir and coworkers using SPS show an increase in product phase formation in the presence of current, but no dependence on current flow direction [211, 212]. While the effect of current on diffusion couples is most often studied using metallic systems, the product phase formation in Nb/C couples

sintered by SPS shows that the presence of an electric field affects conductive covalent materials as well [226]. Kondo et al. demonstrated an increased growth rate of Nb_2C and NbC in the presence of current but independent of direction, and also attributed this to enhanced defect mobility. This type of research on covalently-bonded materials can be taken a step further by utilizing hexaboride compounds, which display metallic-like conduction and readily form solid solutions with one another [2, 5, 31, 45]. In this study, we show that the pulsed DC current in the SPS has a direct effect on the diffusion of Ca and Sr atoms across the interface within a CaB_6 and SrB_6 diffusion couple. Diffusion is enhanced towards the positive electrode, and profiles match well with error functions displaying classic Boltzmann-Matano [199, 200] concentration-dependent diffusivity.

5.2. Results and Discussion

Two identical CaB_6-SrB_6 diffusion couples were sintered together with the only difference being the orientation in the SPS (Figure 67). The pulsed DC current in the FCT SPS flows from the upper positive pressing ram to the lower negative pressing ram. Reversing the orientation of the CaB_6 and SrB_6 pellets in the SPS effectively reverses the direction of current flow across the diffusion couple interface. Any difference in voltage drop across the diffusion couple due to orientation is considered negligible based on the relatively similar electrical conductivities of CaB_6 and SrB_6 (where CaB_6 is ~1.5x more conductive than SrB_6) [31]. Cross-sections of these couples reveal the interface and the clearly distinguishable CaB_6 and SrB_6 sides (Figure 68a). Figure 68b and Figure 68c contain EDX maps depicting Ca in blue and Sr in red, respectively. The concentration profiles produced from these types of EDX images can be seen in Figure 69, overlaid with corresponding ERF fits (Ca in blue and Sr in red).

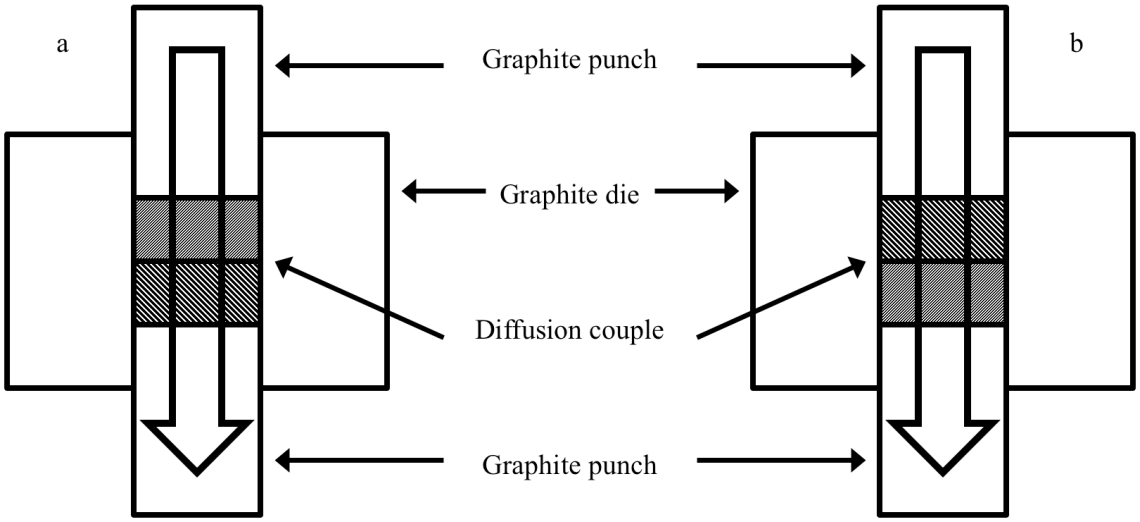

Figure 67 Schematic of the diffusion couple orientation in the SPS showing a) SrB_6 on top and CaB_6 on bottom and b) CaB_6 on top and SrB_6 on bottom. In both cases the current (arrow) flows from top to bottom

Figure 70a and Figure 70b compare the ERF fits of Ca or Sr moving with the flow of current towards negative electrode (dotted lines) and Ca or Sr moving against the flow of current towards positive electrode (solid lines). Table 11 contains the total dopant (*Q)* values for each of the four profiles and the differences between diffusion towards the positive and negative electrodes. Total dopant *Q(t)* is defined by:

$$Q(t) = \int_0^x C(x,t)dx \qquad \text{Equation 23}$$

The profiles in Figure 70 and corresponding Q values from Table 11 reveal that the Ca and Sr atoms diffuse further into the opposing pellet when moving towards the positive electrode. Q is 3.75x greater for Ca and 1.9x greater for Sr when diffusion is towards the positive electrode. This work demonstrates that the metal atoms in alkaline-earth hexaborides are mobile and can be manipulated by the application of an electric field.

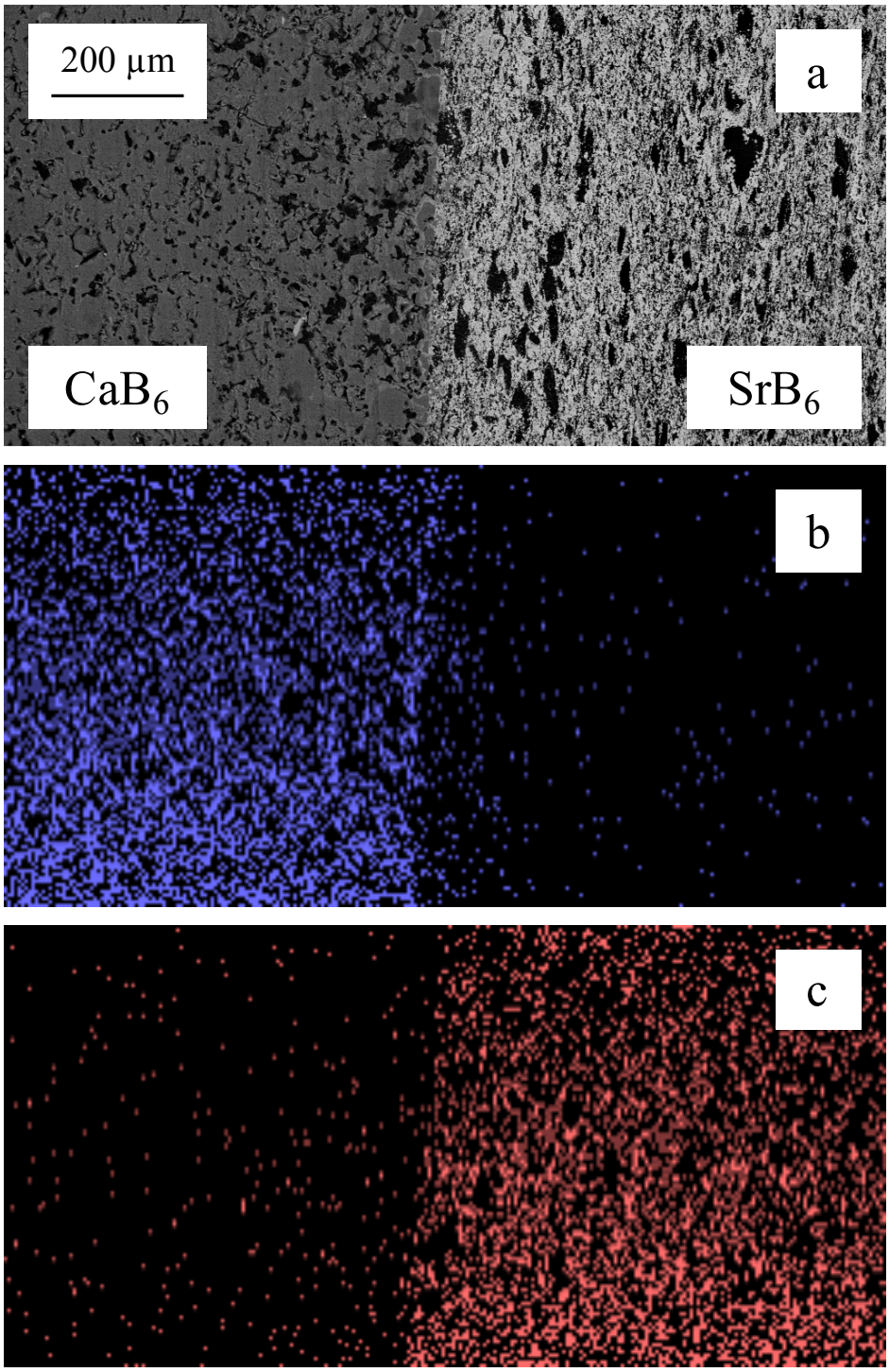

Figure 68 a) Backscattered SEM image of the CaB_6-SrB_6 interface and color-enhanced EDX maps of b) Ca and c) Sr.

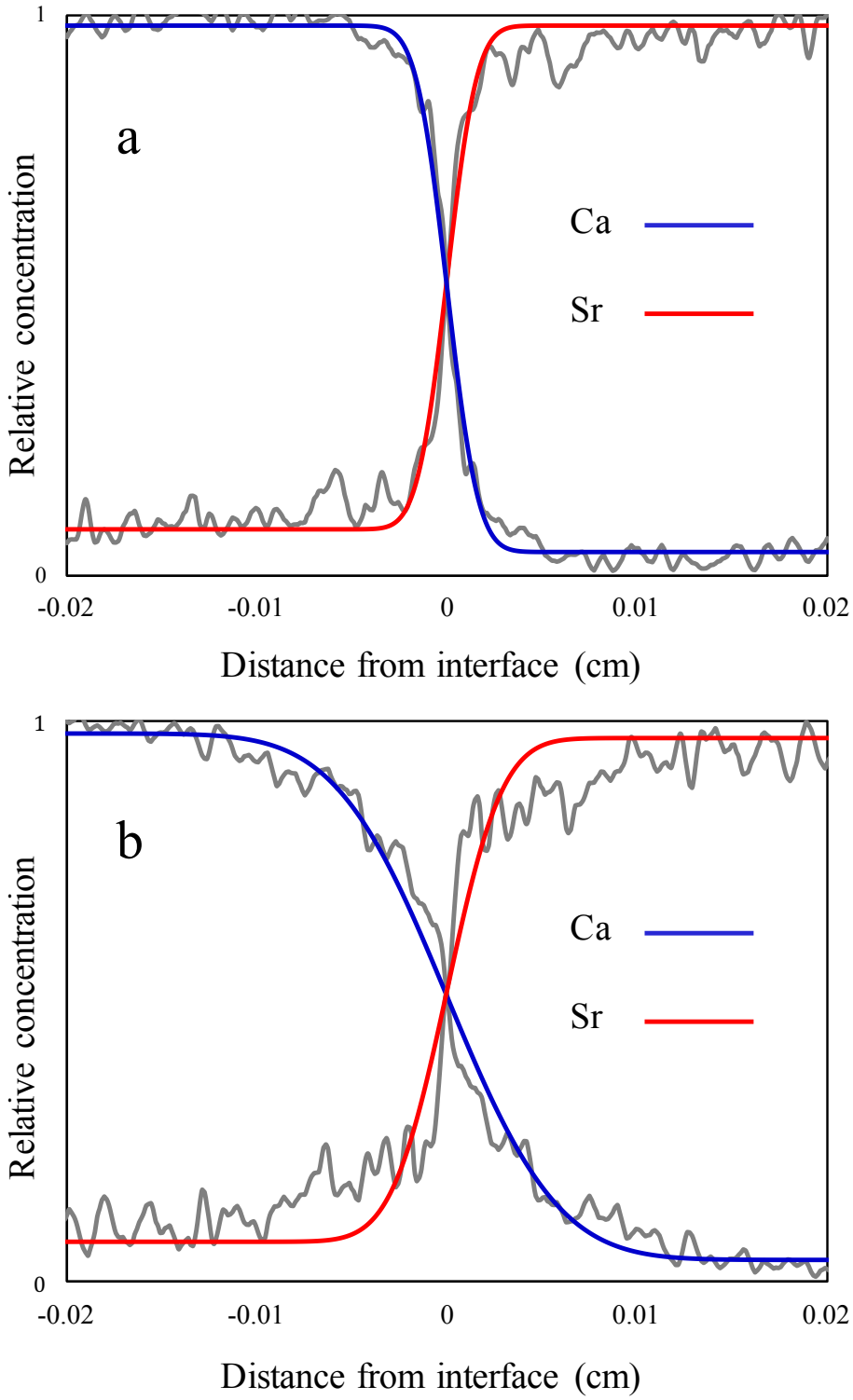

Figure 69 Concentration profiles of Ca in SrB_6 (blue) and Sr in CaB_6 (red) with fitted error functions for diffusion towards a) the negative electrode and b) the positive electrode.

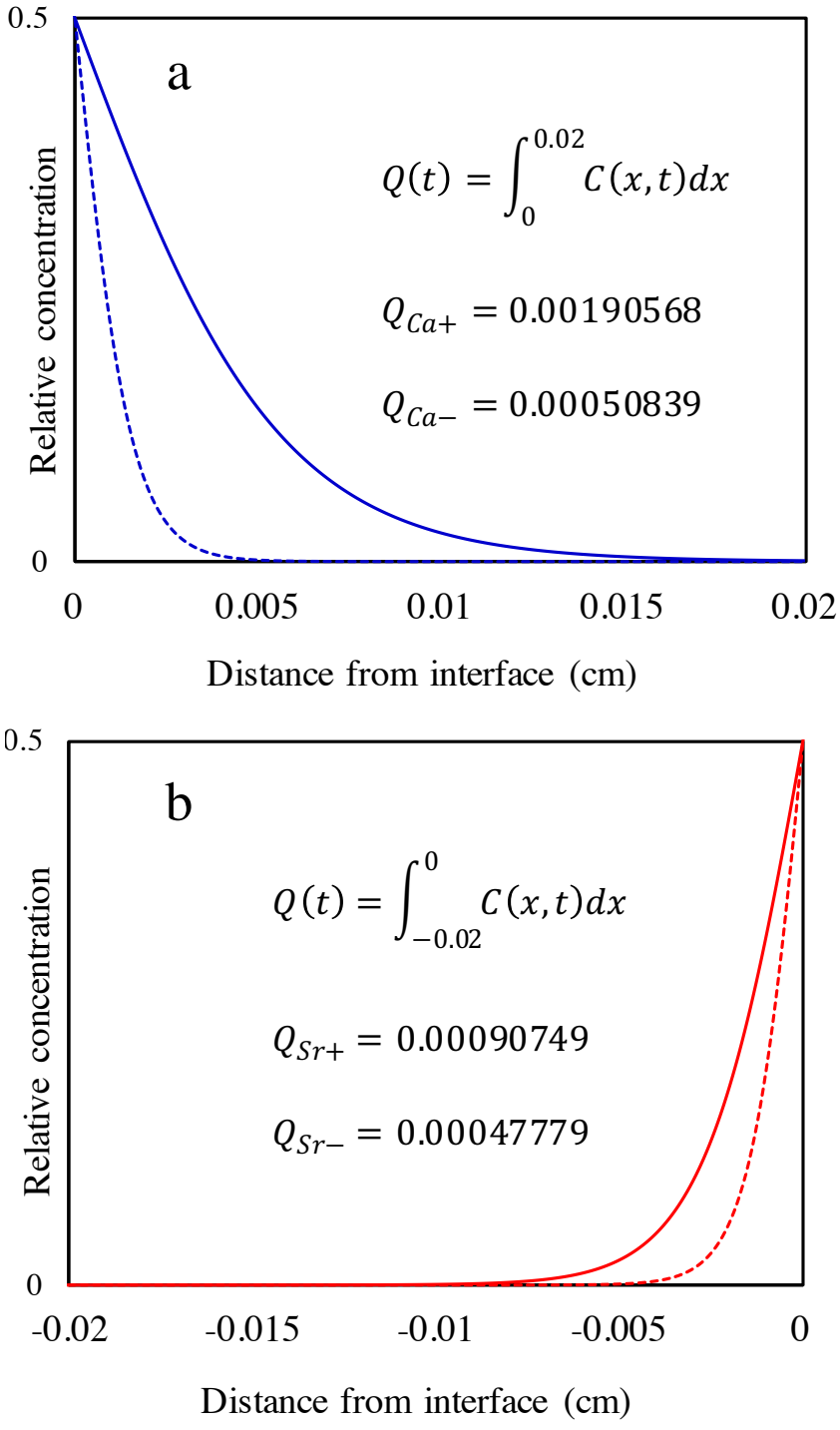

Figure 70 Concentration profiles for a) Ca in SrB_6 towards positive electrode (solid line) and towards negative electrode (dashed line) and b) Sr in CaB_6 towards positive electrode (solid line) and towards negative electrode (dashed line).

Table 11 Total dopant values calculated from integration of concentration profiles for Ca into SrB_6 and Sr into CaB_6 towards positive and negative electrodes. Dopant difference and percent difference act as comparison between the two values.

	Total dopant $\left(10^{-3}/_{cm^2}\right)$	Dopant difference $\left(10^{-3}/_{cm^2}\right)$	Percent difference
Ca into SrB_6 towards positive (+) electrode	1.9057	1.3973	115.76 %
Ca into SrB_6 towards negative (-) electrode	0.5084		
Sr into CaB_6 towards positive (+) electrode	0.9075	0.4297	62.04 %
Sr into CaB_6 towards negative (-) electrode	0.4778		

In many respects, hexaborides can be considered a guest-host structure in which the mobile metal atom is a guest in a rigid boron lattice. This guest-host construct is also common in ionic conductors, however, in these materials the opposite behavior is observed where the ions move towards the oppositely charged electrode. In contrast to ionic conductors, alkaline-earth hexaborides display a metallic-type decrease in conductivity with increasing temperature.

The unusually high conductivity of alkaline-earth hexaborides has been described in terms of both overlapping band gaps and carrier concentration, with the influence of impurities and metal vacancies being quite apparent in experimental results [80]. Although no published data on the self-diffusivity of metal atoms in hexaborides exists, similarities to other cage structures like perovskites suggest that they follow a comparable trend of increasing diffusivity with increasing temperature. With respect to alkaline-earth hexaborides there are several driving forces to consider when discussing mass transport in an environment such as the SPS, and they can be represented visually with respect to

the flow of current (Figure 71). This simplified approach ignores thermal gradients within the SPS die and the effects of pressure and strain on diffusion.

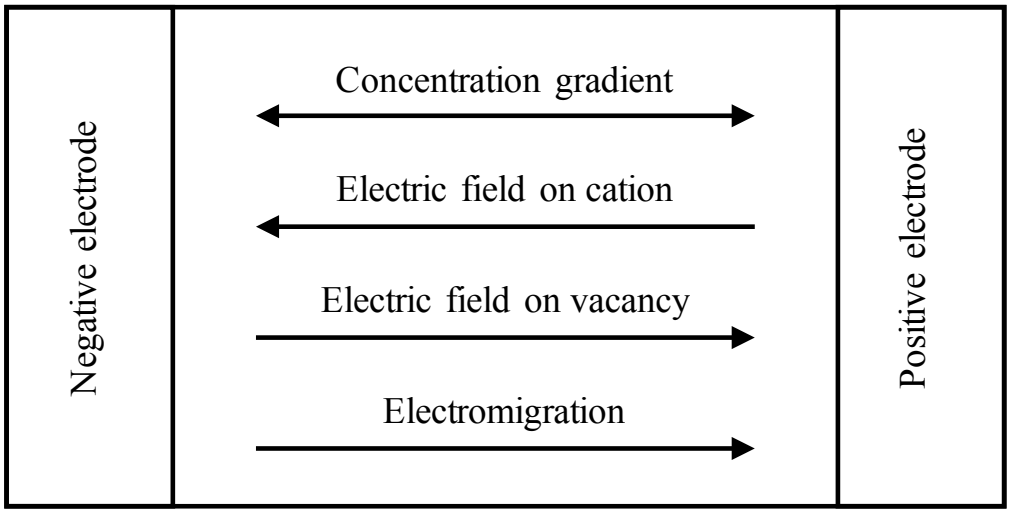

Figure 71 Driving forces for mass transport under the influence of an electric field

Without the influence of the electric field, one would expect to see diffusion of both Ca and Sr atoms across the interface similar to any solid-solution forming diffusion couple. If we assume that Ca and Sr donate two electrons to the boron sublattice then the effective charge of the metal atoms is 2+ while the charge of a metal atom vacancy is 2-. The presence of an electric field now has an effect on these charged species, where once would expect them to move towards the opposite charged electrode (ionic conduction). In conductive materials subjected to high current densities (10^3-10^5 A/cm^2), the effect of flowing electrons may also be considered a driving force for diffusion where the flux for species J_i can then be described by [227]:

$$J_i = D_i \frac{X_i}{RT}\left[RT\frac{\partial \ln X_i}{\partial x} + Fz_iE\right] \quad \text{Equation 24}$$

where D_i is the diffusion coefficient of the ith species, X_i is its concentration, F is Faraday's constant, E is the field, R is the gas constant, T is the absolute temperature, z_i is

the effective charge on the *i*th species and *x* is the direction of diffusion. The *RT* term represents the effect of the concentration gradient while the Fz_iE term represents the effect of electromigration. Considering the maximum possible current density (~800 A/cm^2) and high temperatures (2007 K) used in this research it would not be surprising to see the *RT* term dominate given the $I(T^{-1})$ dependence of the Fz_iE electromigration term. Indeed, Rudinsky et al. calculated an electromigration drift velocity (v_{em}) in Cu/Ni diffusion couples of 2.75x10^{-21} m/s when using a current density of 300 A/cm^2 at 1273 K in the SPS while Blech et al. measured v_{em} = 2x10^{-11} m/s for Cu diffusion through Al under 10^5 A/cm^2 at 528 K [228, 229]. While the effect of electromigration cannot be ruled out, the conditions utilized in this research are not where this phenomenon is typically observed.

Hexaborides, especially the alkaline-earth compounds, are known to be exceptionally sensitive to vacancies and impurities [124]. Mobile charge carries in CaB_6 are thought to be the result of self-doping by vacancies [125], with charge carrier concentrations estimated between 10^{25}-10^{26} per m^3 as calculated from Hall coefficient measurements [31]. The electric fields present in the SPS have been shown to have an effect on the flux of vacancies, as shown in Equation 25 from Olevsky and Froyen [230]:

$$divJ_{vac} = -D\frac{\kappa_T}{\lambda_{T(T)}}\left(C\frac{\partial T}{\partial t} - \lambda_e E^2\right) \quad \text{Equation 25}$$

where *divJ* is the divergence vacancy flux, *D* is the diffusion coefficient, κ_T is the thermal diffusion ratio, λ_T is the thermal conductivity, *C* is the heat capacity, λ_e is the specific electric conductivity and *E* is the electric field. The authors concluded that for conductive materials and moderate values of *E* (e.g. 50 V/m), the $\lambda_e E^2$ term will exceed

the $C^{dT}/_{dt}$ term by several orders of magnitude due to high electric conductivity [230]. In a study on oxygen diffusion in perovskite oxide films, Nian et al. found that ±5 V pulses across the thin films resulted in the reversible movement of oxygen vacancies and resulted in vacancy pileup at the metal electrode interface region [231].

One plausible explanation for the increased diffusion of Ca and Sr atoms towards the positive electrode is that the negatively charged metal vacancies move towards the positive electrode and therefore increase the likelihood of atomic diffusion into those vacant lattice sites in that direction. An important consideration is that the 500 nm particle size of the CaB_6 and SrB_6 powders used to produce the diffusion couples results in sintered specimens with a high volume fraction of grain boundaries. Increased disorder due to vacancies migration into the grain boundaries would result in enhanced diffusion of the grain boundary species. The schematic in Figure 72 depicts enhanced diffusion along grain boundaries towards the positive electrode as vacancies pulled in the same direction through the lattice terminate in the grain boundaries and cause increased disorder and vacant locations for diffusing species. Considering the strong covalent nature of the boron sublattice it is most likely the metal atoms diffusing via grain boundary pathways. As seen in Table 11 and Figure 70, total dopant values for Ca show a greater percent difference than Sr (116% vs 62%, respectively) depending on current flow direction, which may be interpreted as either the Ca atoms diffuse through SrB_6 easier than Sr through CaB_6 or that the current flow has less effect on diffusing Sr atoms.

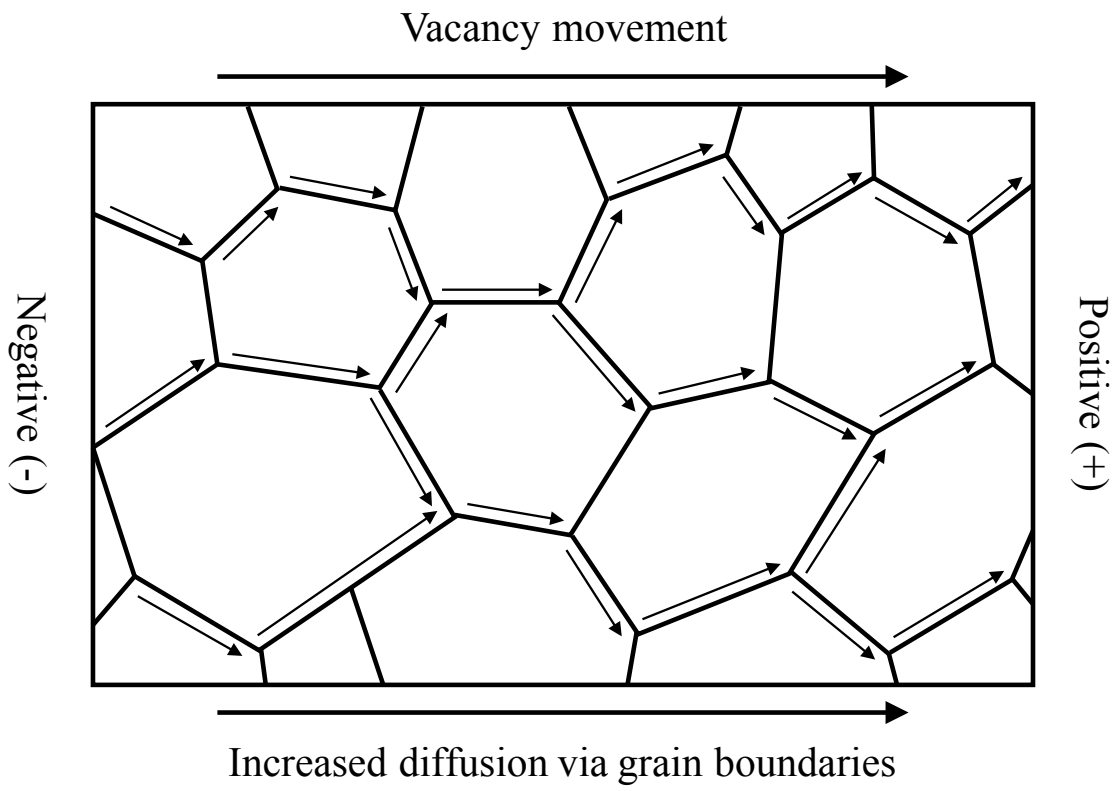

Figure 72 Schematic depicting the flow of metal atoms along grain boundaries due to increased concentration of vacancies in the direction of the positive electrode.

The former may be explained by the smaller size of the Ca ions (0.099 nm) relative to the Sr ions (0.113 nm) [Dickinson], which means that Ca requires less energy to move through the boron framework in the larger lattice of SrB_6 (0.419 nm), while Sr requires more energy to move through the smaller lattice of CaB_6 (0.415 nm). The latter may be due to differences in the activation energies of Ca and Sr under the influence of an electric field; a topic that surely requires further investigation. This work provides a glimpse into the effect of an electric field on the diffusion of alkaline-earth metal atoms within hexaboride compounds and demonstrates that the effect of current flow direction is measureable in CaB_6-SrB_6 diffusion couples.

5.3. Conclusions: Effect of Electric Field on Diffusion in Hexaborides

The pulsed DC current used in spark plasma sintering of CaB_6-SrB_6 diffusion couples was shown to have a direct effect on the movement of Ca and Sr atoms. The enhanced mobility of these atoms across the interface opposite the flow of current is attributed to the movement of negatively charged metal vacancies towards the positive electrode that subsequently terminate in grain boundaries and thereby increase grain boundary diffusion in the same direction. Concentration profiles of Sr and Ca in opposing CaB_6 and SrB_6 pellets match well with error function fits, indicating concentration dependent diffusivity. Total dopant values calculated from the integration of these diffusion profiles reveal a 116% increase for Ca in SrB_6 and 62% increase for Sr in CaB_6 when diffusion occurs towards the positive electrode. Although the current densities applied in the SPS are less than typical electromigration levels, the effect cannot be discount and warrants further investigation to fully understand the complete picture of mass transport in these materials.

Chapter 5, in part, is being prepared for publication authored by J.T. Cahill, V.R. Vasquez, S.T. Misture, D. Edwards, and O.A. Graeve. The dissertation author was the primary investigator and author of this paper.

6. Conclusions

The study of uncommon materials presents a new set of challenges to the interested researcher - namely the task of breaking trail if no previous work exists to guide them. While hexaborides are not the rarest of compounds, they are by no means widely studied. The success of LaB_6 and CeB_6 as electron emitters is the only real example of commercial use for this group of materials, and while other opportunities have been explored they are still very much in the research stage. This relative lack of published material demands creativity and imagination when creating and executing a proposed research plan, which can be both exciting and frustrating. Although the interaction between hydrogen gas and hexaboride compounds has yet to be studied, key steps in understanding the behavior of these candidate materials have been taken. The following is a summary of all the work completed in this dissertation following the order in which the chapters were presented.

Combustion synthesis is a relatively new production technique (< 60 years) that has been gaining popularity for the production of ceramic and intermetallic materials due to its low cost and efficient nature. The subcategory utilized in this research was solution combustion synthesis (SCS), which most commonly involves the reaction of metal nitrates and organic fuel in the presence of mild heat (~700 K). Due to the presence of oxygen in the precursors and ambient air, this process lends itself well to the production of oxide ceramics. The work by Kanakala et al. is the first published example of SCS being used for the production of hexaboride compounds to the best of our knowledge [110, 111]. Using this work as a starting point, we demonstrated the first instance of the alkaline-earth hexaborides CaB_6, SrB_6 and BaB_6 produced by SCS through the use of

metal nitrates, amorphous boron and carbohydrazide. These reactions required special attention as they proved to be highly intense and exothermic – a feature later discovered to be necessary in order to promote the formation of borides over oxides. By developing a custom furnace and corresponding combustion method in-house we were able to increase the powder yield and purity while maintaining a higher degree of safety and efficiency. Although at first glance this approach seems expensive and difficult to reproduce, the concept is simple and the materials widely available at a reasonably low price. By this method we were able to produce hexaboride powders grams at a time with cubic particles ranging in size from 200 to 800 nm. Any oxide impurity phases coating the particles were easily removed with a 10-minute wash in concentrated HCl. Once the fuel-to-oxidizer ratios for the three binary compounds (CaB_6, SrB_6 and BaB_6) were established, the formulation for the production of ternary compounds was easily established by weighted averages, and we have no reason to believe it would not be the same for the quaternary compounds.

The consolidation of hexaboride compounds faces the same challenges as the synthesis due to two main factors: high melting temperatures and undesired oxidation. A high melting temperature often corresponds to a high sintering temperature and increased level of thermal energy required to initiate mass transport and diffusion. Hexaborides are also not immune to oxidation, which is increased at high temperatures from both internal and external oxygen sources. The electric current used in spark plasma sintering (SPS) has been shown to increase mass transport and effectively lower the sintering temperature and reduce the sintering time for a multitude of refractory materials. The work of Takeda and coworkers [5, 31, 33, 45, 127] as well as unpublished research by the author's

coworkers demonstrated that this phenomenon was applicable to hexaboride compounds as well. Using this information, powders of CaB_6 and SrB_6 were sintered at 1753 K (T_m = 2508 K) and 1768 K (T_m = 2508 K), respectively. Using the formula from Kelly and Graeve (Equation 6) we can approximate the inner temperature of the die to be 2048 K for CaB_6 and 2069 K for SrB_6; approximately 82% of the melting temperature. The most interesting feature of sintering hexaboride powders produced by combustion was the presence of two sintering events – the first around 64% T_m and the second around 80% T_m. The first sintering event was marked by solidification of the powder and necking between the particles to produce specimens of approximately 90% relative density. The second sintering event saw increased grain growth and the final 8-9% of densification to produce specimens of approximately 99% relative density. The distinction between these two sintering events became important for the production of diffusion couples, where it was discovered that the ease of polishing samples sintered to 90% relative density made the formation of a high-contact and two-dimensional interface possible. High-quality diffusion couples were prepared in this manner by pre-sintering individual CaB_6 and SrB_6 samples and then re-sintering them together in the SPS.

Detailed X-ray diffraction (XRD) analysis of mixed-cation hexaboride powders revealed that they were not composed of a single solid solution phase as intended. This was determined by examining asymmetry and broadening of the peaks in the XRD data, and noting that some peaks began to actually split. The peak splitting is attributed to the existence of multiple solid solutions with varying compositions, present in the samples as nano-regimes within the particles. High-resolution transmission electron microscopy (HRTEM) reveals the presence of lattice misalignment and alternate crystal orientations

within mixed-cation hexaboride particles. The phenomenon of XRD peak splitting was also present in the diffraction patterns of powders produced by borothermal reduction of metal oxides, and in the case of the (Ba-Ca)B_6 samples was even more pronounced. The thermal stability of these separated phases was studied by heat treating $Ba_{0.5}Ca_{0.5}B_6$ powders (which exhibited peak splitting in both combustion and reduction powders) in a high-vacuum graphite furnace and the SPS. Increasing heat treatment temperature corresponded with the sharpening and merging of separated peaks in all samples, indicating that a single solid solution is the preferred state at high temperatures. $Ba_{0.5}Ca_{0.5}B_6$ samples were also heat treated to 1973 K and then cooled and held at 1273 K before being returned to room temperature. The XRD peaks in the data gathered from these samples did not remain split or re-split upon cooling, suggesting that the singular solid solution phase is stable over a wide range of temperatures and that the separated phases are metastable. The source of these nano-regimes can be traced back to the synthesis methods used to produce the powders. Both the combustion and reduction processes utilize precursors that contain M-O bonds at some point in the synthesis. The thermal energy required to break this bond is different for Ca-O, Sr-O and Ba-O, and as the heating process proceeds for each method these bonds are selectively broken and the metal atoms form borides. The increase in phase separation seen in the powders produced by reduction is attributed to the slow heating rate (15 K/min) used in that method, which gives the M-O precursors more time selectively from borides compared to the fast heating rate of combustion (1000 K/s).

Diffusion couples produced in the SPS were used to study the movement metal atoms under the influence of temperature and an electric field. Two diffusion couples of

CaB_6-SrB_6 were sintered at 1723 K with either a) current passing from CaB_6 to SrB_6 or b) current passing from SrB_6 to CaB_6. Metal atom diffusion was tracked using energy dispersive X-ray spectroscopy (EDXS) and the diffusion profiles of Ca in SrB_6 and Sr in CaB_6 displayed concentration-dependent diffusivity. By comparing the total dopant levels of each metal atom in the opposing hexaboride pellet we were able to observe the effects of current flow direction. Total dopant values for both Ca and Sr were found to be higher in the direction of the positive electrode. As this is atypical of ionic conduction, the hypothesis is that the diffusion of vacancies is affected by the electric field. Metal vacancies in hexaboride compounds carry a virtual negative charge and would therefore be pulled in the direction of the positive electrode. Pile-up of these vacancies at the positive end of hexaboride grains would result in increased disorder in the grain boundaries and enhanced grain boundary diffusion. As grain boundary diffusion is typically greater than lattice diffusion, this mechanism dominates and the overall net movement of metal atoms is greater in the direction of the positive electrode. While the influence of electromigration (the diffusion of metallic species due to the flow of electrons) is not normally observed at the low current densities produced in an SPS, the effect cannot be dismissed as it is most likely overshadowed by grain boundary diffusion.

7. References

1. Etourneau J, Mercurio J-P, and Hagenmuller P, *Compounds based on octahedral B6 units: Hexaborides and tetraborides*, in *Boron and refractory borides*. 1977, Springer. p. 115-138.

2. Lafferty J, *Boride cathodes.* Journal of Applied physics, 1951. **22**(3): p. 299-309.

3. Zhang H, Tang J, Zhang Q, Zhao G, Yang G, Zhang J, Zhou O, and Qin LC, *Field Emission of Electrons from Single LaB6 Nanowires.* Advanced Materials, 2006. **18**(1): p. 87-91.

4. Petrosyan VA, *Hexaborides of rare earths as a sensor material for thermoelectric single-photon detectors.* Journal of Contemporary Physics (Armenian Academy of Sciences), 2011. **46**(3): p. 125-129.

5. Takeda M, Fukuda T, Domingo F, and Miura T, *Thermoelectric properties of some metal borides.* Journal of Solid State Chemistry, 2004. **177**(2): p. 471-475.

6. Buzea C and Yamashita T, *Review of the superconducting properties of MgB2.* Superconductor Science and Technology, 2001. **14**(11): p. R115.

7. Matthias B, Corenzwit E, Vandenberg J, and Barz H, *High superconducting transition temperatures of new rare earth ternary borides.* Proceedings of the National Academy of Sciences, 1977. **74**(4): p. 1334-1335.

8. Schell G, Winter H, Rietschel H, and Gompf F, *Electronic structure and superconductivity in metal hexaborides.* Physical Review B, 1982. **25**(3): p. 1589-1599.

9. Mackinnon IDR, Alarco JA, and Talbot PC, *Metal Hexaborides with Sc, Ti or Mn.* Modeling and Numerical Simulation of Material Science, 2013. **03**(04): p. 158-169.

10. Longuet-Higgins H and Roberts MdV. *The Electronic Structure of the Borides MB6*. in *Proceedings of the Royal Society of London A: Mathematical, Physical and Engineering Sciences*. 1954. The Royal Society.

11. Johnson RW and Daane AH, *Electron Requirements of Bonds in Metal Borides.* The Journal of Chemical Physics, 1963. **38**(2): p. 425.

12. Katsura Y, Yamamoto A, Ogino H, Horii S, Shimoyama J-i, Kishio K, and Takagi H, *On the possibility of MgB2-like superconductivity in potassium hexaboride.* Physica C: Superconductivity, 2010. **470**: p. S633-S634.

13. Kolmogorov A, Shah S, Margine E, Kleppe A, and Jephcoat A, *Pressure-driven evolution of the covalent network in CaB 6.* Physical review letters, 2012. **109**(7): p. 075501.

14. Han H, *Density-functional theory study of the effect of pressure on the elastic properties of CaB6.* Chinese Physics B, 2013. **22**(7): p. 077101.

15. Moissan H and Williams P, *Sur la préparation et les propriétés des borures de calcium, de strontium et de baryum*. 1897: Gauthier-Villars.

16. Andrieux L, *The Electrolytic Preparation of the Borides of Calcium, Strontium and Barium.* C.R. Acad. Sci. (Paris), 1928. **184**(91): p. 1413.

17. Aida T, Honda Y, Yamamoto S, and Kawabe U, *Preparation, vapor pressure, and thermionic emission properties of BaB6 powder.* Journal of Applied Physics, 1981. **52**(2): p. 1022-1029.

18. Aono M and Kawai S, *11B nuclear quadrupole interaction in metal hexaborides (MB6).* Journal of Physics and Chemistry of Solids, 1979. **40**(11): p. 797-802.

19. Avetisyan A, Goryachev YM, Kovenskaya B, and Shvartsman E, *Production and properties of alloys based on chromium disilicide and alkaline earth element hexaborides.* Izv. Akad. Nauk SSSR, Neorg. Mater, 1979. **15**(4): p. 663-666.

20. Bliznakov G and Peshev P, *The preparation of cerium, praseodymium, and neodymium hexaborides.* Journal of the Less Common Metals, 1964. **7**(6): p. 441-446.

21. Grechnev GE, Baranovskiy AE, Fil VD, Ignatova TV, Kolobov IG, Logosha AV, Shitsevalova NY, Filippov VB, and Eriksson O, *Electronic structure and bulk*

properties of MB[sub 6] and MB[sub 12] borides. Low Temperature Physics, 2008. **34**(11): p. 921.

22. Jha M, Patra R, Ghosh S, and Ganguli AK, *Vertically aligned nanorods of lanthanum hexaboride with efficient field emission properties.* Solid State Communications, 2013. **153**(1): p. 35-39.

23. Latini A, Di Pascasio F, and Gozzi D, *A new synthesis route to light lanthanide borides: borothermic reduction of oxides enhanced by electron beam bombardment.* Journal of alloys and compounds, 2002. **346**(1): p. 311-313.

24. Menaka, Patra R, Ghosh S, and Ganguli AK, *Novel borothermal route for the synthesis of lanthanum cerium hexaborides and their field emission properties.* Journal of Solid State Chemistry, 2012. **194**: p. 173-178.

25. Muratov V, Bolgar A, Loboda P, and Morozov V, *Enthalpy and heat capacity of CeB 6, PrB 6, and EuB 6 in a wide temperature range.* Powder Metallurgy and Metal Ceramics, 1988. **27**(12): p. 984-988.

26. Paderno YB, Pokrzywnicki S, and Staliński B, *Magnetic properties of some rare earth hexaborides.* physica status solidi (b), 1967. **24**(1): p. K73-K76.

27. Rhyee J-S and Cho BK, *Anomalous electronic transport and magnetic instability in Eu[sub 1−x]La[sub x]B[sub 6] (x=0.0, 0.1, 0.2, and 0.3).* Journal of Applied Physics, 2005. **97**(10): p. 10A901.

28. Samsonov G, Kondrashov A, Okhremchuk L, Podchernyaeva I, and Fomenko V, *Thermionic properties of lanthanum hexaborite alloys with refractory compounds and nickel.* Poroshk. Metall, 1976: p. 89-91.

29. Schwetz K, Hoerle M, and Bauer J, *Contribution to the system Europium—boron—carbon.* Ceramurgia International, 1979. **5**(3): p. 105-109.

30. Serebryakova T and Marek E, *Conditions of preparation of calcium and barium hexaboride powders.* Powder Metallurgy and Metal Ceramics, 1969. **8**(8): p. 608-612.

31. Takeda M, Terui M, Takahashi N, and Ueda N, *Improvement of thermoelectric properties of alkaline-earth hexaborides.* Journal of Solid State Chemistry, 2006. **179**(9): p. 2823-2826.

32. Tarascon J, Soubeyroux J, Etourneau J, Georges R, Coey J, and Massenet O, *Magnetic structures determined by neutron diffraction in the EuBϵ− xCx system.* Solid State Communications, 1981. **37**(2): p. 133-137.

33. Tsuji R, Sato K, and Takeda M. *PN control of YbB 6*. in *Thermoelectrics, 2007. ICT 2007. 26th International Conference on*. 2007. IEEE.

34. Akkoyunlu A, Koc R, Mawdsley J, and Carter D, *Synthesis of submicron size CaB6 powder using various boron sorces.* Nanostructured Materials and Nanotechnology, 2011. **V**: p. 127-135.

35. Hasan M, Sugo H, and Kisi E, *Low temperature carbothermal and boron carbide reduction synthesis of LaB6.* Journal of Alloys and Compounds, 2013. **578**: p. 176-182.

36. Lin Z, Guanghui M, and Huashun Y, *Reaction mechanism and size control of CaB6 micron powder synthesized by the boroncarbide method.* Ceramics International, 2009. **35**(8): p. 3533-3536.

37. Liu Y, Lu WJ, Qin JN, and Zhang D, *A new route for the synthesis of NdB6 powder from Nd2O3–B4C system.* Journal of Alloys and Compounds, 2007. **431**(1-2): p. 337-341.

38. Min G, Zheng S, Zou Z, Yu H, and Han J, *Reaction synthesis and formation mechanism of barium hexaboride.* Materials Letters, 2003. **57**(7): p. 1330-1333.

39. Sonber JK, Murthy TSRC, Subramanian C, Hubli RC, and Suri AK, *Synthesis, densification and characterization of EuB6.* International Journal of Refractory Metals and Hard Materials, 2013. **38**: p. 67-72.

40. Takeda H, Kuno H, and Adachi K, *Solar Control Dispersions and Coatings With Rare-Earth Hexaboride Nanoparticles.* Journal of the American Ceramic Society, 2008. **91**(9): p. 2897-2902.

41. Yildiz Ö, Telle R, Schmalzried C, and Kaiser A, *Phase transformation of transient B4C to CaB6 during production of CaB6 from colemanite.* Journal of the European Ceramic Society, 2005. **25**(14): p. 3375-3381.

42. Zheng S, Min G, Zou Z, Yu H, and Han J, *Synthesis of calcium hexaboride powder via the reaction of calcium carbonate with boron carbide and carbon.* Journal of the American Ceramic Society, 2001. **84**(11): p. 2725-2727.

43. Carenco S, Portehault D, Boissiere C, Mezailles N, and Sanchez C, *Nanoscaled metal borides and phosphides: recent developments and perspectives.* Chemical reviews, 2013. **113**(10): p. 7981-8065.

44. Ammar A, Menetrier M, Villesuzanne A, Matar S, Chevalier B, and Etourneau J, *Investigarion of the electronic and structural properties of potassium hexaboride, KB6, by transport, magnetic susceptibility, EPR and NMR measurments, temperature-dependent crystal structure determination and electronic band structure calculations.* Inorganic Chemistry, 2004. **43**(4974-4987).

45. Gürsoy M, Takeda M, and Albert B, *High-pressure densified solid solutions of alkaline earth hexaborides (Ca/Sr, Ca/Ba, Sr/Ba) and their high-temperature thermoelectric properties.* Journal of Solid State Chemistry, 2015. **221**: p. 191-195.

46. Aprea A, Maspero A, Masciocchi N, Guagliardi A, Albisetti AF, and Giunchi G, *Nanosized rare-earth hexaborides: Low-temperature preparation and microstructural analysis.* Solid State Sciences, 2013. **21**: p. 32-36.

47. Balcı Ö, Ağaoğulları D, Duman İ, and Öveçoğlu ML, *Synthesis of CaB6 powders via mechanochemical reaction of Ca/B2O3 blends.* Powder Technology, 2012. **225**: p. 136-142.

48. Bao L-H, Zhang J-X, Zhang N, Li X-N, and Zhou S-L, *In situ(LaxGd1−x)B6cathode materials prepared by the spark plasma sintering technique.* Physica Scripta, 2012. **85**(3): p. 035710.

49. Balakrishnan G, Lees MR, and Paul DM, *Growth of large single crystals of rare earth hexaborides.* Journal of Crystal Growth, 2003. **256**(1-2): p. 206-209.

50. Bat'ko I, Bat'ková M, Flachbart K, Filippov VB, Paderno YB, Shicevalova NY, and Wagner T, *Electrical resistivity and superconductivity of LaB6 and LuB12.* Journal of Alloys and Compounds, 1995. **217**(2): p. L1-L3.

51. Batkova M, Batko I, Konovalova E, and Shitsevalova N, *Tunneling Spectroscopy Studies of SmB~ 6 and YbB~ 1~ 2.* ACTA PHYSICA POLONICA SERIES A, 2008. **113**(1): p. 255.

52. Iwashita K, Matsumura T, Segawa K, and Kunii S, *Electrical and magnetic properties of heavy rare-earth hexaborides.* Physica B: Condensed Matter, 1993. **186**: p. 636-638.

53. Le MD, McEwen KA, Park JG, Lee S, Iga F, and Rule KC, *Magnetic excitations in the ordered phases of praseodymium hexaboride.* Journal of Physics: Condensed Matter, 2008. **20**(10): p. 104231.

54. Mercurio J, Etourneau J, Naslain R, and Hagenmuller P, *Electrical and magnetic properties of some rare-earth hexaborides.* Journal of the Less Common Metals, 1976. **47**: p. 175-180.

55. Petrosyan V, Vardanyan V, Kuzanyan V, Konovalov M, Gurin V, and Kuzanyan A, *Thermoelectric properties and chemical composition of CeB6 crystals obtained by various methods.* Solid State Sciences, 2012. **14**(11-12): p. 1653-1655.

56. Segawa K, Tomita A, Iwashita K, Kasaya M, Suzuki T, and Kunii S, *Electronic and magnetic properties of heavy rare-earth hexaboride single crystals.* Journal of Magnetism and Magnetic Materials, 1992. **104**: p. 1233-1234.

57. Teyssier J, Kuzmenko A, van der Marel D, Lortz R, Junod A, Filippov V, and Shitsevalova N, *Electronic and optical properties of ZrB12 and YB6. Discussion on electron-phonon coupling.* physica status solidi (c), 2006. **3**(9): p. 3114-3117.

58. Walker H, McEwen K, McMorrow D, Bleckmann M, Park JG, Lee S, Iga F, and Mannix D, *X-ray resonant scattering study of the structural and magnetic transitions in PrB6.* Physical Review B, 2009. **79**(5).

59. Otani S, Nakagawa H, Nishi Y, and Kieda N, *Floating Zone Growth and High Temperature Hardness of Rare-Earth Hexaboride Crystals: LaB6, CeB6, PrB6, NdB6, and SmB6.* Journal of Solid State Chemistry, 2000. **154**(1): p. 238-241.

60. Amalajyothi K, Berchmans LJ, Angappan S, and Visuvasam A, *Electrosynthesis of cerium hexaboride by the molten salt technique.* Journal of Crystal Growth, 2008. **310**(14): p. 3376-3379.

61. Amalajyothi K, Berchmans LJ, Visuvasam A, and Angappan S, *Electrosynthesis of Cerium Hexaboride using Lithium Tetra Borate Melt.* Materials and Manufacturing Processes, 2011. **26**: p. 792-795.

62. Angappan S, Helan M, Visuvasam A, Berchmans LJ, and Ananth V, *Electrolytic preparation of CaB6 by molten salt technique.* Ionics, 2011. **17**(6): p. 527-533.

63. Angappan S, Kalaiselvi N, Sudha R, and Visuvasam A, *Electrochemical Synthesis of Magnesium Hexaboride by Molten Salt Technique.* Int Sch Res Notices, 2014. **2014**: p. 123194.

64. Bukatova GA, Kuznetsov SA, and Gaune-Escard M, *Electrochemical synthesis of rare-earth metal (Eu, Nd) borides in molten salts.* Russian Journal of Electrochemistry, 2007. **43**(8): p. 929-935.

65. Uchida K and Shiota M, *Electrodeposited mixed hexaborides of sodium and lanthanum.* Surface Technology, 1978. **7**(4): p. 299-304.

66. Wang X and Zhai Y, *An electrochemical method for the preparation of CaB6 crystal powder.* Journal of Applied Electrochemistry, 2009. **39**(10): p. 1797-1802.

67. Scholz H, Bauhofer W, and Ploog K, *Preparation of lanthanum hexaboride by electrolysis and measurements of the Raman-active phonons.* Solid State Communications, 1976. **18**(11-12): p. 1539-1542.

68. Amsler B, Fisk Z, Sarrao JL, von Molnar S, Meisel MW, and Sharifi F, *Electron tunneling studies of the hexaboride materials SmB6, EuB6, CeB6 and SrB6.* Physical Review B, 1998. **57**(15): p. 8747-8750.

69. Chen C-H, Aizawa T, Iyi N, Sato A, and Otani S, *Structural refinement and thermal expansion of hexaborides.* Journal of Alloys and Compounds, 2004. **366**(1-2): p. L6-L8.

70. Derkachenko L, Gurin V, Korsukova M, Jung W, and Müller R, *A new criterion for explaining the polar and reticular microhardness anisotropy of tetra-and hexaborides of lanthanides and actinides.* Journal of Solid State Chemistry, 1997. **133**(1): p. 296-301.

71. Futamoto M, Aita T, and Kawabe U, *Microhardness of hexaboride single crystals.* Materials Research Bulletin, 1979. **14**(10): p. 1329-1334.

72. Gurin V, Konovalov M, Kuzanyan A, Petrosyan V, Burkhardt U, and Grin J, *Chemical composition topography in RE hexaboride crystals obtained by various solution-melt methods.* Solid State Sciences, 2012. **14**(11-12): p. 1705-1709.

73. Gurin V, Korsukova M, Nikanorov S, Smirnov I, Stepanov N, and Shul'man S, *The Preparation of Single Crystals of the Rare Earth Borides by the Solution Method and a Study of their Properties.* Journal of the Less Common Metals, 1979. **67**: p. 115-123.

74. Meegoda M, Trenary M, Mori T, and Otani S, *Depth profile of iron in a CaB6 crystal.* Physical Review B, 2003. **67**(17).

75. Murakami K, Adachi T, Kuroda T, Nakamura S, and Komoda O, *An atom-probe analysis of LaB6 (001) plane.* Surface Science Letters, 1983. **124**(2-3): p. L25-L30.

76. Olsen G and Cafiero A, *Single-crystal growth of mixed (La, Eu, Y, Ce, Ba, Cs) hexaborides for thermionic emission.* Journal of Crystal Growth, 1978. **44**(3): p. 287-290.

77. Ott H, Chernikov M, Felder E, Degiorgi L, Moshopoulou E, Sarrao J, and Fisk Z, *Structure and low temperature properties of SrB6.* Zeitschrift für Physik B Condensed Matter, 1997. **102**(3): p. 337-345.

78. Peshev P, *A thermodynamic analysis of lanthanum hexaboride crystal preparation from aluminum flux with the use of compound precursors.* Journal of Solid State Chemistry, 1997. **133**(1): p. 237-242.

79. Süllow S, Prasad I, Aronson M, Bogdanovich S, Sarrao J, and Fisk Z, *Metallization and magnetic order in EuB 6.* Physical Review B, 2000. **62**(17): p. 11626.

80. Vonlanthen P, Felder E, Degiorgi L, Ott H, Young D, Bianchi A, and Fisk Z, *Electronic transport and thermal and optical properties of Ca 1− x La x B 6.* Physical Review B, 2000. **62**(15): p. 10076.

81. Wigger G, Beeli C, Felder E, Ott H, Bianchi A, and Fisk Z, *Percolation and the Colossal Magnetoresistance of Eu-Based Hexaboride.* Physical Review Letters, 2004. **93**(14).

82. Matsubayashi K, Maki M, Tsuzuki T, Nishioka T, and Sato N, *Magnetic properties: Parasitic ferromagnetism in a hexaboride?* Nature, 2002. **420**(6912): p. 143-144.

83. Mori T and Otani S, *Ferromagnetism in lanthanum doped CaB 6: is it intrinsic?* Solid state communications, 2002. **123**(6): p. 287-290.

84. Amin SS, Li S-y, Roth JR, and Xu TT, *Single crystalline alkaline earth metal hexaboride one dimensional (1D) nanostructures: synthesis and characterization.* Chemistry of Materials, 2009. **21**: p. 763-770.

85. Gernhart ZC, Jacobberger RM, Wang L, Brewer JR, Dar MA, Diercks DR, Mei WN, Cheung CL, and Mullins W, *Existence of Erbium Hexaboride Nanowires.* Journal of the American Ceramic Society, 2012. **95**(12): p. 3992-3996.

86. Jash P, Nicholls AW, Ruoff RS, and Trenary M, *Synthesis and characterization of single-crystal strontium hexaboride nanowires.* Nano letters, 2008. **8**(11): p. 3794-3798.

87. Wu X and Xu TT, *Measurement of mechanical properties of alkaline-earth metal hexaboride one-dimensional nanostructures by nanoindentation.* Journal of Materials Research, 2012. **27**(09): p. 1218-1229.

88. Xu J, Chen X, Zhao Y, Zou C, and Ding Q, *Single-crystalline PrB6 nanowires and their field-emission properties.* Nanotechnology, 2007. **18**(11): p. 115621.

89. Xu J, Chen X, Zhao Y, Zou C, Ding Q, and Jian J, *Self-catalyst growth of EuB6 nanowires and nanotubes.* Journal of Crystal Growth, 2007. **303**(2): p. 466-471.

90. Xu J, Hou G, Li H, Zhai T, Dong B, Yan H, Wang Y, Yu B, Bando Y, and Golberg D, *Fabrication of vertically aligned single-crystalline lanthanum hexaboride nanowire arrays and investigation of their field emission.* NPG Asia Materials, 2013. **5**(7): p. e53.

91. Xu J, Hou G, Mori T, Li H, Wang Y, Chang Y, Luo Y, Yu B, Ma Y, and Zhai T, *Excellent Field-Emission Performances of Neodymium Hexaboride (NdB6) Nanoneedles with Ultra-Low Work Functions.* Advanced Functional Materials, 2013. **23**(40): p. 5038-5048.

92. Xu J, Zhao Y, Zou C, and Ding Q, *Self-catalyst growth of single-crystalline CaB6 nanostructures.* Journal of Solid State Chemistry, 2007. **180**(9): p. 2577-2580.

93. Xu TT, Zheng J-G, Nicholls AW, Stankovich S, Piner RD, and Ruoff RS, *Single-Crystal Calcium Hexaboride Nanowires: Synthesis and Characterization.* Nano Letters, 2004. **4**(10): p. 2051-2055.

94. Kher SS and Spencer JT, *CHEMICAL VAPOR DEPOSITION OF METAL BORIDES: 7. THE RELATIVELY LOW TEMPERATURE FORMATION OF CRYSTALLINE LANTHANUM HEXABORIDE THIN FILMS FROM BORON HYDRIDE CLUSTER COMPOUNDS BY CHEMICAL VAPOR DEPOSITION [1].* Journal of Physics and Chemistry of Solids, 1998. **59**(8): p. 1343-1351.

95. Brewer JR, Deo N, Morris Wang Y, and Cheung CL, *Lanthanum hexaboride nanoobelisks.* Chemistry of Materials, 2007. **19**(26): p. 6379-6381.

96. Ding Q, Zhao Y, Xu J, and Zou C, *Large-scale synthesis of neodymium hexaboride nanowires by self-catalyst.* Solid State Communications, 2007. **141**(2): p. 53-56.

97. Fan QH, Zhao YM, and Li DD, *Synthesis of single-crystalline lanthanum hexaboride nanowires by Au catalyst.* Ceramics International, 2013. **39**(6): p. 6271-6275.

98. Zou CY, Zhao YM, and Xu JQ, *Synthesis of single-crystalline CeB6 nanowires.* Journal of Crystal Growth, 2006. **291**(1): p. 112-116.

99. Kajiwara T, Urakabe T, Sano K, Fukuyama K, Watanabe K, Baba S, Nakano T, and Kinbara A, *Mechanical and electrical properties of rf sputtered LaB6 thin films on glass substrates.* Vacuum, 1990. **41**(4): p. 1224-1228.

100. Mushiaki M, Akaishi K, Mori T, Kubota Y, Funato Y, and Motojima O, *LaB6 coating to reduce the outgassing rate of a vacuum wall.* Materials Science and Engineering: A, 1993. **163**(2): p. 177-179.

101. Ociepa JG and Mróz S, *Properties of very thin La-B films deposited onto tantalum.* Thin Solid Films, 1981. **85**(1): p. 43-51.

102. Ryan JG and Roberts S, *The formation and characterization of rare earth boride films.* Thin Solid Films, 1986. **135**(1): p. 9-19.

103. Winsztal S, Majewska-Minor H, Wisniewska M, and Niemyski T, *Preparation and investigation of LaB6 films.* Materials Research Bulletin, 1973. **8**(12): p. 1329-1335.

104. Kondrashin AA, *EMISSIVE PLASMA COATINGS BASED ON LAB 6.* INORG. MATER. Inorg. Mater., 1982. **18**(1): p. 34.

105. Szépvölgyi J, Mohai I, Károly Z, and Gál L, *Synthesis of nanosized ceramic powders in a radiofrequency thermal plasma reactor.* Journal of the European Ceramic Society, 2008. **28**(5): p. 895-899.

106. Amalajyothi K and Berchmans LJ, *Combustion synthesis of nanocrystalline cerium hexaboride using citric acid as a fuel.* International Journal of Self-Propagating High-Temperature Synthesis, 2009. **18**(3): p. 151-153.

107. Dou Z-h, Zhang T-a, Zhang Z-q, Zhang H-b, and He J-c, *Preparation and characterization of LaB6 ultra fine powder by combustion synthesis.* Transactions of Nonferrous Metals Society of China, 2011. **21**(8): p. 1790-1794.

108. Dou ZH, Zhang TA, and He JC. *Preparation and Characterization of Cerium Hexaboride Nanometer Powders by Combustion Synthesis*. in *Advanced Materials Research*. 2011. Trans Tech Publ.

109. Huang X, Zhong J, Dou L, and Wang K, *Combustion synthesis of CaB6 powder from calcium hexaborate and Mg.* International Journal of Refractory Metals and Hard Materials, 2010. **28**(2): p. 143-149.

110. Kanakala R, Escudero R, Rojas-George G, Ramisetty M, and Graeve OA, *Mechanisms of combustion synthesis and magnetic response of high-surface-area hexaboride compounds.* ACS Appl Mater Interfaces, 2011. **3**(4): p. 1093-100.

111. Kanakala R, Rojas-George G, and Graeve OA, *Unique Preparation of Hexaboride Nanocubes: A First Example of Boride Formation by Combustion Synthesis.* Journal of the American Ceramic Society, 2010. **93**(10): p. 3136-3141.

112. Selvan RK, Genish I, Perelshtein I, Calderon Moreno JM, and Gedanken A, *Single step, low-temperature synthesis of submicron-sized rare earth hexaborides.* The Journal of Physical Chemistry C, 2008. **112**(6): p. 1795-1802.

113. Brewer L, Sawyer DL, Templeton D, and Dauben CH, *A study of the refractory borides.* Journal of the American Ceramic Society, 1951. **34**(6): p. 173-179.

114. Mohammadi R, Lech AT, Xie M, Weaver BE, Yeung MT, Tolbert SH, and Kaner RB, *Tungsten tetraboride, an inexpensive superhard material.* Proceedings of the National Academy of Sciences, 2011. **108**(27): p. 10958-10962.

115. Koester R and Moak D, *Hot hardness of selected borides, oxides, and carbides to 1900 C.* Journal of the American Ceramic Society, 1967. **50**(6): p. 290-296.

116. Chatterjee A, Jayaraman S, Gerbi J, Kumar N, Abelson J, Bellon P, Polycarpou A, and Chevalier J, *Tribological behavior of hafnium diboride thin films.* Surface and Coatings Technology, 2006. **201**(7): p. 4317-4322.

117. Schwarzkopf P and Glaser F, *Borides Designed for High Temperature Use.* Iron Age, 1954. **173**: p. 138-9.

118. Matthias B, Geballe T, Andres K, Corenzwit E, Hull G, and Maita J, *Superconductivity and antiferromagnetism in boron-rich lattices.* Science, 1968. **159**.

119. Lundström T, *Borides: Solid-State Chemistry.* Enclyopedia of Inorganic Chemistry, 2006.

120. Guo-Liang X, Jing-Dong C, Yao-Zheng X, Xue-Feng L, Yu-Fang L, and Xian-Zhou Z, *First-principles calculations of elastic and thermal properties of lanthanum hexaboride.* Chinese Physics Letters, 2009. **26**(5): p. 056201.

121. Zakaryan DA, Kartuzov VV, and Khachatryan AV, *Ab-initio calculation of the coefficients of thermal expansion for MeB2 (Me–Ti, Zr) and LaB6 borides and LaB6–MeB2 eutectic composites.* Powder Metallurgy and Metal Ceramics, 2012. **51**(5-6): p. 301-306.

122. Sirota NN, Novikov VV, and Novikov AV, *Identity period and thermal expansion coefficient for rare-earth hexaborides at temperatures of 5–320 K.* Physics of the Solid State, 2000. **42**(11): p. 2093-2096.

123. Sirota NN, Novikov VV, Vinokurov VA, and Paderno YB, *Temperature dependence of the heat capacity and lattice constant of lanthanum and samarium hexaborides.* Physics of the Solid State, 1998. **40**(11): p. 1856-1858.

124. Fisk Z, Ott H, Barzykin V, and Gor'kov L, *The emerging picture of ferromagnetism in the divalent hexaborides.* Physica B: Condensed Matter, 2002. **312**: p. 808-810.

125. Ott H, Gavilano J, Ambrosini B, Vonlanthen P, Felder E, Degiorgi L, Young D, Fisk Z, and Zysler R, *Unusual magnetism of hexaborides.* Physica B: Condensed Matter, 2000. **281**: p. 423-427.

126. Mandrus D, Sales B, and Jin R, *Localized vibrational mode analysis of the resistivity and specific heat of LaB6.* Physical Review B, 2001. **64**(1).

127. Takeda M, Fukuda T, and Miura T. *Thermoelectric properties of metal-hexaborides*. in *Thermoelectrics, 2002. Proceedings ICT'02. Twenty-First International Conference on*. 2002. IEEE.

128. Schmitt K, Stückl C, Ripplinger H, and Albert B, *Crystal and electronic structure of BaB 6 in comparison with CaB 6 and molecular [B 6 H 6] 2−*. Solid state sciences, 2001. **3**(3): p. 321-327.

129. Massidda S, Continenza A, De Pascale T, and Monnier R, *Electronic structure of divalent hexaborides.* Zeitschrift für Physik B Condensed Matter, 1996. **102**(1): p. 83-89.

130. Snow C, Cooper S, Young D, Fisk Z, Comment A, and Ansermet J-P, *Magnetic polarons and the metal-semiconductor transitions in (Eu,La)B6 and EuO: Raman scattering studies.* Physical Review B, 2001. **64**(17).

131. Süllow S, Prasad I, Aronson M, Sarrao J, Fisk Z, Hristova D, Lacerda A, Hundley M, Vigliante A, and Gibbs D, *Structure and magnetic order of EuB 6.* Physical Review B, 1998. **57**(10): p. 5860.

132. Menth A, Buehler E, and Geballe T, *Magnetic and Semiconducting Properties of Sm B 6.* Physical Review Letters, 1969. **22**(7): p. 295.

133. Flachbart K, Gloos K, Konovalova E, Paderno Y, Reiffers M, Samuely P, and Švec P, *Energy gap of intermediate-valent SmB6 studied by point-contact spectroscopy.* Physical Review B, 2001. **64**(8).

134. Wachter P, *Handbook on the Physics and Chemistry of Rare Earths.* Vol. 2North-Holland, Amsterdam, 1979. **19**: p. 177.

135. Beille J, Maple MB, Wittig J, Fisk Z, and DeLong LE, *Suppression of the energy gap in SmB6 under pressure*. 1983.

136. Cooley J, Aronson M, Fisk Z, and Canfield P, *Sm B 6: Kondo Insulator or Exotic Metal?* Physical review letters, 1995. **74**(9): p. 1629.

137. Röhler J, *Handbook on the Physics and Chemistry of Rare Earths.* edited by KA Gschneider Jr, L. Eyring and S. H üfner)(North-Holland, Amsterdam 1987), 1987. **10**.

138. Berman I, Brandt N, Moshchalkov V, Pashkevich S, Sidorov V, Konovalova E, and Paderno IB, *Effect of pressure on the correlation gap in a compound with intermediate valency SmB6.* ZhETF Pisma Redaktsiiu, 1983. **38**: p. 393-396.

139. Cooley J, Mielke C, Hults W, Goettee J, Honold M, Modler R, Lacerda A, Rickel D, and Smith J, *High field gap closure in the Kondo insulator SmB6.* Journal of superconductivity, 1999. **12**(1): p. 171-173.

140. Fisk Z, Cooper A, Schmidt P, and Castellano R, *Preparation and lattice parameters of the rare earth tetraborides.* Materials Research Bulletin, 1972. **7**(4): p. 285-288.

141. Fisk Z, Lawson A, and Fitzgerald R, *Remarks on the mutual solubilities and superconductivity of hexaborides.* Materials Research Bulletin, 1974. **9**(5): p. 633-636.

142. Kunii S, Kasuya T, Kadowaki K, Date M, and Woods S, *Electron tunneling into superconducting YB6.* Solid state communications, 1984. **52**(7): p. 659-661.

143. Geballe T, Matthias B, Andres K, Maita J, Cooper A, and Corenzwit E, *Magnetic ordering in the rare-earth hexaborides.* Science, 1968. **160**(3835): p. 1443-1444.

144. Baťko I, Flachbart K, Miškuf J, Filipov VM, Konovalova ES, and Paderno JB, *Electrical resistivity of SmB6 thin films.* Journal of the Less Common Metals, 1990. **158**(1): p. L17-L19.

145. Altshuler T, Goryunov YV, Shitsevalova NY, and Dukhnenko A. *Effect of anisotropy in temperature dynamics of magnetic phase separation in europium hexaboride*. in *Journal of Physics: Conference Series*. 2010. IOP Publishing.

146. Kunes J and Pickett W, *Kondo and anti-Kondo coupling to local moments in EuB 6.* Physical Review B, 2004. **69**(16): p. 165111.

147. Henggeler W, Ott H-R, Young D, and Fisk Z, *Magnetic ordering in EuB 6, investigated by neutron diffraction.* Solid state communications, 1998. **108**(12): p. 929-932.

148. Altshuler TS, Goryunov YV, Shitsevalova NY, and Dukhnenko A, *Effect of anisotropy in temperature dynamics of magnetic phase separation in europium hexaboride.* Journal of Physics: Conference Series, 2010. **200**(3): p. 032019.

149. Young D, Hall D, Torelli M, Fisk Z, Sarrao J, Thompson J, Ott H-R, Oseroff S, Goodrich R, and Zysler R, *High-temperature weak ferromagnetism in a low-density free-electron gas.* Nature, 1999. **397**(6718): p. 412-414.

150. Dub SN, Kislaya GP, and Loboda PI, *Study of mechanical properties of LaB6 single crystal by nanoindentation.* Journal of Superhard Materials, 2013. **35**(3): p. 158-165.

151. Bao L, Zhang J, and Zhou S, *Effect of particle size on the polycrystalline CeB6 cathode prepared by spark plasma sintering.* Journal of Rare Earths, 2011. **29**(6): p. 580-584.

152. Ogita N, Nagai S, Okamoto N, Udagawa M, Iga F, Sera M, Akimitsu J, and Kunii S, *Raman scattering investigation of R B 6 (R= Ca, La, Ce, Pr, Sm, Gd, Dy, and Yb).* Physical Review B, 2003. **68**(22): p. 224305.

153. Leger J, Rossat-Mignod J, Kunii S, and Kasuya T, *High pressure compression of CeB 6 up to 20 GPa.* Solid state communications, 1985. **54**(11): p. 995-997.

154. Gupta H and Kumar S. *Ab-initio Study Of Zone Centre Phonons In MB6 (M= La, Ce, Sm)*. in *XXII INTERNATIONAL CONFERENCE ON RAMAN SPECTROSCOPY*. 2010. AIP Publishing.

155. Sandeep M, Rai D, Patra P, Mohanty A, and Thapa R. *Study of Bulk modulus, Volume, Energy, lattice parameters and magnetic moments in rare earth hexaborides using density functional theory*. in *Journal of Physics: Conference Series*. 2012.

156. Merzhanov AG and Borovinskaya IP, *A New Class of Combustion Processes†.* Combustion Science and Technology, 1975. **10**(5-6): p. 195-201.

157. Merzhanov AG, *Combustion and explosion processes in physical chemistry and technology of inorganic materials.* Russian Chemical Reviews, 2003. **72**(4): p. 289-310.

158. McCauley JW. *An historical and technical perspective on SHS*. in *14th Annual Conference on Composites and Advanced Ceramic Materials, Part 2 of 2:*

Ceramic Engineering and Science Proceedings, Volume 11, Issue 9/10. 1990. Wiley Online Library.

159. Yi H and Moore J, *Self-propagating high-temperature (combustion) synthesis (SHS) of powder-compacted materials.* Journal of materials Science, 1990. **25**(2): p. 1159-1168.

160. Patil KC, Aruna ST, and Ekambaram S, *Combustion synthesis.* Current opinion in solid state and materials science, 1997. **2**(2): p. 158-165.

161. Patil KC, Aruna ST, and Mimani T, *Combustion synthesis: an update.* Current Opinion in Solid State and Materials Science, 2002. **6**(6): p. 507-512.

162. Merzhanov A, Borovinskaya I, and Ratnikov V, *A method of producing refractory inorganic compounds.* Inventor's Certificate, 1967. **736541**: p. 131.

163. Aldushin A, Merzhanov A, and Khaikin B. *Some Peculiarities of Condensed System Combustion with Refractory Reaction Products*. in *Dokl. Akad. Nauk SSSR*. 1972.

164. Zel'dovich Y and Frank-Kamenetskii D, Zh. Fiz. Khim, 1938. **12**: p. 100.

165. *Solution combustion synthesis.* https://www.youtube.com/watch?v=u3IDWm3XZxI

166. Ravindranathan P and Patil K, *A one-step process for the preparation ofγ-Fe 2 O 3.* Journal of materials science letters, 1986. **5**(2): p. 221-222.

167. Chick LA, Pederson L, Maupin G, Bates J, Thomas L, and Exarhos G, *Glycine-nitrate combustion synthesis of oxide ceramic powders.* Materials Letters, 1990. **10**(1): p. 6-12.

168. Shea LE, McKittrick J, Lopez OA, and Sluzky E, *Synthesis of Red-Emitting, Small Particle Size Luminescent Oxides Using an Optimized Combustion Process.* Journal of the American Ceramic Society, 1996. **79**(12): p. 3257-3265.

169. McKittrick J, Shea L, Bacalski C, and Bosze E, *The influence of processing parameters on luminescent oxides produced by combustion synthesis.* Displays, 1999. **19**(4): p. 169-172.

170. Mimani T and Patil K, *Solution combustion synthesis of nanoscale oxides and their composites.* Materials Physics and Mechanics(Russia), 2001. **4**(2): p. 134-137.

171. Pathak L, Singh T, Das S, Verma A, and Ramachandrarao P, *Effect of pH on the combustion synthesis of nano-crystalline alumina powder.* Materials Letters, 2002. **57**(2): p. 380-385.

172. Aruna S and Rajam K, *Mixture of fuels approach for the solution combustion synthesis of Al 2 O 3–ZrO 2 nanocomposite.* Materials research bulletin, 2004. **39**(2): p. 157-167.

173. Dinka P and Mukasyan AS, *In situ preparation of oxide-based supported catalysts by solution combustion synthesis.* The Journal of Physical Chemistry B, 2005. **109**(46): p. 21627-21633.

174. Bansal NP and Zhong Z, *Combustion synthesis of Sm 0.5 Sr 0.5 CoO 3− x and La 0.6 Sr 0.4 CoO 3− x nanopowders for solid oxide fuel cell cathodes.* Journal of Power Sources, 2006. **158**(1): p. 148-153.

175. Mukasyan AS, Epstein P, and Dinka P, *Solution combustion synthesis of nanomaterials.* Proceedings of the Combustion Institute, 2007. **31**(2): p. 1789-1795.

176. Prakash A, Manikandan P, Ramesha K, Sathiya M, Tarascon J, and Shukla A, *Solution-combustion synthesized nanocrystalline Li4Ti5O12 as high-rate performance Li-ion battery anode.* Chemistry of Materials, 2010. **22**(9): p. 2857-2863.

177. Reddy AJ, Kokila M, Nagabhushana H, Chakradhar R, Shivakumara C, Rao J, and Nagabhushana B, *Structural, optical and EPR studies on ZnO: Cu nanopowders prepared via low temperature solution combustion synthesis.* Journal of Alloys and Compounds, 2011. **509**(17): p. 5349-5355.

178. Lenel F, *Resistance sintering under pressure.* J. Metals, 1955. **7**.

179. Goldberger W, Merkle B, and Boss D, *Making Dense Near-Net Shaped Parts by Electroconsolidation [TM].* Advances in Powder Metallurgy and Particulate Materials, 1994. **6**: p. 91-91.

180. Shon I and Munir Z, *Synthesis of MoSi 2 xNb and MoSi 2 yZrO 2 composites by the field-activated combustion method.* Materials Science and Engineering: A, 1995. **202**(1): p. 256-261.

181. Tokita M. *Mechanism of spark plasma sintering*. in *Proceeding of NEDO International Symposium on Functionally Graded Materials*. 1999. Japan.

182. Xie G, Ohashi O, Song M, Mitsuishi K, and Furuya K, *Reduction mechanism of surface oxide films and characterization of formations on pulse electric-current sintered Al–Mg alloy powders.* Applied surface science, 2005. **241**(1): p. 102-106.

183. Munir Z, Anselmi-Tamburini U, and Ohyanagi M, *The effect of electric field and pressure on the synthesis and consolidation of materials: a review of the spark plasma sintering method.* Journal of Materials Science, 2006. **41**(3): p. 763-777.

184. Clark DE and Sutton WH, *Microwave processing of materials.* Annual Review of Materials Science, 1996. **26**(1): p. 299-331.

185. German RM, *Sintering theory and practice.* Solar-Terrestrial Physics (Solnechno-zemnaya fizika), 1996: p. 568.

186. Anselmi-Tamburini U, Gennari S, Garay JE, and Munir ZA, *Fundamental investigations on the spark plasma sintering/synthesis process.* Materials Science and Engineering: A, 2005. **394**(1-2): p. 139-148.

187. Nishimura T, Mitomo M, Hirotsuru H, and Kawahara M, *Fabrication of silicon nitride nano-ceramics by spark plasma sintering.* Journal of materials science letters, 1995. **14**(15): p. 1046-1047.

188. Shen Z, Johnsson M, Zhao Z, and Nygren M, *Spark plasma sintering of alumina.* Journal of the American Ceramic Society, 2002. **85**(8): p. 1921-1927.

189. Cha SI and Hong SH, *Microstructures of binderless tungsten carbides sintered by spark plasma sintering process.* Materials Science and Engineering: A, 2003. **356**(1-2): p. 381-389.

190. Angerer P, Yu L, Khor KA, Korb G, and Zalite I, *Spark-plasma-sintering (SPS) of nanostructured titanium carbonitride powders.* Journal of the European Ceramic Society, 2005. **25**(11): p. 1919-1927.

191. Li JF, Wang K, Zhang BP, and Zhang LM, *Ferroelectric and Piezoelectric Properties of Fine-Grained Na0. 5K0. 5NbO3 Lead-Free Piezoelectric Ceramics Prepared by Spark Plasma Sintering.* Journal of the American Ceramic Society, 2006. **89**(2): p. 706-709.

192. Kim B-N, Hiraga K, Morita K, and Yoshida H, *Spark plasma sintering of transparent alumina.* Scripta Materialia, 2007. **57**(7): p. 607-610.

193. Sciti D, Guicciardi S, and Nygren M, *Spark plasma sintering and mechanical behaviour of ZrC-based composites.* Scripta materialia, 2008. **59**(6): p. 638-641.

194. Guo SQ, Nishimura T, Kagawa Y, and Yang JM, *Spark plasma sintering of zirconium diborides.* Journal of the American Ceramic Society, 2008. **91**(9): p. 2848-2855.

195. Couret A, Molénat G, Galy J, and Thomas M, *Microstructures and mechanical properties of TiAl alloys consolidated by spark plasma sintering.* Intermetallics, 2008. **16**(9): p. 1134-1141.

196. Kelly JP and Graeve OA, *Mechanisms of pore formation in high-temperature carbides: Case study of TaC prepared by spark plasma sintering.* Acta Materialia, 2015. **84**: p. 472-483.

197. *Toyota Mirai.* https://ssl.toyota.com/mirai/fcv.html

198. Fick A, *Ueber diffusion.* Annalen der Physik, 1855. **170**(1): p. 59-86.

199. Boltzmann L, *Zur integration der Diffusionsgleichung bei variabeln Diffusionscoefficienten.* Annalen der Physik, 1894. **289**(13): p. 959-964.

200. Matano C, *On the relation between the diffusion-coefficients and concentrations of solid metals (the nickel-copper system)*. Jpn. J. Phys, 1933. **8**(3): p. 109-113.

201. Dorneles L, Venkatesan M, Moliner M, Lunney J, and Coey J, *Magnetism in thin films of CaB6 and SrB6.* Applied physics letters, 2004. **85**(26): p. 6377-6379.

202. Wang XX, Chan HLW, Pang GKH, and Choy CL, *Semiconducting barium titanate ceramics prepared by using yttrium hexaboride as sintering aid.* Materials Science and Engineering: B, 2003. **100**(3): p. 286-291.

203. Zhang JX, Bao LH, and Zhou SL. *Thermal emission property of solid solution Gd 1− x Nd x B 6 (x= 0, 0.6, 0.8)*. in *2011 IEEE International Vacuum Electronics Conference (IVEC)*. 2011.

204. Badalyan G, Kuzanyan A, Petrosyan V, Kuzanyan V, and Gulian A. *Investigation of the elemental composition of lanthanum-cerium hexaboride crystals*. in *International Conference on Laser Physics 2010*. 2010. International Society for Optics and Photonics.

205. Trunov V, Malyshev A, Chernyshov DY, Kurbakov A, Korsukova M, Gurin V, Antson O, and Hiismäki P, *Problems of studying the crystal structure of Ce1− xLax11B6 solid solutions by high-resolution powder neutron diffraction.* Journal of applied crystallography, 1991. **24**(2): p. 142-145.

206. Holt J and Dunmead S, *Self-heating synthesis of materials.* Annual review of materials science, 1991. **21**(1): p. 305-334.

207. Varma A, Rogachev AS, Mukasyan AS, and Hwang S, *Combustion synthesis of advanced materials: principles and applications.* advances in chemical engineering, 1998. **24**: p. 79-226.

208. Broqvist P, Grönbeck H, and Panas I, *Surface properties of alkaline earth metal oxides.* Surface science, 2004. **554**(2): p. 262-271.

209. Königstein M and Catlow CRA, *Ab InitioQuantum Mechanical Study of the Structure and Stability of the Alkaline Earth Metal Oxides and Peroxides.* Journal of Solid State Chemistry, 1998. **140**(1): p. 103-115.

210. Bao L, Qi X, Chao L, and Tegus O, *Synthesis, and magnetic and optical properties of nanocrystalline alkaline-earth hexaborides.* CrystEngComm, 2016. **18**(7): p. 1223-1229.

211. Anselmi-Tamburini U, Garay JE, and Munir ZA, *Fundamental investigations on the spark plasma sintering/synthesis process.* Materials Science and Engineering: A, 2005. **407**(1-2): p. 24-30.

212. Bertolino N, Garay J, Anselmi-Tamburini U, and Munir Z, *Electromigration effects in Al-Au multilayers.* Scripta materialia, 2001. **44**(5): p. 737-742.

213. Friedman JR, Garay JE, Anselmi-Tamburini U, and Munir ZA, *Modified interfacial reactions in Ag–Zn multilayers under the influence of high DC currents.* Intermetallics, 2004. **12**(6): p. 589-597.

214. Liu W-C, Chen S-W, and Chen C-M, *The Al/Ni interfacial reactions under the influence of electric current.* Journal of electronic materials, 1998. **27**(1): p. L6-L9.

215. Zhao J, Unuvar C, Anselmi-Tamburini U, and Munir Z, *Kinetics of current-enhanced dissolution of nickel in liquid aluminum.* Acta Materialia, 2007. **55**(16): p. 5592-5600.

216. Frei JM, Anselmi-Tamburini U, and Munir ZA, *Current effects on neck growth in the sintering of copper spheres to copper plates by the pulsed electric current method.* Journal of Applied Physics, 2007. **101**(11): p. 114914.

217. Chen S-W, Chen C-M, and Liu W-C, *Electric current effects upon the Sn/Cu and Sn/Ni interfacial reactions.* Journal of electronic materials, 1998. **27**(11): p. 1193-1199.

218. Chen C-M and Chen S-W, *Electric current effects on Sn/Ag interfacial reactions.* Journal of electronic materials, 1999. **28**(7): p. 902-906.

219. Chen C-M and Chen S-W, *Electromigration effect upon the Zn/Ni and Bi/Ni interfacial reactions.* Journal of electronic materials, 2000. **29**(10): p. 1222-1228.

220. Kelly JP and Graeve OA, *Spark Plasma Sintering as an Approach to Manufacture Bulk Materials: Feasibility and Cost Savings.* JOM, 2015. **67**(1): p. 29-33.

221. Graeve O, Saterlie M, Kanakala R, de la Torre SD, and Farmer J, *The kinetics of devitrification of amorphous alloys: The time–temperature–crystallinity diagram describing the spark plasma sintering of Fe-based metallic glasses.* Scripta Materialia, 2013. **69**(2): p. 143-148.

222. Sinha K, Pearson B, Casolco SR, Garay JE, and Graeve OA, *Synthesis and consolidation of BaAl2Si2O8: Eu: development of an integrated process for luminescent smart ceramic materials.* Journal of the American Ceramic Society, 2009. **92**(11): p. 2504-2511.

223. Graeve OA, Kanakala R, Kaufman L, Sinha K, Wang E, Pearson B, Rojas-George G, and Farmer JC, *Spark plasma sintering of Fe-based structural amorphous metals (SAM) with Y 2 O 3 nanoparticle additions.* Materials Letters, 2008. **62**(17): p. 2988-2991.

224. Khanolkar GR, Rauls MB, Kelly JP, Graeve OA, Hodge AM, and Eliasson V, *Shock Wave Response of Iron-based In Situ Metallic Glass Matrix Composites.* Scientific reports, 2016. **6**.

225. Olevsky E and Froyen L, *Constitutive modeling of spark-plasma sintering of conductive materials.* Scripta materialia, 2006. **55**(12): p. 1175-1178.

226. Kondo T, Yasuhara M, Kuramoto T, Kodera Y, Ohyanagi M, and Munir ZA, *Effect of pulsed DC current on atomic diffusion of Nb–C diffusion couple.* Journal of materials science, 2008. **43**(19): p. 6400-6405.

227. Huntington H and Grone A, *Current-induced marker motion in gold wires.* Journal of Physics and Chemistry of Solids, 1961. **20**(1-2): p. 76-87.

228. Blech IA, *Copper electromigration in aluminum.* Journal of Applied Physics, 1977. **48**(2): p. 473.

229. Rudinsky S, Gauvin R, and Brochu M, *The effects of applied current on one-dimensional interdiffusion between copper and nickel in spark plasma sintering.* Journal of Applied Physics, 2014. **116**(15): p. 154901.

230. Olevsky EA and Froyen L, *Impact of thermal diffusion on densification during SPS.* Journal of the American Ceramic Society, 2009. **92**(s1).

231. Nian Y, Strozier J, Wu N, Chen X, and Ignatiev A, *Evidence for an oxygen diffusion model for the electric pulse induced resistance change effect in transition-metal oxides.* Physical review letters, 2007. **98**(14): p. 146403.